Coherent dynamics of atomic spins on a surface

Veldman, L.M.

DOI
10.4233/uuid:c3e888a9-cfaa-4d67-8ff2-74deebb6ee46

Publication date
2024

Document Version
Final published version

Citation (APA)
Veldman, L. M. (2024). *Coherent dynamics of atomic spins on a surface*. [Dissertation (TU Delft), Delft University of Technology]. https://doi.org/10.4233/uuid:c3e888a9-cfaa-4d67-8ff2-74deebb6ee46

COHERENT DYNAMICS OF ATOMIC SPINS ON A SURFACE

COHERENT DYNAMICS OF ATOMIC SPINS ON A SURFACE

Dissertation

for the purpose of obtaining the degree of doctor
at Delft University of Technology
by the authority of the Rector Magnificus, prof. dr. ir. T.H.J.J. van der Hagen,
chair of the Board for Doctorates
to be defended publicly on
Monday 27 May 2024 at 12:30 o'clock

by

Lukas Maarten VELDMAN

Master of Science in applied physics,
Delft University of Technology, The Netherlands
born in Amsterdam, The Netherlands

This dissertation has been approved by the promotors.

Composition of the doctoral committee:

Rector Magnificus,	chairperson
Prof. dr. A. F. Otte,	Delft University of Technology, *promotor*
Dr. T. van der Sar,	Delft University of Technology, *copromotor*
Independent members:	
Prof. dr. H. Brune,	École polytechnique fédérale de Lausanne, Switzerland
Prof. dr. A. Khajetoorians,	Radboud University, The Netherlands
Prof. dr. ir. L. M. K. Vandersypen	Delft University of Technology
Dr. P. Willke,	Karlsruhe Institute of Technology, Germany
Prof. dr. S. Gröblacher,	Delft University of Technology, reserve member

Prof. dr. A. F. Otte of Delft University of Technology has contributed greatly to the preparation of this dissertation.

Keywords: Scanning tunneling microscopy, coherent spin dynamics, electron spin resonance, pump-probe spectroscopy

Printed by: Gildeprint - Enschede

Cover design: Electron spin resonance data of two coupled titanium atoms. Cover art inspired by the original design of the Joy Division album *Unknown pleasures* by Peter Saville using data from pulsar measurements.

ISBN 978-94-6384-580-9

An electronic copy of this dissertation is available at
https://repository.tudelft.nl/.

But you tell me of an invisible planetary system
in which electrons gravitate around a nucleus.
You explain this world to me with an image.
I realize then that you have been reduced to poetry:
I shall never know.

Albert Camus - The Myth of Sisyphus

CONTENTS

SUMMARY

This thesis presents experiments on the free, coherent spin dynamics of magnetic nanostructures built out of individual titanium atoms adsorbed on bilayer MgO islands grown on a Ag(100) crystal inside a scanning tunneling microscope (STM). We use the exchange field of the spin-polarized probe tip to tune the eigenstates of the magnetic structures to superpositions of the Zeeman product states. These superpositions appear as avoided level crossings of the eigenenergies as a function of tip-atom distance and are detected through electron spin resonance (ESR) measurements. Subsequently, we put the STM tip at the position where we detect an avoided crossing and we perform a DC pump-probe experiment. Here, the pump pulse causes a single spin flip on the atom under state tip which is then allowed to evolve freely for some time t until it is measured by the subsequent probe pulse. By varying the time t between pump and probe over many experiments, we are able to trace out the evolution of the spin under the tip with nanosecond time resolution.

Using this novel measurement scheme, we show a proof-of-concept measurement in chapter 4. Using the atomic manipulation capabilities of STM, we place two Ti atoms closely together so as to couple their electron spins. As a function of magnetic field applied by the STM tip, we find a single avoided level crossing in ESR-STM measurements. Subsequent pump-probe measurements reveal a flip-flop oscillation of the induced spin excitation between the two atoms driven by the spin-spin coupling.

In chapter 5, we build chains of different length out of individual Ti atoms. For every atom that we add to the chain, we find an additional avoided crossing in the ESR-STM measurements and different dynamics in the pump-probe experiment. We attribute this to the different eigenstates that play a role in the formation of the avoided level crossings. As a result, at every point where we observe dynamics, the spin excitation delocalizes over the chain in a different way. By building a branched structure, we use this mechanism to gain some degree of control over the direction of the propagation of the spin excitation.

From here, we shift our focus from the electron spins of single titanium atoms to their nuclear spins. In chapter 6, we resolve the highly anisotropic hyperfine coupling between the nuclear spin and the unpaired electron spin of a ^{49}Ti isotope by performing ESR-STM experiments in a vector magnetic field. Using these measurements, together with a simple point charge model, we are able to determine the groundstate orbital of the unpaired electron, something that was previously not possible to derive experimentally.

Finally, in chapter 7 we use the coherent evolution measurement scheme introduced earlier to observe the free evolution of a spin excitation between the electron spin and the nuclear spin within a single ^{47}Ti isotope. In our ESR-STM measurements, we not only find the point where the spin eigenstates form superpositions, we also find very sharp NMR-type resonances indicating a long spin lifetime of the nucleus. The subsequent pump-probe experiments reveal a beating pattern of multiple frequencies which we attribute to different dynamic processes: a Larmor-like precession of the electron spin and a flip-flop dynamic between the nucleus and the electron spin.

Combined, the results presented in this thesis show the dynamic nature of the quantum mechanical interactions between and within single atoms. They also showcase the potential of STM as a tool for atomic-scale spin dynamics and they open the door to further experiments on low-dimensional magnonics, qubit operations and molecular dynamics. All experimental data and analysis code presented in this thesis is publicly available online at DOI: 10.4121/1c93d3fe-9085-4fb0-91eb-9ecef3be1ee9.

SAMENVATTING

Dit proefschrift bevat experimentele resultaten betreft de vrije, coherente spin dynamica in magnetische nanostructuren bestaande uit enkele titanium atomen die geadsorbeerd zijn op tweelaagse eilanden van MgO op een Ag(100) kristal binnenin een raster tunnel microscoop (STM). We gebruiken het lokale magnetische veld afkomstig van de STM naald om de eigentoestanden van de magnetische structuren naar superposities van de Zeeman toestanden te brengen. Deze superposities zijn waarneembaar als vermeden kruisingen tussen de eigenenergieën als functe van de afstand tussen naald en atoom en worden gedetecteerd in elektron spin resonantie (ESR) experimenten. Vervolgens plaatsen we de STM naald op de tip-atoom afstand waar we een vermeden kruising hebben gemeten en doen we een excitatie-lees experiment. Dit bestaat uit het sturen van twee pulsen: de excitatie puls klapt de spin van een van de twee atomen om, welke daarna een vrije tijdsevolutie ondergaat voor een bepaalde tijd t voordat de magnetisatie van het atoom onder de naald gemeten wordt door de lees puls. Door de tijd t tussen de excitatie en lees pulsen te variëren over meerdere experimenten kunnen we de gehele tijdsevolutie van het atoom onder de naald tot op de nanoseconde nauwkeurig vastleggen.

In hoofdstuk 4 demonstreren we het principe van de experimentele methode die hierboven is beschreven. Met behulp van de atoom manipulatie mogelijkheden van de STM plaatsen we twee titanium atomen zo dicht bij elkaar dat hun elektron spins koppelen. Als functie van het lokale magneetveld van de STM naald, vinden we een enkele vermeden kruising in de ESR metingen. Daaropvolgend laten gepulseerde excitatie-lees experimenten een flip-flop oscillatie van de spin excitatie zien tussen de twee atomen die gedreven wordt door de koppeling tussen de twee spins.

In hoofdstuk 5 bouwen we spinketens van verschillende lengtes uit individuele titanium atomen. Voor elk atoom dat we aan de keten toevoegen vinden we een extra vermeden kruising in de ESR spectra en verandert de dynamica in de gepulseerde metingen. We schrijven dit toe aan de verschillende eigentoestanden die een rol spelen in het totstandkomen van de vermeden kruisingen. Daardoor delokaliseert de spin excitatie op verschillende manieren over de rest van de keten en zien we andere dynamica bij iedere vermeden kruising. Door een vertakte structuur te bouwen maken we gebruik van dit mechanisme om een zekere mate van controle over de propagatierichting van de spin excitatie te krijgen.

Vervolgens verleggen we onze focus van de elektron spin van de enkele titanium atomen naar hun nucleaire spin. In hoofdstuk 6 bestuderen we de anisotropie van de hyperfijn koppeling tussen de nucleaire spin en de ongepaarde elektron spin binnenin een enkel ^{49}Ti isotoop met behulp van ESR metingen in een vector magneetveld. De data uit deze metingen, samen met een simpel puntlading model, volstaan om de grondtoestand orbitaal van het ongepaarde elektron te bepalen, iets dat hiervoor niet experimenteel mogelijk was.

Tot slot gebruiken we in hoofdstuk 7 de coherente evolutie meetmethode die we hiervoor hebben geïntroduceerd om de vrije evolutie van een spin excitatie tussen de elektron spin en de nucleaire spin binnen een enkel ^{47}Ti isotoop te meten. In de ESR metningen vinden we niet alleen het punt waar de eigentoestanden superposities vormen, we vinden ook zeer scherpe NMR-type resonanties die een lange spinleeftijd van de nucleus suggereren. De daaropvolgende gepulseerde excitatie-lees experimenten laten een interferentie patroon zien van meerdere frequencties die we toeschrijven aan verschillende dynamische processen: enerzijds een Larmor-achtige precessie van de elektron spin en anderzijds een flip-flop mechanisme tussen de nucleus en de elektron spin.

Samengenomen tonen de resultaten in deze thesis de dynamische aard van kwantummechanische interacties tussen en binnenin enkele atomen. Ze laten ook de potentie van STM zien als een veelbelovende methode voor onderzoek naar spin dynamica op de atomaire schaal. Daarnaast openen ze de deur naar verdere experimenten aan laagdimensionale magnonica, qubit operaties en moleculaire dynamica. Alle experimentele data and analyse scripts gebruikt voor dit proefschrift zijn publiekelijk beschikbaar online op DOI: 10.4121/1c93d3fe-9085-4fb0-91eb-9ecef3be1ee9.

1

INTRODUCTION

Life moves pretty fast.
If you don't stop and look around once in a while,
you could miss it.

Ferris Bueller

When you look at the sample that was studied in this thesis with the naked eye, you would not see anything particularly interesting or dynamic. You would simply see a shiny, square, silver surface roughly the size of a single ant laying very still. The reason that your measurement is not giving the desired results is in the choice of instrumentation: your eyes are simply bad tools to study the dynamics occurring in solid state materials. In fact, there is a significant amount of movement happening on that metal surface. Phonons travel through the crystal, shaking the entire lattice. Electrons freely move around with certain preferred momenta given by the material. And in some magnetic materials magnons represent movement of the local magnetic moments.

The reason your eyes fail to pick up on all that hidden busyness is twofold. First of all, they lack the spatial resolution. All that movement is happening on the scale of single atoms: way too small for our eyes to see. When you look at the sample's surface, your eyes average over all the tiny parts that form the crystal and therefore also average out the dynamics of the individual atoms. Second, your brain only samples the data coming from your eyes at roughly 30 Hz while the dynamics happening inside solid state materials occur in the Ghz or even THz range. Even if your eyes could resolve single atoms, your brain would average out any dynamics and perceive them to be completely static.

So, if we want to find out more about what is happening at our sample surface we have two tasks: measure at the single atom limit and measure very fast. Just thinking about this possibility already raises multiple fascinating questions: what are the physical properties of a single, isolated atom of a certain species? How does a single atom interact with a single electron, phonon or magnon? How do the interactions between individual atoms result in the macroscopic phenomena observed in bulk experiments? Can we locally induce and control the dynamics of a single atom? In other words: what does the world look like if we don't average over its many parts?

This thesis consists of experiments using a scanning tunneling microscope (STM), a machine devised specifically to answer the question posed above. In chapter 3 we will go into the working principle of STM. Here we will only briefly discuss its use in the study of single magnetic atoms. In short, this microscope achieves sub-atomic resolution by probing a conducting surface using an atomically sharp tip. At its inception in the early eighties, STM was mainly used to characterize the surface of macroscopic materials: one could resolve the individual atoms in the crystallographic structure on the surface [1]. However, soon it was found that individual atoms could be evaporated onto such a surface. These adatoms were not part of the crystal lattice, instead bound much more loosely to the surface. This made it possible to move them to arbitrary positions on the surface using the STM tip [2], allowing one to build structures atom-by-atom [3].

Some atomic species were found to show signs of magnetic interaction with the underlying surface in the form of Kondo resonances on metals [4, 5] and Shiba states on superconductors [6, 7]. These effects arise due to strong coupling of the orbiting electrons of the adatom to the electrons in the underlying substrate. In order to reduce this coupling, adatoms were evaporated onto insulating decoupling layers of only one to several layers thick. This allowed to study the more isolated magnetic properties of the adatoms under the influence of the symmetry of the underlying crystal field [8, 9]. When brought close together, the spins of the adatoms coupled so strongly that the magnetic interaction between them could be studied and quantified [10–13]. The spin state of these structures could even be controlled by the tunneling current [14].

More recently, a new range of magnetic interactions could be studied due to the enhanced energy resolution of combining electron spin resonance (ESR) techniques with STM in 2015. Magnetic dipole interaction between adatoms were mapped on the surface [15, 16], anisotropies in the electronic g-factor [17, 18] were observed and the hyperfine interaction between the electron spin and the nuclear spin in a single atom was resolved [19, 20].

The power and the value of all of these experiments lay in the fact that they got rid of the averaging over large numbers. Observations of Kondo physics, magnetic anisotropy in materials or electron spin resonance had been achieved in bulk materials for a long time already. STM gave the possibility to bring these experiments to the atomic scale, uncovering the microscopic origins of these phenomena. However, all these experiments are concerned with the static properties of the adatoms. The magnetic dynamics that are present at these length-scales were still lost in the time averaging. In this thesis, we aim to study these atomic dynamics and we will try to get a glimpse of what the magnetic nanoworld looks like if we don't average over time either.

The challenge of measuring spin dynamics in single atoms using STM is twofold: on the one hand, the measured signals are very small. Typically, STM measurements consist of picoampere currents running through a single atom. On the other hand, the dynamics at these length-scales are very fast, in the nanosecond or even picosecond range. This means that in these measurement conditions, only one or two electrons can interact with the spin to measure it during its time evolution. These signals are too delicate to be detected in real time due to bandwidth limitations of the STM preamplifier. The solution to this problem is to perform pulsed experiments: instead of averaging over the number of spins or over a long period of time, we average over a large number of repeated experiments. This was first introduced to STM in 2010 in the form of an all electronic pump-probe scheme in order to measure the spin lifetime of a single atom [21]. Suddenly, it was possible to observe the magnetic moment of an atom on a nanosecond timescale.

However, in order to uncover the quantum mechanical nature of the time dependent magnetic properties of single atoms we want to study the coherent dynamics of such systems. This is because these dynamics arise directly from the phase of the wavefunction being preserved over time. In 2019, this was shown for the first time on a single adatom in the form of Rabi oscillations using pulsed ESR techniques [22]. In this experiment, the spin of a titanium atom could be gradually rotated up and down by an external drive which periodically modulates the Hamiltonian. Here, the system has to be continuously perturbed in order to make the spins oscillate and the characteristics of the dynamics (frequency, amplitude, etc.) depend on the parameters of the drive. However, for some systems, coherent dynamics are induced by the Hamiltonian itself: by preparing the system in a certain state, it is bound to evolve freely over time. The characteristics of these dynamics are completely determined by the system alone.

In this thesis, we will present measurements on the free, coherent evolution of a single spin excitation in different spin systems built out of individual Ti atoms. Instead of pulsed ESR techniques, we utilize the electron spin scattering induced by a DC pulse to induce a single spin flip inside these structures during an electronic pump-probe measurement. By controlling the field emanating from the magnetic STM tip, we are able to influence the Hamiltonian of the spin system and change the dynamics.

In chapter 2 we will discuss the different spin Hamiltonians that are relevant for the studied systems. We will also show the calculations used to simulate and interpret the measurements. In chapter 3 we will introduce the experimental techniques mentioned above in detail, as well as showcase our sample preparation and characterization. In chapter 4 we will show the proof-of-concept measurement of the free evolution of a two atom system. We induce a spin flip on one of the two coupled Ti atoms, after which it oscillates between the two atoms at a frequency that is determined by the spin-spin coupling. Continuing this path, in chapter 5 we build larger structures out of multiple Ti atoms. We find that the induced spin excitation becomes delocalized over the structure in different ways depending on the proximity of the STM tip. By building a branched structure we achieve some degree of control over the direction in which the excitation oscillates. In chapter 6, we take a small detour to study the anisotropy of the hyperfine interaction between the nucleus and the unpaired electron spin inside a single Ti isotope using ESR-STM. Using this, we establish a new experimental method to determine the electronic goundstate wavefunction of a single Ti atom on MgO. Finally, in chapter 7 we study the free evolution of a spin flip inside a single Ti isotope. We find that the spin excitation oscillates back and forth between the nucleus and the electron spin in a complex beating pattern arising from a nuclear-electron flip-flop term and a Larmor like precession of the electron spin. We also find nuclear magnetic resonance (NMR) type transitions below 100 MHz, made possible by the efficient spin pumping of both the electron spin and the nuclear spin.

REFERENCES

[1] G. Binnig, H. Rohrer, C. Gerber, and E. Weibel. “Tunneling through a controllable vacuum gap”. In: *Applied Physics Letters* 40.2 (1982), pp. 178–180.

[2] D. M. Eigler and E. K. Schweizer. “Positioning single atoms with a scanning tunnelling microscope”. In: *Nature* 344.6266 (1990), pp. 524–526.

[3] M. F. Crommie, C. P. Lutz, and D. M. Eigler. “Confinement of electrons to quantum corrals on a metal surface”. In: *Science* 262.5131 (1993), pp. 218–220.

[4] V. Madhavan, W. Chen, T. Jamneala, M. Crommie, and N. Wingreen. “Tunneling into a single magnetic atom: spectroscopic evidence of the Kondo resonance”. In: *Science* 280.5363 (1998), pp. 567–569.

[5] K. Nagaoka, T. Jamneala, M. Grobis, and M. Crommie. “Temperature dependence of a single Kondo impurity”. In: *Physical review letters* 88.7 (2002), p. 077205.

[6] A. Yazdani, B. Jones, C. Lutz, M. Crommie, and D. Eigler. “Probing the local effects of magnetic impurities on superconductivity”. In: *Science* 275.5307 (1997), pp. 1767–1770.

[7] K. Franke, G. Schulze, and J. Pascual. “Competition of superconducting phenomena and Kondo screening at the nanoscale”. In: *Science* 332.6032 (2011), pp. 940–944.

[8] A. J. Heinrich, J. A. Gupta, C. P. Lutz, and D. M. Eigler. “Single-atom spin-flip spectroscopy”. In: *Science* 306.5695 (2004), pp. 466–469.

[9] I. G. Rau, S. Baumann, S. Rusponi, F. Donati, S. Stepanow, L. Gragnaniello, J. Dreiser, C. Piamonteze, F. Nolting, S. Gangopadhyay, *et al.* “Reaching the magnetic anisotropy limit of a 3 d metal atom”. In: *Science* 344.6187 (2014), pp. 988–992.

[10] C. F. Hirjibehedin, C. P. Lutz, and A. J. Heinrich. “Spin coupling in engineered atomic structures”. In: *Science* 312.5776 (2006), pp. 1021–1024.

[11] S. Loth, S. Baumann, C. P. Lutz, D. Eigler, and A. J. Heinrich. “Bistability in atomic-scale antiferromagnets”. In: *Science* 335.6065 (2012), pp. 196–199.

[12] A. Spinelli, B. Bryant, F. Delgado, J. Fernández-Rossier, and A. F. Otte. “Imaging of spin waves in atomically designed nanomagnets”. In: *Nature materials* 13.8 (2014), pp. 782–785.

[13] R. Toskovic, R. Van Den Berg, A. Spinelli, I. Eliens, B. Van Den Toorn, B. Bryant, J.-S. Caux, and A. Otte. “Atomic spin-chain realization of a model for quantum criticality”. In: *Nature Physics* 12.7 (2016), pp. 656–660.

[14] S. Loth, K. Von Bergmann, M. Ternes, A. F. Otte, C. P. Lutz, and A. J. Heinrich. “Controlling the state of quantum spins with electric currents”. In: *Nature Physics* 6.5 (2010), pp. 340–344.

[15] T. Choi, W. Paul, S. Rolf-Pissarczyk, A. J. Macdonald, F. D. Natterer, K. Yang, P. Willke, C. P. Lutz, and A. J. Heinrich. “Atomic-scale sensing of the magnetic dipolar field from single atoms”. In: *Nature nanotechnology* 12.5 (2017), pp. 420–424.

[16] K. Yang, Y. Bae, W. Paul, F. D. Natterer, P. Willke, J. L. Lado, A. Ferrón, T. Choi, J. Fernández-Rossier, A. J. Heinrich, *et al.* “Engineering the eigenstates of coupled spin-1/2 atoms on a surface”. In: *Physical Review Letters* 119.22 (2017), p. 227206.

[17] M. Steinbrecher, W. M. Van Weerdenburg, E. F. Walraven, N. P. Van Mullekom, J. W. Gerritsen, F. D. Natterer, D. I. Badrtdinov, A. N. Rudenko, V. V. Mazurenko, M. I. Katsnelson, *et al.* “Quantifying the interplay between fine structure and geometry of an individual molecule on a surface”. In: *Physical Review B* 103.15 (2021), p. 155405.

[18] J. Kim, W.-j. Jang, T. H. Bui, D.-J. Choi, C. Wolf, F. Delgado, Y. Chen, D. Krylov, S. Lee, S. Yoon, *et al.* “Spin resonance amplitude and frequency of a single atom on a surface in a vector magnetic field”. In: *Physical Review B* 104.17 (2021), p. 174408.

[19] P. Willke, Y. Bae, K. Yang, J. L. Lado, A. Ferrón, T. Choi, A. Ardavan, J. Fernández-Rossier, A. J. Heinrich, and C. P. Lutz. “Hyperfine interaction of individual atoms on a surface”. In: *Science* 362.6412 (2018), pp. 336–339.

[20] K. Yang, P. Willke, Y. Bae, A. Ferrón, J. L. Lado, A. Ardavan, J. Fernández-Rossier, A. J. Heinrich, and C. P. Lutz. “Electrically controlled nuclear polarization of individual atoms”. In: *Nature nanotechnology* 13.12 (2018), pp. 1120–1125.

[21] S. Loth, M. Etzkorn, C. P. Lutz, D. M. Eigler, and A. J. Heinrich. “Measurement of fast electron spin relaxation times with atomic resolution”. In: *Science* 329.5999 (2010), pp. 1628–1630.

[22] K. Yang, W. Paul, S.-H. Phark, P. Willke, Y. Bae, T. Choi, T. Esat, A. Ardavan, A. J. Heinrich, and C. P. Lutz. “Coherent spin manipulation of individual atoms on a surface”. In: *Science* 366.6464 (2019), pp. 509–512.

2

THEORETICAL FRAMEWORK

The truth is never exactly what you expect it to be

Johan Cruyff

In this chapter we will discuss the theoretical framework used in this thesis to describe the magnetic properties of Ti atoms on MgO/Ag(100). We start by characterising the different magnetic moments of a Ti atom: its orbital moment, electron spin moment and nuclear spin moment. We then discuss the effective spin Hamiltonian that is used to describe the interactions between these spins and their interactions with the environment. Next, we present methods used in this thesis to simulate STM experiments on these Ti atoms. First, we calculate expected amplitudes of transitions in electron spin resonance (ESR) experiments. Then, we simulate spin dynamics between multiple Ti spins using Lindblad equations. Finally, we use Bloch-Redfield equations to simulate the experimental excitation process of these dynamics using nanosecond timescale DC bias pulses.

2.1. SINGLE ATOM MAGNETISM

The magnetic characteristics of a single atom adsorbed onto a surface can vary significantly depending on the atom, the type of surface and the experimental conditions like temperature and magnetic field. Therefore, it can be very challenging to explain phenomena measured in experiments. An exhaustive description of all interactions would be too complex and impair an intuitive understanding of the systems' behavior. A common approach to circumvent this problem is to use a Spin Hamiltonian formalism to describe the behavior of the spin's degree of freedom in a specific environment.

The electronic contribution to the magnetic properties of an atom are largely determined by the total spin S of the combined electrons in partially filled orbitals and their angular momentum L. In free space, these quantities are given by Hund's rule. On a surface, the crystal field of the surrounding atoms lifts the degeneracy of certain orbitals according to their spatial symmetry. This is often the case for transition metal atoms: species that have partially filled 3d orbitals. In that case, the orbital momentum operator L^2 is no longer preserved resulting in the system eigenstates having a quenched orbital moment: $\langle L_x \rangle, \langle L_y \rangle, \langle L_z \rangle = 0$ [1]. However, the presence of spin-orbit coupling (SOC) partially restores the angular momentum and couples the orbital moment to the electronic spin states. More precisely, spin-orbit coupling originates from relativistic effects arising from the electron orbiting the nucleus [2]. The term has the following form:

$$\hat{H}_{\mathrm{SOC}} = \lambda \hat{\mathbf{L}} \cdot \hat{\mathbf{S}} \tag{2.1}$$

where λ is the spin-orbit parameter. Since for many species the orbital moment is almost fully quenched, the influence of this coupling term is a small perturbation to the spin states. Treating the SOC term to 2^{nd} order in perturbation theory allows one to describe the system with a Hamiltonian that only acts on the spin degree of freedom of the atom: the so-called spin Hamiltonian. As we will see in sections 2.2 and 2.5, this results in the symmetry of the crystal field leaking into the parameters of this spin Hamiltonian. In general, spin-orbit coupling gives rise to magnetic anisotropy. For high spin adsorbates, this usually leads to magnetically stable Ising-like systems with large energy barriers [3, 4].

In this thesis, we discuss experiments performed on Ti atoms adsorbed on bilayer MgO islands grown on top of an Ag(100) crystal. In free space, Ti atoms harbour two unpaired electrons in their 3d orbital, making it a member of the transition metal family. When adsorbed onto bilayer MgO/Ag(100), only one unpaired electron remains, resulting in an effective electron spin number of $\frac{1}{2}$. The leading theory behind this observation is that every Ti atom binds to some residual hydrogen atom, giving up one electron in a covalent bond and forming TiH [5, 6]. The presence of this bond with H has not yet been confirmed experimentally and throughout this thesis we will refer to these atoms as Ti for simplicity. As a result of Kramer's degeneracy's theorem, Ti on MgO doesn't experience magnetic anisotropy, and thus behaves as a quantum Heisenberg spin, making it an excellent testbed for quantum information [7, 8] and quantum simulation applications [9] using single atoms.

Due to the effects of spin-orbit coupling and the interaction of the surface, the electron spin of Ti on MgO is not exactly that of a free spin-$\frac{1}{2}$ particle. In the following, we will describe its response to a magnetic field, the two types of interatomic interactions that Ti atoms on MgO experience in our experiments (exchange and dipolar coupling), and finally the hyperfine coupling between Ti electron and nuclear spins for certain Ti isotopes.

2.2. ZEEMAN INTERACTION AND G-FACTOR ANISOTROPY

One of the key experiments to determine if an experimental observation is magnetic in nature is to observe its response to an external magnetic field. This is because every spin experiences a Zeeman energy splitting as function of the applied field. In all generality, the Zeeman Hamiltonian is given by:

$$\hat{H}_{\text{Zeeman}} = \mu_{\text{B}} \mathbf{B} \cdot \mathbf{g} \cdot \hat{\mathbf{S}} \tag{2.2}$$

where μ_{B} is the Bohr magneton and **g** is the g-tensor which is in general a 3x3 matrix. For free electrons, **g** reduces to an isotropic 3x1 vector with $g_x = g_y = g_z = 2.0023$. Only for certain symmetries of the atom's surroundings can the dimensionality of **g** be reduced [6, 10]. In other words, the symmetry of the binding site of the atom manifests itself in the g-tensor [1]. The origin of the g-tensor anisotropy has been linked to the partially unquenched orbital moment of the Ti electron spin. By including the presence of a hydrogen bound to the atom in the calculations, the g-factor anisotropy was reproduced quantifiably [6].

Ti on MgO can adopt two different adsorption sites as shown in fig. 2.1A. The first adsorption site, on top of a O-site, has a C_{4v} symmetry. As a result, the g-tensor of Ti is a 3x1 vector along the (x, y, z) directions of the crystal field with $g_x = g_y$. The other adsorption site of Ti, bridge site between two O and two Mg atoms, is of C_{2v} symmetry. This leads again to a reduction of the g-tensor as a vector along the crystal field directions but this time with complete anisotropy: $g_x \neq g_y$. As a result, the application of an external magnetic field in-plane, as done in our experiments, leads to various Zeeman splitting for the three types of Ti atoms (one O-site and two bridge sites – vertical and horizontal) on MgO that we investigate, as shown in fig. 2.1B.

In our experiments, the magnetic fields experienced by the Ti atoms can be of two origins: the external magnetic field as well as the magnetic field induced by the magnetic tip. For the latter, its fast spatial decay makes it only relevant for the atom directly underneath the tip and we neglect its effect on other spins.

Finally, we note that nuclear spins also experience a Zeeman effect. However, it scales with the nuclear magneton μ_{N} which is three orders of magnitude smaller than the Bohr magneton μ_{B}. Therefore, we neglect the nuclear Zeeman energy in this thesis.

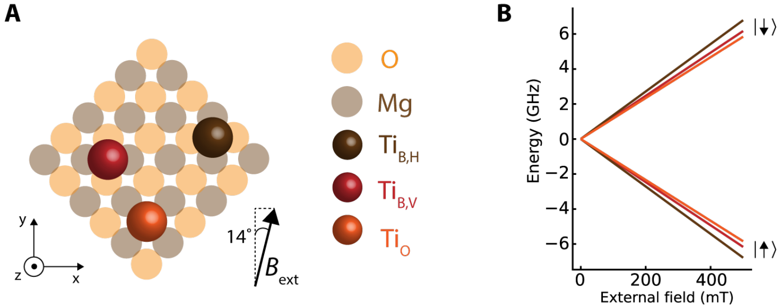

Figure 2.1: Zeeman splitting and g-factor anisotropy. A. Schematic image of Ti atoms bound on different binding site on the MgO lattice. **B.** Calculated Zeeman splitting for Ti on the three binding sites showing the effect of the difference in g-tensor components.

2.3. HEISENBERG EXCHANGE COUPLING

Another key ingredient in describing the magnetic properties of single atoms on surfaces is the coupling between individual atoms. This inter-spin coupling is at the origin of many interesting effects: emergent magnetic phenomena such as spin waves [11], long range magnetic order [12], the quantum to classical transition [13–15] and the possibility to transfer magnetic information over different atoms [16]. Several mechanisms can mediate spin interactions, among them are direct exchange arising from the overlap of the electron wavefunctions [2], super-exchange or RKKY type coupling mediated by the electron bath of the surface [17]. For two atoms in close proximity to one another, the dominant coupling mechanism is the Heisenberg exchange coupling:

$$\hat{H}_{\text{Heis}} = J\hat{\mathbf{S}}_1 \cdot \hat{\mathbf{S}}_2. \tag{2.3}$$

Here, $\hat{S}_1$ and $\hat{S}_2$ are the spin operators of the coupled spins and the exchange coupling parameter J is assumed to be isotropic for simplicity. The sign of J determines if the coupling is antiferromagnetic (AFM, $J > 0$) of ferromagnetic (FM, $J < 0$). In-depth analysis of the coupling between pairs of Ti atoms done in chapter 5 shows that for the systems studied in this thesis, the exchange coupling is AFM and isotropic as is often assumed for single atoms on a surface [18]. Characteristic of exchange coupling is the exponential decay over distance, as shown in fig. 2.2. Therefore, it is sufficient to consider only nearest neighbor interactions when describing a system comprising several spins.

To appreciate the quantum nature of this coupling, we need only look at the eigenstates of the Hamiltonian of eq. (2.3). For the case of two coupled spins, the exchange Hamiltonian produces singlet-triplet eigenstates as shown in fig. 2.2B. Here, we use the shorthand notation $|-\rangle = \frac{1}{\sqrt{2}}(|\uparrow\downarrow\rangle - |\downarrow\uparrow\rangle)$ and $|+\rangle = \frac{1}{\sqrt{2}}(|\uparrow\downarrow\rangle + |\downarrow\uparrow\rangle)$. This showcases that the exchange coupling gives rise to a fundamentally quantum mechanical property in a spin system: the eigenstates are entangled and delocalized over two atoms separated in space. In contrast, the Zeeman Hamiltonian discussed before produces so called Zeeman product states: $|\uparrow\uparrow\rangle, |\uparrow\downarrow\rangle, |\downarrow\uparrow\rangle, |\downarrow\downarrow\rangle$.

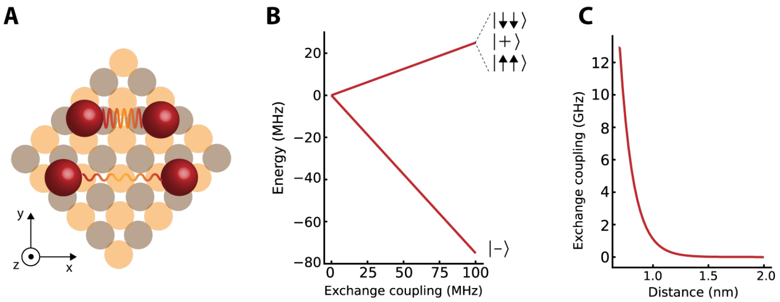

Figure 2.2: Heisenberg exchange coupling. A. Schematic picture of exchange coupled atoms on a surface. **B.** Energy diagram and eigenstates resulting from antiferromagnetic exchange coupling. **C.** Characteristic exponential decay of exchange coupling over distance between two Ti atoms on a surface.

2.4. DIPOLE-DIPOLE COUPLING

At larger distances, atomic spins couple to each other via dipole-dipole interaction. This coupling arises from one atom experiencing the magnetic field emanating from another atom. This is a fundamentally different interaction from exchange coupling and has very distinct characteristics: it is highly anisotropic and decays with the cube of the distance. We can write the dipolar interaction between two spin as follows:

$$\hat{H}_{\text{dipole}} = \frac{\mu_0 \gamma_1 \gamma_2 \hbar^2}{4\pi \left|\mathbf{r}_{1,2}\right|^3} \left(3(\hat{\mathbf{S}}_1 \cdot \hat{\mathbf{r}}_{1,2})(\hat{\mathbf{S}}_2 \cdot \hat{\mathbf{r}}_{1,2}) - \hat{\mathbf{S}}_1 \cdot \hat{\mathbf{S}}_2\right) \tag{2.4}$$

With $\hat{\mathbf{r}}_{12}$ the vector connecting the spins $\hat{\mathbf{S}}_1$ and $\hat{\mathbf{S}}_2$ and $\left|\mathbf{r}_{1,2}\right|$ the distance between them. In the case of dipole-dipole interaction between two Ti atoms we neglect the g-factor anisotropy: $\gamma_1 = \gamma_2 = \frac{g\mu_B}{\hbar}$. To simplify this equation further we use the secular approximation which is valid when the external field dominates over the dipolar field of the spins: $E_{\text{Zeeman}} > E_{\text{dipole}}$ [5, 19]. In this case we can assume that in the ground state, the spins both follow the external field and the dipolar field is just a perturbation. Following [20] we arrive at:

$$\hat{H}_{\text{dipole}} = D_{1,2}\left(3\hat{S}_1^z \hat{S}_2^z - \hat{\mathbf{S}}_1 \cdot \hat{\mathbf{S}}_2\right) \tag{2.5}$$

Where we define $D_{1,2} = \frac{D_0}{\left|\mathbf{r}_{1,2}\right|^3}(1 - 3\cos^2\theta)$ with $D_0 = \frac{g\mu_B}{2\pi}$ and θ the angle between the vector $\mathbf{r}$ and the direction of the external field. In this form we can immediately note a number of characteristics of the dipolar coupling. First, from the form of the Hamiltonian in eq. (2.5) we see that that the coupling terms are a mix of Ising and Heisenberg type coupling. Second, the magnitude of the coupling parameter D can be either positive or negative depending on the angle θ. This spatial dependence is calculated for constant $|\mathbf{r}|$ and an external field at a 14° angle with the y-axis (corresponding to our experiment) in fig. 2.3. We find that depending on the angle between the spins, the dipolar coupling is either strongly AFM of weakly FM. At the so-called magic dipole angles of 54.7° and 125.3° the term $(1 - 3\cos^2\theta) = 0$ and the dipolar coupling vanishes completely.

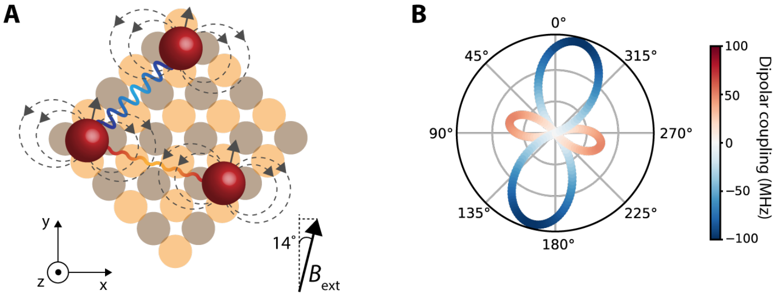

Figure 2.3: Dipole-dipole coupling. **A.** Schematic picture of Ti atoms on a MgO surface and the magnetic field lines emanating from them. Depending on their relative orientation, the dipolar coupling can be AFM or FM. **B.** Angle dependence of the dipolar coupling parameter D calculated for constant distance $|\mathbf{r}|$. The external field is applied at a 14° angle. The radial axis of the plot shows the absolute value of the dipolar constant $|D|$ while the color also shows the sign of the coupling.

2.5. HYPERFINE COUPLING

Titanium has five stable isotopes, three of which have no net nuclear spin: ^{46}Ti, ^{48}Ti and ^{50}Ti. Since we have no way of discerning these three isotopes using STM we just refer to this group as ^{48}Ti throughout this thesis as that is by far the most abundant species of the three (73%). The other two isotopes do have a net nuclear spin: $I = \frac{5}{2}$ for ^{47}Ti (7%) and $I = \frac{7}{2}$ for ^{49}Ti (5%). These nuclear spins are coupled to the unpaired orbiting electron spin through the hyperfine interaction:

$$\hat{H}_{\text{hyperfine}} = \hat{\mathbf{I}} \cdot \mathbf{A} \cdot \hat{\mathbf{S}} \tag{2.6}$$

where we allow for an anisotropic hyperfine coupling vector $\mathbf{A}$ between the nuclear spin $\hat{\mathbf{I}}$ and electron spin $\hat{\mathbf{S}}$. Here, again the symmetry of the adsorption site can reduce the dimensionality of $\mathbf{A}$ and dictate its anisotropy. This equation bears a resemblance to the Heisenberg exchange Hamiltonian and indeed leads to the same kind of superposition eigenstates between electron and nuclear spins as the exchange interaction does between neighboring atomic electron spins. We will exploit this parallel by performing similar experiments between atoms (chapter 4) and between the electron spin and the nuclear spin within the same atom (chapter 7).

The hyperfine coupling $\mathbf{A}$ consists of three contributions. The Fermi contact interaction is a term arising from the dipolar interaction between the nuclear spin and the electron spins in the s orbitals [21]. Due to the symmetry of the s orbitals, this term is completely isotropic. However, other orbitals (like the p and d orbitals) are not spherically symmetric. The dipolar coupling between spin densities in these orbitals can thus attribute anisotropic terms to the overall hyperfine coupling. In chapter 6 we will do an in depth investigation into the hyperfine anisotropy of a single Ti atom and show that this anisotropy can be used to determine the electronic ground state of the atom.

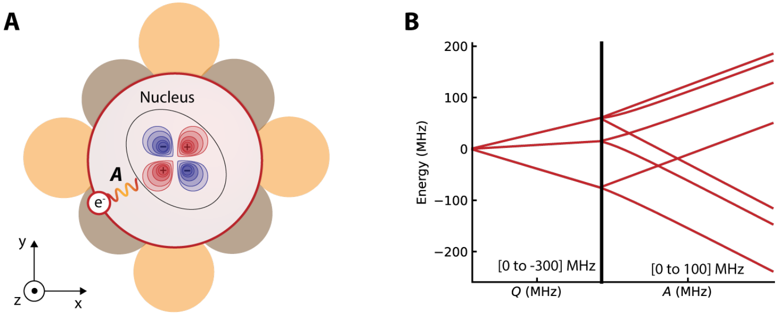

Figure 2.4: Quadrupole and hyperfine interaction. **A.** schematic picture of the interactions between nuclear and electronic spins inside a single Ti atom. The nuclear quadrupole charge distribution is approximated by an ellipsoid. **B.** calculations of the energy level splitting due to quadrupole and hyperfine interactions. Calculations were done using $\eta = 0$, $I = \frac{5}{2}$, $S = \frac{1}{2}$.

Next to the hyperfine interaction that couples the nuclear spin to the electrons that orbit around it, large nuclear spins ($I > \frac{1}{2}$) also experience anisotropy energies due to the quadrupole interaction. This energy splitting arises from the fact that large nuclear spins have asymmetric quadrupole charge distributions that deviate from spherical symmetry (see fig. 2.4A). Gradient electric fields originating either from the charge distributions of the orbiting electron or directly from the nearby crystal field can result in an effective torque on the charged nucleus. In turn, this torque gives rise to magnetic anisotropy splitting of the nuclear spin states [22]. The general form of this term is given by:

$$\hat{H}_{\text{quad}} = \hat{\mathbf{I}} \cdot \mathbf{Q} \cdot \hat{\mathbf{I}}. \tag{2.7}$$

We can write the quadrupole interaction tensor $\mathbf{Q}$ as a diagonal 3 by 3 matrix [23]:

$$\mathbf{Q} = \frac{e^2 qQ/h}{4I(2I-1)} \begin{bmatrix} -(1-\eta) & 0 & 0 \\ 0 & -(1+\eta) & 0 \\ 0 & 0 & 2 \end{bmatrix}. \tag{2.8}$$

Here, $0 < \eta < 1$ is the in-plane anisotropy parameter, I the magnitude of the nuclear spin, eq is the electric field gradient and eQ the mount the nuclear charge distribution departs from spherical symmetry. The effects of both Q and A on the spin states a of ^{47}Ti atom ($I = \frac{5}{2}$, $S = \frac{1}{2}$) are plotted in fig. 2.4B. The quadrupole term splits the nuclear spin states in pairs: $m_I = \pm\frac{5}{2}, \pm\frac{3}{2}, \pm\frac{1}{2}$. The hyperfine term forms entangled states of the electron and nuclear spins.

2.6. ESR-STM SIMULATIONS

In the previous section, we discussed the different interactions that occur within and between individual Ti atoms on a surface and we have presented the Hamiltonians that describe these interactions. We will now turn to the calculation methods that we use to simulate experimental results, starting with electron spin resonance (ESR) experiments. For experimental details of the working principle of the technique, see chapter 3. During ESR measurements, we drive transitions between the magnetic eigenstates of the atomic system that we study. To first approximation, the measured intensity of a transition is determined by three factors: the driving amplitude, the population difference between the two states and the detection amplitude. We can write the total measured peak amplitude as:

$$I^{\mathrm{ESR}}_{n,m} \propto \left|V_{n,m}\right|^2 \Delta P_{n,m} \left(\langle n|\, \hat{S}^{\mathrm{tip}}_z\, |n\rangle - \langle m|\, \hat{S}^{\mathrm{tip}}_z\, |m\rangle\right). \tag{2.9}$$

Here, the first term represents the driving amplitude as a result of an oscillating transverse magnetic field term applied to the spin underneath the tip. This results in the following coupling term:

$$V_{n,m} = \langle n|\, (\hat{S}^{\mathrm{tip}}_+ + \hat{S}^{\mathrm{tip}}_-)\, |m\rangle \tag{2.10}$$

where $\hat{S}^{\mathrm{tip}}_+$ and $\hat{S}^{\mathrm{tip}}_-$ are raising and lowering operators that only work on the electron spin of atoms underneath the tip. It follows that only transitions with $\Delta m = \pm 1$ for the spin underneath the tip can be driven. In recent experiments, Ti atoms have also been driven remotely via a nearby Fe atom, circumventing this limitation of the highly localized driving of ESR-STM [7]. However, in the experiments we present in this thesis we consciously keep our Ti atoms very far away from the stray fields of Fe atoms on the surface and therefore only consider driving of the Ti atom underneath the tip.

In the case of atoms with nonzero nuclear spin we add an extra driving term that works on the nuclear spin of the atom underneath the tip: $V^{\mathrm{nuclear}}_{n,m} = \langle n|\, (\hat{I}^{\mathrm{tip}}_+ + \hat{I}^{\mathrm{tip}}_-)\, |m\rangle$. We do this in order to match the amplitude of the nuclear magnetic resonance (NMR) type transitions measured in the experiments (see chapter 7). In these transitions the nuclear spin transitions are driven instead of electron spin transitions. We believe that the large amplitude of these transitions could originate from directly driving the nucleus via the hyperfine Stark effect [24] or modulation of the quadrupole interaction via the applied RF electric field. However, the extra amplitude could also arise from a difference in spin lifetime between the electron and nuclear spin that we do not take into account in this modeling of the transition amplitudes.

The second factor in eq. (2.9) is the population difference between the two states ΔP. If two states are equally populated, driving a spin transition between them will not result in any change in population and therefore be undetectable. The populations of the eigenstates of a spin system can be determined by temperature and calculated from the Boltzmann distribution. Alternatively, if spin pumping effects dominate, the populations can be calculated via rate equations [25] or with Bloch-Redfield equations (see section 2.8).

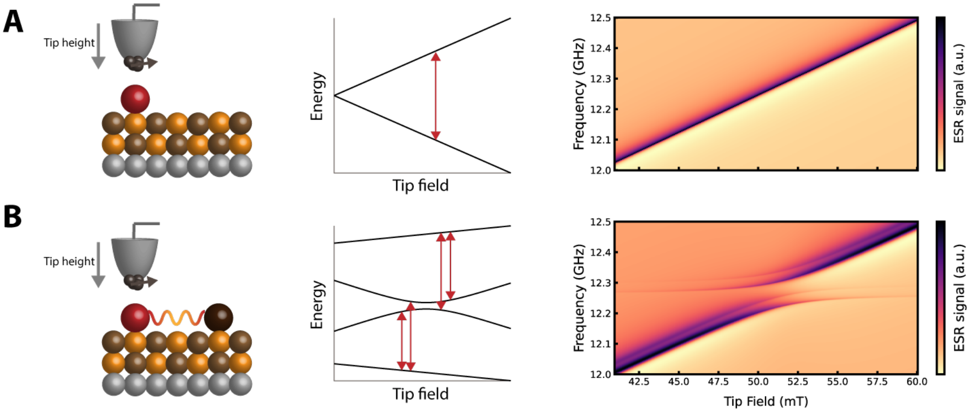

Figure 2.5: Simulating ESR-STM experiments. A. Simulations for a single Ti atom experiencing Zeeman splitting due to an external field and a local tip-induced field. We drive a single transition between two spin states at a resonance frequency that linearly increases with the applied field. **B.** Simulations for two coupled spins with different g-factors. By applying the tip field on the atom with the lowest g-factor, the difference in Zeeman energy can be compensated. In that case, the first and second excited state form an avoided level crossing and the composition of the eigenstates changes drastically. This is reflected in the simulated transition amplitudes at the crossing point.

The final factor in eq. (2.9) represents the detection mechanism of the transition. The spin-polarized tunneling current interacts solely with the electron spin of the atom underneath the tip. Therefore, it can only detect changes in the average polarization of that particular electron spin. This means that we are not sensitive to any spin transitions that do not change the average spin state of the atom underneath the tip.

We note that we do not take into account homodyne detection, which allows for detection of spin transitions with $\Delta m = 0$ like a singlet-triplet transition. Even though these transitions have been observed experimentally [26], we do not encounter them in the experiments discussed in this thesis.

In fig. 2.5 we show two example cases for which we simulate the ESR-STM spectra. In fig. 2.5A we consider a single Ti atom that experiences Zeeman splitting due to an external field and the local tip field. The colorplot shows the linear dependence of the resonance frequency with applied tip field. In fig. 2.5B we add an atom with a different g-factor and consider the exchange and dipolar interactions between the spins as well as the Zeeman interaction. We now apply the tip field on the Ti spin with the lowest g-factor and simulate the ESR spectra we expect to measure on that atom. We find an avoided crossing at the point where the added tip field compensates the difference in g-factor causing both spins to experience the same Zeeman splitting. This drastically changes the composition of the eigenstates with is reflected in the amplitudes of the four difference ESR transitions. We describe this experiment in chapter 4.

2.7. SYSTEM DYNAMICS: LINDBLAD EQUATIONS

In this chapter we have so far discussed the different Hamiltonians that predict the energy state space of Ti atoms on an MgO surface and we discussed the expected amplitude of resonant transitions between these states as measured by ESR-STM. This allows us to gain greater understanding of the static properties and energies of the atomic spin system that we study in the experiments presented in chapters 4 to 7. Now, we finally turn to the central topic of this thesis: studying the dynamical properties of these spin systems. For details on the experimental method, see chapter 3. In this section we will discuss numerical methods to predict the dynamics of these single spin excitations in different spin systems. We will do so by making use of the density matrix formalism:

$$\hat{\rho} = \sum_j p_j \left|\psi_j\right\rangle\left\langle\psi_j\right|. \tag{2.11}$$

Here, a state is represented by a density matrix $\hat{\rho}$ with p_j the weights of each basis state $\left|\psi_j\right\rangle$. The diagonal elements of $\hat{\rho}$ are called the populations as they tell us the probability of finding the system in that particular state during a measurement in that basis. The off-diagonal elements are called the coherences and represent the phase information present between two basis state components. This representation also allows to describe the system in a mixed state: in such a state, the phase information between the different basis state components is unknown, i.e. the off-diagonal elements are zero.

As is often the case in quantum mechanics, the choice of basis used to describe the system state has a large influence on the composition of $\hat{\rho}$ and therefore what is considered a population and what a coherence. In this thesis we will only display density matrices in the energy eigenbasis of the Hamiltonian so that the populations are static under influence of $\hat{H}$. The dynamics due to the system thus always originate from the coherences of the state.

We can calculate the dynamics of a perfectly isolated quantum system with known Hamiltonian using the von Neumann equation:

$$\frac{\mathrm{d}\hat{\rho}(t)}{\mathrm{d}t} = -\frac{i}{\hbar}[\hat{H}, \hat{\rho}(t)]. \tag{2.12}$$

This equation is the equivalent of the Schrödinger equation in density matrix formalism: it describes the unitary time evolution of a density matrix $\hat{\rho}$ under the influence of a Hamiltonian $\hat{H}$. In principle, this relatively simple equation is sufficient to describe all dynamics that arise from interactions between different Ti spins.

However, the Ti atoms that we study are not perfectly isolated from their environment. In fact, the coupled Ti atom system is better described as an 'open' quantum system that interacts with, for example, nearby electrons in the sample and tip, phonons in the underlying lattice and stochastic magnetic field fluctuations [27]. Importantly, these interactions can cause transitions between energy levels (changes in the populations) and loss of phase information (decay of the coherences). We can write a general description of an open quantum system as follows:

$$\hat{H}_{\text{total}} = \hat{H} + \hat{H}_{\text{B}} + \hat{H}_{\text{I}} \tag{2.13}$$

where $\hat{H}$ is the system Hamiltonian, $\hat{H}_{\text{B}}$ the bath Hamiltonian of the environment and $\hat{H}_{\text{I}}$ describing the interaction between bath and system. In principle, we could still solve the von Neumann equation for this new combined Hamiltonian, however, usually the environment consists of nearly infinite degrees of freedom (i.e. all electrons in a metal substrate) and therefore attempting this is futile. Common is to treat the bath as a perturbation to the system, in other words: $\hat{H}_I \ll \hat{H}, \hat{H}_{\text{B}}$ is small. In that case, we can use a quantum master equation that describes the time evolution of the reduced density matrix $\hat{\rho}$ of the system instead of the whole Hamiltonian. Below, we will briefly discuss the most commonly used quantum master equation: the Lindblad equation [28, 29]. The general equation is written as follows:

$$\frac{\mathrm{d}\hat{\rho}(t)}{\mathrm{d}t} = -\frac{i}{\hbar}[\hat{H}, \hat{\rho}(t)] + \sum_n \frac{1}{2}[2\hat{L}_n\hat{\rho}(t)\hat{L}_n^\dagger - \hat{\rho}(t)\hat{L}_n^\dagger\hat{L}_n - \hat{L}_n^\dagger\hat{L}_n\hat{\rho}(t)] \tag{2.14}$$

With $\hat{L}_n$ the Lindblad jump operators defined as $\hat{L}_n = \sqrt{\gamma_n}\hat{A}_n$. Here, $\hat{A}_n$ is the operator through which the environment effectively couples to the system density matrix $\hat{\rho}$ and γ_n is the associated rate at which this process happens.

For the Lindblad equation to be applicable, several approximations must be justified. We already mentioned that the coupling between system and environment must be weak. If we know that the bath is many times larger than the system, we can also assume that the influence of the system on the bath is negligible. This is called the Born approximation and it assumes that the bath remains constant throughout the time evolution. This allows us to separate the density matrix of the bath and the system: $\hat{\rho}_{\text{total}} = \hat{\rho} \otimes \hat{\rho}_{\text{bath}}$. The second important assumption that is necessary for the Lindblad treatment is that the bath has very short term memory. In other words, the interaction between bath and the system only depends on the system state and is not influenced by correlations within the bath. This is known as the Markov approximation. For this approximation to be valid, the system must have a long relaxation time compared to the lifetime of correlations inside the bath: $\tau_S \gg \tau_B$. If we consider Ti atoms interacting with an electron bath in a metal substrate this is a valid assumption to make. Lastly, to arrive at eq. (2.14), it is also necessary to neglect terms that oscillate fast compared to timescales that are intrinsic to the system. This can be done either by applying the rotating wave approximation or the secular approximation [30].

The appeal of the Lindblad equations is that it is relatively easy to apply phenomenological operators to simulate the dissipative effects of an environment on a spin system. For example, pure dephasing of a single spin-$\frac{1}{2}$ particle can easily be modelled by inserting $\hat{L} = \sqrt{\frac{1}{T_2}}\hat{S}_z$ to eq. (2.14). However, the Lindblad formalism can be applied in much more involved ways [31, 32]. In this thesis, we only use phenomenological jump operators to crudely simulate dissipation effects in Ti spin systems using the Lindblad equation in the QuTiP package [33].

Although simulating STM experiments on Ti spin dynamics using this approach is effective (see chapter 5), it falls short most noticeably for the excitation process. We start the time evolution at a chosen initial state after excitation, assuming the experimental bias pulse will indeed lead to a coherent spin state. To understand how interaction with the incoherent electrons tunneling through the atom can result in a coherent spin state, we have to use a more involved model using the Bloch-Redfield framework.

2.8. EXCITATION PROCESS: BLOCH-REDFIELD EQUATIONS

The Bloch-Redfield equations are closely related to the Lindblad equations. Both are quantum master equations based on the Born and Markov approximations and are valid in the case of weak coupling between system and environment [34, 35]. In fact, the Bloch-Redfield terms can often be rewritten into a Lindblad form if the additional secular approximation is applied [36]. The difference lies in the approach to the description of the environment. The Lindblad equations give a phenomenological description of the interaction with a bath in terms of decoherence and spin flip 'jumps' and the rates at which these effects happen are considered free parameters. The Bloch-Redfield formalism describes the interaction with a bath starting from a microscopic picture. This has the large benefit that the system-bath interaction has clear physical interpretation and can be tailored to a specific type of environment. The downside is that the Bloch-Redfield approach is not guaranteed to result in a physically sound density matrix as evolution by the Redfield tensor could lead to negative populations in $\hat{\rho}$ and is therefore considered less robust [37].

In this section, we will describe the coupling between the Ti spin system and the electron baths in the substrate and tip using Bloch-Redfield. We assume the interaction Hamiltonian to have to following form:

$$H_I = \sum_{\alpha} \hat{A}_{\alpha} \otimes \hat{B}_{\alpha} \tag{2.15}$$

where $\hat{A}$ are system operators and $\hat{B}$ bath operators and we sum over all interactions. In our case we will consider interactions of a single nature: Kondo scattering between Ti spins and electrons in the tip and sample baths. This specific interaction Hamiltonian has the form:

$$\hat{H}_{\text{Kondo}} = \sum_{i} \sum_{j=\text{t,s}} J_{i,j} \hat{\mathbf{S}}_i \cdot \hat{\mathbf{s}}_j. \tag{2.16}$$

Here, $\hat{\mathbf{S}}_i$ is the spin operator for the i'th atom, $\hat{\mathbf{s}}_j$ are the operators of the spin baths of the tip and the sample and $J_{i,j}$ describe the coupling between each atoms and each bath. The bath operators are expressed as:

$$\hat{s}_{\alpha} = \sum_{k,k',\sigma,\sigma'} \hat{a}^{\dagger}_{k,\sigma} \frac{\tau^{\alpha}_{\sigma,\sigma'}}{2} \hat{a}_{k',\sigma'}. \tag{2.17}$$

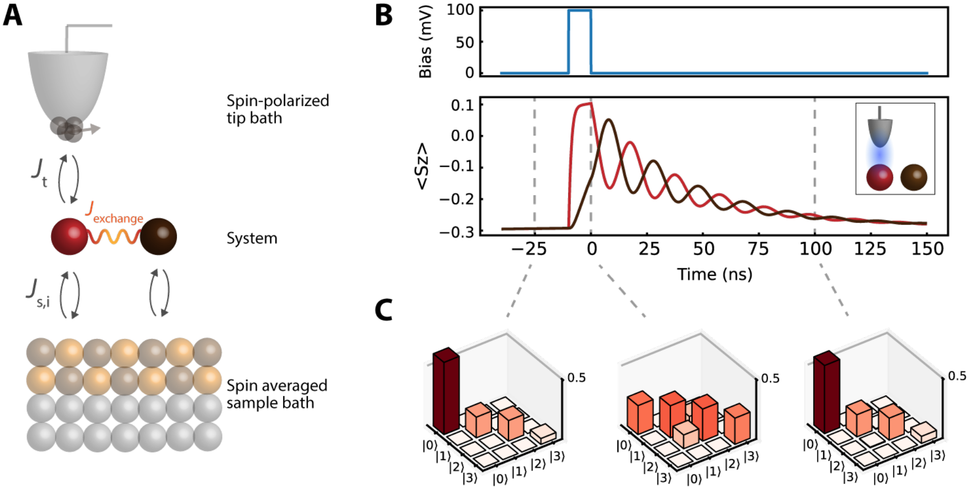

Figure 2.6: Bloch-Redfield simulations. A. Schematic picture of the scattering processes considered in the Bloch-Redfield calculations. All Ti atoms in the system are coupled to the sample bath and experience sample-sample scattering. Only the atom underneath the tip experiences scattering from electrons tunneling between tip and sample. In our case, tip-tip scattering is neglected. **B.** Bloch-Redfield simulations for two coupled atoms experiencing the same Zeeman splitting. Top panel: time dependent applied bias consisting of a 10 ns square pulse. Bottom panel: calculated expectation value $\langle S_z \rangle$ of both spins as a result of the applied bias. Temperature: $T = 0.4$ K, exchange coupling: $J_{\text{exchange}} = 50$ MHz, spin-polarization vector: $|\mathbf{n}| = 0.3$, sample coupling: $J_s = 0.06$, tip coupling: $J_t = 0.005$. **C.** Density matrices calculated at different moments during the time evolution. Before excitation, the system is in thermal equilibrium (left). After the bias pulse, the system is excited and coherences appear in the density matrix due to scattering with the spin polarized tunneling electrons (center). At $t \gg T_1, T_2$, the system has returned back to thermal equilibrium due to scattering with the spin-averaged electrons in the sample bath (right).

Here, $\tau^{\alpha}_{\sigma,\sigma'}$ are the Pauli spin operators of the substrate electrons in the three spatial dimensions ($\alpha = x, y, z$) and $\hat{a}^{\dagger}_{k,\sigma}$ ($\hat{a}_{k',\sigma'}$) the creation (annihilation) operator as used in a second quantization description.

We have now described the nature of the interaction between the spin system and the bath: the Ti spins can exchange angular momentum as well as phase information with the electron bath through scattering events. Next, we will calculate the impact of this interaction on the system density matrix element ρ_{nm} using the general form of the Bloch-Redfield equation:

$$\frac{d\rho_{nm}(t)}{d(t)} = -i\omega\rho_{nm}(t) + \sum_{kl}\left(R_{nmkl} + R'_{nmkl}(t)\right)\rho_{kl}(t). \tag{2.18}$$

The first term can be recognised as the Von Neumann equation shown in section 2.7 and cover the unitary evolution of density matrix element ρ_{nm}. The second term describes how weight from the density matrix element ρ_{kl} influences the element ρ_{nm} over time. Here we distinguish between two separate Redfield tensors: the constant R_{nmkl} and the time dependent $R'_{nmkl}(t)$. This is because we consider two different scattering paths. In sample-sample scattering, an electron originates from the sample bath, interacts with the Ti spin and ends up back in the sample bath. We consider this interaction to be time independent and always present throughout the calculated time evolution. Consequently, it can be described by R_{nmkl} and we applied it to all Ti spin in the system. On the other hand, we consider tunneling of electrons between the tip and sample baths via the Ti spin underneath the tip. This interaction is dependent on the applied bias between tip and sample and is therefore time dependent in the case of a pulsed measurement. We describe it using $R'_{nmkl}(t)$ and only apply it to the spin underneath the tip. Since we assume $J_t \ll J_s$ we neglect the constant tip-tip scattering channel. A schematic picture of the considered scattering processes and their coupling parameters is shown in fig. 2.6A. The Redfield tensor has the following general form:

$$R^{a\to b}_{nmkl} = \frac{1}{\hbar^2} J_a J_b \sum_i \sum_{\alpha,\beta=x,y,z} \begin{pmatrix} -\delta_{ml}\sum_p \langle n|\,\hat{S}^{\alpha}_i\,|p\rangle\langle p|\,\hat{S}^{\beta}_i\,|k\rangle\, g^{\alpha\beta}_{a\to b}(\omega_{pk}) \\ -\delta_{nk}\sum_p \langle l|\,\hat{S}^{\alpha}_i\,|p\rangle\langle p|\,\hat{S}^{\beta}_i\,|m\rangle \left(g^{\alpha\beta}_{a\to b}(\omega_{pl})\right)^* \\ +\langle n|\,\hat{S}^{\beta}_i\,|k\rangle\,\langle l|\,\hat{S}^{\alpha}_i\,|m\rangle\left(g^{\alpha\beta}_{a\to b}(\omega_{nk}) + \left(g^{\alpha\beta}_{a\to b}(\omega_{ml})\right)^*\right) \end{pmatrix}. \tag{2.19}$$

These terms describe the influence of electrons scattering from bath a to bath b scaled by their corresponding coupling strengths J_a and J_b. The functions $g^{\alpha\beta}_{a\to b}$ are correlation functions of the baths that depend on the energy difference of the states that they connect. They are expressed using the bath operators:

$$g^{\alpha\beta}_{a\to b}(\omega_{nm}) = \int_0^{\infty} \langle B^{\alpha\beta}_b(t) B^{\alpha\beta}_a(0)\rangle e^{-\omega_{nm}t}\,dt. \tag{2.20}$$

We discard the complex part of this integral which would lead to a small re-normalisation of the energy levels [27]. We can calculate the correlation functions for the two specific scattering channels we consider. In the case of interaction with the sample electrons we assume the bath to be spin averaged and time independent:

$$g^{\alpha\beta}_{\mathrm{s}\to\mathrm{s}}(\omega_{nm}) = \frac{\hbar\pi(\eta^{\mathrm{s}})^2}{4}\sum_{\sigma,\sigma'}\frac{\tau^{\alpha}_{\sigma\sigma'}\tau^{\beta}_{\sigma'\sigma}}{4}\iint f(\epsilon)(1-f(\epsilon'))\delta(\epsilon-\epsilon'-\epsilon_{nm})\,d\epsilon\,d\epsilon'. \tag{2.21}$$

Here, η^{s} is the density of states of the sample and $f(\epsilon)$ is the Fermi-Dirac distribution. In case of electrons tunneling between the two baths the correlation function looks slightly different. Here, we need to take into account the applied bias that shifts the Fermi level of one bath with respect the the other and we need to account for the spin polarized density of states of the tip [38, 39]. We obtain:

$$g^{\alpha\beta}_{\mathrm{t}\to\mathrm{s}}(\omega_{nm}, t) = \hbar\pi \sum_{\sigma,\sigma',\sigma''} \frac{\tau^{\alpha}_{\sigma''\sigma'}\tau^{\beta}_{\sigma\sigma'}}{4} \eta^{\mathrm{t}}_{\sigma''\sigma'}\eta^{\mathrm{s}}_{\sigma\sigma} \iint f(\epsilon)(1-f(\epsilon'))\delta(\epsilon-\epsilon'-\epsilon_{nm}-V(t))\, d\epsilon\, d\epsilon' \tag{2.22}$$

where we allow the bias to be time dependent and we describe the spin polarized density of states in the tip as $\hat{\eta}^{\mathrm{t}} = \frac{1}{2}(\hat{\mathbb{I}}+\mathbf{n}\cdot\hat{\tau})$. Here, $\mathbf{n}$ is a vector pointing along the tip polarization axis with magnitude $0 < |\mathbf{n}| < 1$ and $\hat{\tau}$ is a vector containing the Pauli spin matrices.

In fig. 2.6B we show simulation results for a two atom system. The two spins are subjected to an external magnetic field via the Zeeman Hamiltonian and are coupled to each other by the exchange interaction. The initial state is calculated by letting the system relax to its equilibrium state at zero bias. We then apply a 10 ns long, 100 mV bias pulse (top panel). Scattering with spin polarized tunneling electrons immediately affects the spin state of the atom underneath the tip (in red, bottom panel) changing its spin projection. The response of the coupled atom (dark brown) is delayed compared to the red spin as the excitation process first has to be mediated through the exchange coupling. As a result, the two spins have different $\langle\hat{S}_z\rangle$ spin projections at the end of the bias pulse. This excitation sets off an oscillation between the two spins that slowly decays over time due to relaxation and decoherence processes involving the electrons in the sample bath.

This process is further visualized by the density matrices plotted for different times in fig. 2.6C. Before the pulse, the system is in thermal equilibrium determined by the Boltzmann distribution. At the end of the bias pulse, the populations have been pushed to the excited states and coherences have appeared on the off-diagonals between the first and second excited state. These coherences give rise to the oscillations in fig. 2.6B that decay exponentially with characteristic time T_2 as a result from the interaction with the sample bath. The average spin expectation value decays exponentially with characteristic time T_1 due to coupling to the bath. For times $t \gg T_1, T_2$ the system returns back to the thermal equilibrium state.

These calculations show that coupling to an incoherent bath can lead to a coherent quantum state in a coupled spin system. This is a somewhat counter-intuitive result as all interactions leading to this state are scattering events between incoherent electron and surface spins. The key realisation is that by coupling the tip bath to only a single atom in the spin system, the Kondo interaction only works on a single spin operator and doesn't couple to the eigenstates of the entire system. This introduces coherences into the density matrix (which is written in the energy basis) and thus induces dynamics from the Hamiltonian. This intriguing realisation opens the door to studying coherent spin physics where all the coherent driving is determined by fine-tuning the Hamiltonian of the system itself and we use incoherent tunneling electrons for both excitation and detection. In chapter 4, we perform the experiment shown in fig. 2.6B,C and discuss the physics behind this oscillation in detail.

REFERENCES

[1] D. Dai, H. Xiang, and M.-H. Whangbo. “Effects of spin-orbit coupling on magnetic properties of discrete and extended magnetic systems”. In: *Journal of computational chemistry* 29.13 (2008), pp. 2187–2209.

[2] D. J. Griffiths and D. F. Schroeter. *Introduction to quantum mechanics*. Cambridge university press, 2018.

[3] A. J. Heinrich, J. A. Gupta, C. P. Lutz, and D. M. Eigler. “Single-atom spin-flip spectroscopy”. In: *Science* 306.5695 (2004), pp. 466–469.

[4] F. D. Natterer, F. Donati, F. Patthey, and H. Brune. “Thermal and magnetic-field stability of holmium single-atom magnets”. In: *Physical review letters* 121.2 (2018), p. 027201.

[5] K. Yang, Y. Bae, W. Paul, F. D. Natterer, P. Willke, J. L. Lado, A. Ferrón, T. Choi, J. Fernández-Rossier, A. J. Heinrich, *et al.* “Engineering the eigenstates of coupled spin-1/2 atoms on a surface”. In: *Physical Review Letters* 119.22 (2017), p. 227206.

[6] M. Steinbrecher, W. M. Van Weerdenburg, E. F. Walraven, N. P. Van Mullekom, J. W. Gerritsen, F. D. Natterer, D. I. Badrtdinov, A. N. Rudenko, V. V. Mazurenko, M. I. Katsnelson, *et al.* “Quantifying the interplay between fine structure and geometry of an individual molecule on a surface”. In: *Physical Review B* 103.15 (2021), p. 155405.

[7] S.-h. Phark, Y. Chen, H. T. Bui, Y. Wang, M. Haze, J. Kim, Y. Bae, A. J. Heinrich, and C. Wolf. “Double-Resonance Spectroscopy of Coupled Electron Spins on a Surface”. In: *ACS nano* (2023).

[8] Y. Wang, M. Haze, H. T. Bui, W.-h. Soe, H. Aubin, A. Ardavan, A. J. Heinrich, and S.-h. Phark. “Universal quantum control of an atomic spin qubit on a surface”. In: *npj Quantum Information* 9.1 (2023), p. 48.

[9] K. Yang, S.-H. Phark, Y. Bae, T. Esat, P. Willke, A. Ardavan, A. J. Heinrich, and C. P. Lutz. “Probing resonating valence bond states in artificial quantum magnets”. In: *Nature communications* 12.1 (2021), p. 993.

[10] J. Kim, W.-j. Jang, T. H. Bui, D.-J. Choi, C. Wolf, F. Delgado, Y. Chen, D. Krylov, S. Lee, S. Yoon, *et al.* “Spin resonance amplitude and frequency of a single atom on a surface in a vector magnetic field”. In: *Physical Review B* 104.17 (2021), p. 174408.

[11] A. Spinelli, B. Bryant, F. Delgado, J. Fernández-Rossier, and A. F. Otte. “Imaging of spin waves in atomically designed nanomagnets”. In: *Nature materials* 13.8 (2014), pp. 782–785.

[12] U. Kamber, A. Bergman, A. Eich, D. Iuşan, M. Steinbrecher, N. Hauptmann, L. Nordström, M. I. Katsnelson, D. Wegner, O. Eriksson, *et al.* “Self-induced spin glass state in elemental and crystalline neodymium”. In: *Science* 368.6494 (2020), eaay6757.

[13] R. Toskovic, R. Van Den Berg, A. Spinelli, I. Eliens, B. Van Den Toorn, B. Bryant, J.-S. Caux, and A. Otte. “Atomic spin-chain realization of a model for quantum criticality”. In: *Nature Physics* 12.7 (2016), pp. 656–660.

[14] S. Loth, S. Baumann, C. P. Lutz, D. Eigler, and A. J. Heinrich. “Bistability in atomic-scale antiferromagnets”. In: *Science* 335.6065 (2012), pp. 196–199.

[15] F. Delgado, S. Loth, M. Zielinski, and J. Fernández-Rossier. “The emergence of classical behaviour in magnetic adatoms”. In: *Europhysics Letters* 109.5 (2015), p. 57001.

[16] A. A. Khajetoorians, J. Wiebe, B. Chilian, and R. Wiesendanger. “Realizing all-spin–based logic operations atom by atom”. In: *Science* 332.6033 (2011), pp. 1062–1064.

[17] A. Spinelli, M. Gerrits, R. Toskovic, B. Bryant, M. Ternes, and A. Otte. “Exploring the phase diagram of the two-impurity Kondo problem”. In: *Nature communications* 6.1 (2015), p. 10046.

[18] C. F. Hirjibehedin, C. P. Lutz, and A. J. Heinrich. “Spin coupling in engineered atomic structures”. In: *Science* 312.5776 (2006), pp. 1021–1024.

[19] T. Choi, W. Paul, S. Rolf-Pissarczyk, A. J. Macdonald, F. D. Natterer, K. Yang, P. Willke, C. P. Lutz, and A. J. Heinrich. “Atomic-scale sensing of the magnetic dipolar field from single atoms”. In: *Nature nanotechnology* 12.5 (2017), pp. 420–424.

[20] C. P. Slichter. *Principles of magnetic resonance*. Vol. 1. Springer Science & Business Media, 2013.

[21] E. Fermi. “Über die magnetischen Momente der Atomkerne”. In: *Zeitschrift für Physik* 60.5-6 (1930), pp. 320–333.

[22] J. A. Smith. “Nuclear quadrupole resonance spectroscopy. General principles”. In: *Journal of Chemical Education* 48.1 (1971), p. 39.

[23] F. Mabbs and D. Collison. “Electron paramagnetic resonance of d transition metal compounds”. In: *Studies in Inorganic Chemistry* 16 (1992), pp. 1–1306.

[24] S. Thiele, F. Balestro, R. Ballou, S. Klyatskaya, M. Ruben, and W. Wernsdorfer. “Electrically driven nuclear spin resonance in single-molecule magnets”. In: *Science* 344.6188 (2014), pp. 1135–1138.

[25] S. Loth, C. P. Lutz, and A. J. Heinrich. “Spin-polarized spin excitation spectroscopy”. In: *New Journal of Physics* 12.12 (2010), p. 125021.

[26] Y. Bae, K. Yang, P. Willke, T. Choi, A. J. Heinrich, and C. P. Lutz. “Enhanced quantum coherence in exchange coupled spins via singlet-triplet transitions”. In: *Science Advances* 4.11 (2018), eaau4159.

[27] F. Delgado and J. Fernández-Rossier. “Spin decoherence of magnetic atoms on surfaces”. In: *Progress in Surface Science* 92.1 (2017), pp. 40–82.

[28] G. Lindblad. “On the generators of quantum dynamical semigroups”. In: *Communications in Mathematical Physics* 48 (1976), pp. 119–130.

[29] V. Gorini, A. Kossakowski, and E. C. G. Sudarshan. “Completely positive dynamical semigroups of N-level systems”. In: *Journal of Mathematical Physics* 17.5 (1976), pp. 821–825.

[30] H. Mäkelä and M. Möttönen. “Effects of the rotating-wave and secular approximations on non-Markovianity”. In: *Physical Review A* 88.5 (2013), p. 052111.

[31] J. Reina-Gálvez, C. Wolf, and N. Lorente. “Many-body nonequilibrium effects in all-electric electron spin resonance”. In: *Physical Review B* 107.23 (2023), p. 235404.

[32] F. Delgado and N. Lorente. “A theoretical review on the single-impurity electron spin resonance on surfaces”. In: *Progress in Surface Science* 96.2 (2021), p. 100625.

[33] J. R. Johansson, P. D. Nation, and F. Nori. “QuTiP: An open-source Python framework for the dynamics of open quantum systems”. In: *Computer Physics Communications* 183.8 (2012), pp. 1760–1772.

[34] A. G. Redfield. “On the theory of relaxation processes”. In: *IBM Journal of Research and Development* 1.1 (1957), pp. 19–31.

[35] C. Cohen-Tannoudji, J. Dupont-Roc, and G. Grynberg. *Atom-photon interactions: basic processes and applications.* John Wiley & Sons, 1998.

[36] G. McCauley, B. Cruikshank, D. I. Bondar, and K. Jacobs. “Accurate Lindblad-form master equation for weakly damped quantum systems across all regimes”. In: *npj Quantum Information* 6.1 (2020), p. 74.

[37] R. S. Whitney. “Staying positive: going beyond Lindblad with perturbative master equations”. In: *Journal of Physics A: Mathematical and Theoretical* 41.17 (2008), p. 175304.

[38] A. M. Shakirov, Y. E. Shchadilova, A. N. Rubtsov, and P. Ribeiro. “Role of coherence in transport through engineered atomic spin devices”. In: *Physical Review B* 94.22 (2016), p. 224425.

[39] A. M. Shakirov, A. N. Rubtsov, A. I. Lichtenstein, and P. Ribeiro. “Relaxation and decoherence of qubits encoded in collective states of engineered magnetic structures”. In: *Physical Review B* 96.9 (2017), p. 094410.

3

EXPERIMENTAL TECHNIQUES

Wie het grote niet eert,
Is het kleine niet weerd

- Almost a Dutch proverb

In this chapter we will discuss the tools and techniques necessary (het grote) to be able to visualize, measure and manipulate single atoms on a surface (het kleine). We will start by explaining the basic working principle of scanning tunneling microscopy (STM) and describe the sample preparation studied in this thesis: Fe and Ti atoms on MgO/Ag(100). We create spin polarized tips by picking up Fe atoms which we use to read out the spin state of single Ti atoms. Using novel STM techniques electron spin resonance (ESR) and pump-probe spectroscopy we are able to manipulate and influence the spin states of individual atoms as well. These techniques will be central to the experiments presented in the later chapters of this thesis.

3.1. SCANNING TUNNELING MICROSCOPY

Conventional microscopy has, since its earliest invention in the seventeenth century in the form of elaborate magnifying glasses, been based on the scattering and refocusing of light. These early microscopes - for example those built by Antoni Van Leeuwenhoek in Delft - led to revolutions in biology, medicine and physics as they uncovered a previously hidden microworld [1]. These types of devices, however more sophisticated in the present day, are fundamentally limited in their magnification by the wavelength of the light that passes through them: the diffraction limit. By using a different medium like scattering electrons [2] instead of light waves, this problem can be mitigated as these particles can have wavelenghts < 1 nm. However, the measurement principle is the same: it reconstructs an image based on particles scattering off of the subject.

Scanning tunneling microscopy (STM), invented by Rohrer and Binnig in 1981 [3], is based on a different method entirely. Similar to the Braille reading and writing system designed for people who do not have access to detection of lightwaves, STM works by sensing the topography of a surface. A very sharp, conductive probe tip, ideally ending in a single atom, is brought in close proximity to a conductive surface until they are separated by vacuum gap only a few Ångstroms wide. By the fundamentally quantum mechanical principle of tunneling, electrons can jump through the vacuum between tip and sample [4]. Classically, this is deemed impossible as the energy needed to extract an electron from the material and put it into the vacuum is not overcome. The tunneling principle is illustrated in fig. 3.1A: electronic states live in either the sample or the tip electrode but can exist outside in the vacuum. The probability of finding an electron in the vacuum, however, decreases exponentially with the distance from surface. Therefore, when applying a bias voltage between tip and sample, a current will flow that is exponentially dependent on the distance between them:

$$I \propto e^{-kd} \tag{3.1}$$

with k the decay constant depending on the work function of the electronic states and d the distance between tip and sample. This exponential dependence is the source of the incredible spatial resolution of STM: displacing tip and sample by 1 Ångstrom can lead to an order of magnitude change in measured current [5, 6].

One of the reasons STM is such a fascinating and versatile tool for studying physics is that it can be used for more than just imaging surfaces. This sets it apart from the other, more conventional forms of microscopy based on scattering reflections introduced above. The flexibility of STM arises from the fact that the measured tunneling current also strongly depends on the density of states (DOS) of the tip, as well as the local density of states (LDOS) of the sample [7]:

$$I \propto \int_0^{eV} \rho_s(E_F - eV + \epsilon)\rho_t(E_F + \epsilon)d\epsilon \tag{3.2}$$

with E_F the Fermi energy and ρ_t and ρ_s the DOS of tip and sample. This means that by sweeping the bias applied between tip and sample, the convolution of the two den-

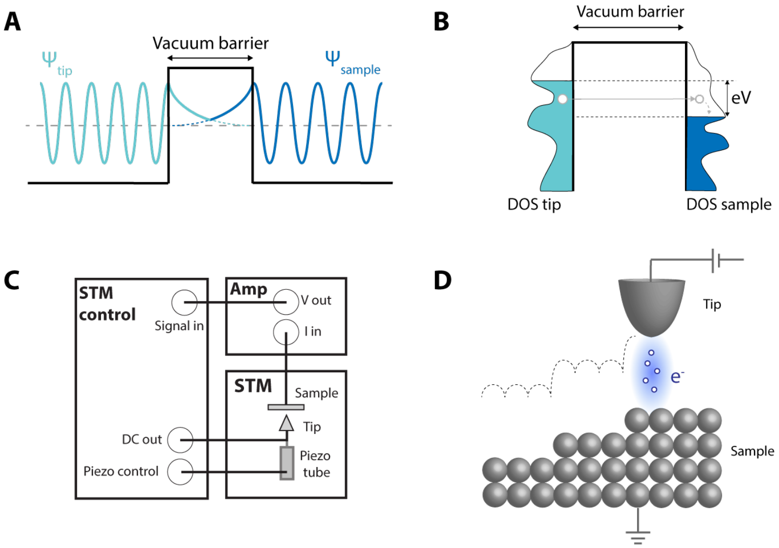

Figure 3.1: Working principle of a scanning tunneling microscope. A. Schematic illustration of the tunneling principle: electronic states decay exponentially into the vacuum. **B.** When a bias voltage is applied between tip and sample, a tunneling current can flow that is dependent on both the width of the vacuum barrier as well as the DOS of tip and sample. **C.** Schematic of an STM control loop. **D.** Schematic picture of the scanning motion of an STM tip in constant height mode.

sities of states can be measured. The principle is illustrated in fig. 3.1B: the number of electrons tunneling depends on the number of filled states in the bias window on one side and the number of empty states on the other. By moving the tip over the surface at different bias voltages, the variations in LDOS in the sample can be mapped. As can be deduced from section 3.1, the LDOS is proportional to the derivative of the current: the conductance. This allows STM to measure a plethora of surface phenomena: quasiparticle interference [8], band bending in semiconductors [9], field emission resonances [10] and surface magnetism (see section 3.5) [11] just to name a few.

To keep the tip at a constant separation with respect to the surface, the tip-sample distance is usually regulated via a feedback loop. A crude schematic of an STM control loop is shown in fig. 3.1C. The STM control electronics apply a bias between tip and sample which gives rise to a tunneling current. This current goes through a preamplifier and is fed back to the control system. There, a proportional/integral/differential (PID) feedback loop regulates the tip-sample distance via a piezotube attached to the STM tip to keep the current constant. The tip can also be moved sideways over the surface using the same piezotube. The resulting scanning motion is shown in fig. 3.1D: the tip follows the topography of the surface at a constant distance. All topographies shown in this thesis were made using constant current mode.

3.2. SAMPLE PREPARATION

All data shown in this thesis were acquired using a commercial Unisoku USM-1300 ^{3}He low temperature STM (see fig. 3.2A). The system has a base temperature of ~ 330 mK and is equipped with a vector magnet: up to 2 T in-plane and 9 T out-of-plane. The entire machine is floating on pressurized damping legs in order to minimize the effects of acoustic vibrations from the environment on the experiment. Inside the cryostat, the STM head itself is suspended on springs in an ultra-high vacuum (UHV) chamber kept at $\sim 10^{-10}$ mbar in order to prevent contamination of the surface. High frequency cabling runs from the input down to the tip in order to transmit radio-frequency (RF) signals as well as sharp DC pulses down to the junction. Outside the cryostat, multiple additional UHV chambers are connected to the system in order to prepare samples in-situ.

This thesis presents a variety of experiments conducted on a single surface preparation: Ti and Fe atoms evaporated onto bilayer MgO islands grown on top of a Ag(100) crystal. The exact same sample was used for chapter 5 and chapter 7 while new preparations of the same surface were made for chapter 4 and chapter 6. This sample preparation was first introduced by Yang et al. in 2017 [12] and has since become one of the most well-studied systems in the field as it has become a test bed for coherent spin physics using single atoms [13–20]. The different surface preparation steps are shown in fig. 3.2B. Here, we roughly follow the growth recipe from a number of previous publications [12, 21, 22] with minor adjustments. To obtain a clean Ag surface we first perform two cleaning cycles consisting of Ar sputtering and annealing in a UHV chamber separate from the STM. During sputtering, Ar gas is introduced into the chamber, ionized and accelerated to the sample by means of a high voltage. The inert Ar^+ ions collide with the sample and remove atomic layers in order to get rid of any surface contamination. Because this process results in a rough surface, we subsequently anneal the sample up to 650°C to let it reconstruct into atomically flat Ag terraces that can extend over several hundreds of nanometers. Next, we grow bilayer MgO islands by evaporating Mg atoms onto the sample in a 10^{-6} mbar O_2 atmosphere. During this process the sample is kept at a temperature of about 400°C. Finally, we cool down the sample to 1.5 K for single atom deposition. As our machine does not allow for cold evaporation, we take out the sample from the cryostat for ~ 30 seconds to expose it to a flow of Fe and Ti atoms after which we immediately return it to the fridge. We estimate that during this time the sample warms up to ~ 80 K, however, we still achieve a clean deposition of single atoms without visible clustering. It is theorized that the Ti atoms become hydrogenated on the surface immediately due to residual H_2 gas in the vacuum chamber [12, 23], reducing their electron spin moment to $\frac{1}{2}$ and leaving the orbital moment partially unquenched when bound to the MgO surface. The Fe atoms exhibit a total electron spin of $S = 2$ on the MgO surface [24, 25]. The resulting surface is shown in the topography image in fig. 3.2C: a single 30 nm times 30 nm square MgO island lays next to an atomic step in the Ag crystal. White protrusions are single Fe and Ti adatoms. In fig. 3.2D we show an atomic resolution image of the MgO lattice. Here, white protrusions are the O atoms of the top MgO layer [21]. These topographies confirm that we obtain atomically pristine islands and allow us to determine the angle between the MgO lattice and the applied in-plane magnetic field which is aligned with the scan direction of the STM. We find an angle of ~ 14°.

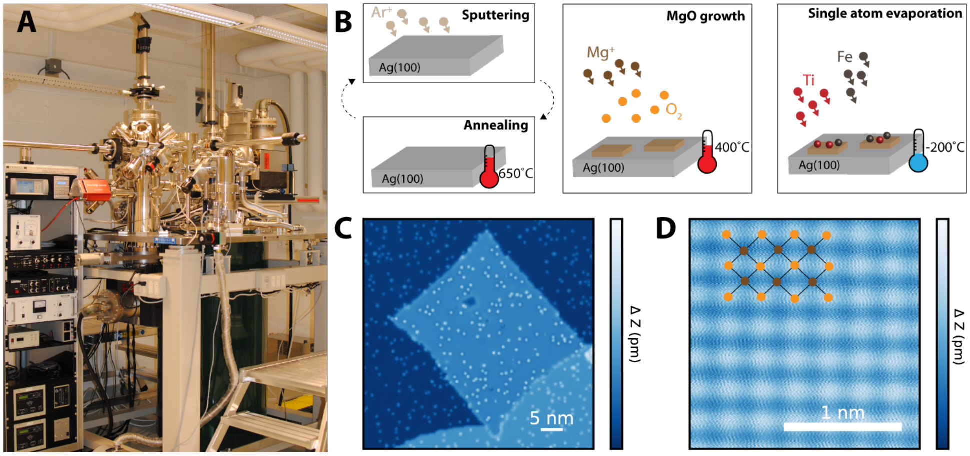

Figure 3.2: Experimental setup and sample preparation. **A.** Picture of the Unisoku USM-1300 STM system in Delft. **B.** schematic pictures of the preparation steps for Ti and Fe atoms on MgO/Ag(100). From left to right: (i) cleaning cycles consisting of Ar sputtering and annealing (ii) MgO growth by evaporating Mg in an oxygen atmosphere (iii) evaporation of Fe and Ti atoms. **C.** STM topography of Ti and Fe atoms on a single bilayer MgO island on top of a Ag(100) crystal (setpoint: 60 mV, 20 pA). **D.** atomic resolution image of an MgO island (setpoint: 4 mV, 8 nA).

3.3. ATOM MANIPULATION

The fact that the tip is in such close proximity to the surface sets STM apart from other microscopy methods for another reason: it allows not just for imaging of the surface but also to interact with it. When the tip is brought close to a surface, it creates a very localized potential well due to both van der Waals forces and electrostatic forces between tip and sample [26–28]. Ti adatoms on MgO can be moved via lateral manipulation, meaning that they can be dragged or pushed over the surface by the tip. In fig. 3.3A-C we schematically show the steps for lateral atom manipulation. First, we bring the STM tip close to the adatom (setpoint: 380 mV, ~ 5 nA). Then, we move the tip slowly to a new position and monitor the tip-sample distance to check whether the adatom follows. At the desired location, we ramp down the voltage and increase the tip-sample distance. The panels in fig. 3.3D-F show three consecutive atomic manipulations of a Ti atom over a single lattice site. First, it is bound to a bridge site between to O atoms (D). It is then moved to a binding site on top of a single O, thereby drastically decreasing its apparent height in the STM topography (E). Finally, it is moved up once more to a bridge site (F). These two types of binding site are the only positions on which single titanium atoms have been found on the MgO surface [12].

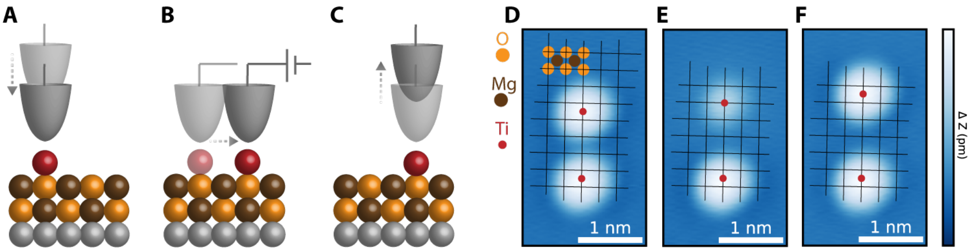

Figure 3.3: Lateral atom manipulation of Ti atoms on MgO. A-C. Three steps of lateral manipulation. First (**A**), the tip is brought into close proximity with the adatom. Then (**B**), a large bias is applied and the tip is moved over the surface. The Ti atom is trapped in the local potential well and follows the tip. Finally (**C**), the applied bias is reduced and the tip withdrawn, leaving the Ti atom in the desired location. **D-F** consecutive STM topographies showing the manipulation of a Ti atom over a single lattice site (setpoint: 50 mV, 20 pA). Schematic MgO lattice is overlaid derived from the atomic resolution topography in fig. 3.2D. First (**D**), both atoms are on bridge sites. Then (**E**), the top atom is move half a lattice site to an O-site. Finally (**F**), the top atom is move again to another bridge site.

Some atoms, such as Fe on MgO, are bound too tightly to the surface to be moved via lateral manipulation. They can be moved via vertical manipulation: in that case the tip is brought so close that the adatom leaves the surface entirely and jumps onto the STM tip [29]. Then the tip can be moved and the atom can be dropped off again in a different place. In this thesis we use this technique to pick up Fe atoms from the MgO islands in order to obtain spin polarized contrast (see section 3.5) .

3.4. INELASTIC ELECTRON TUNNELING SPECTROSCOPY

In addition to being able to manipulate single atoms on a surface, STM allows us to perform local spectroscopy. The signatures in the LDOS of a single atom serve as a fingerprint for identification of atomic species [22, 24, 30], and furthermore, of how that atom interacts with its local environment. Of particular interests are inelastic processes, where an electron arrives with enough energy to produce an excitation of the atom. This technique, known as inelastic electron tunnelling spectroscopy (IETS) and be used to study processes that involve vibrational [31], orbital [22, 32] or spin excitations [30].

The underlying principle of IETS measurements is the inelastic co-tunneling of electrons resulting in single atom spin excitations (see fig. 3.4A). Tunneling electrons with opposite spin to that of the atom's unpaired electron are able to tunnel onto the adatom. This brings the atom into a virtual state as the Coulomb energy needed to add an extra electron to the orbital is not provided. Therefore, one of the two electrons has to tunnel out of the atom within the time set by the Heisenberg uncertainty principle. Depending on which electron leaves, the spin state of the atom remains unchanged ($\Delta m = 0$) or may change ($\Delta m = \pm 1$) if the electron tunneling onto the atom had enough energy to account for the spin flip process ($eV > \Delta E$). The same process applies to tunneling holes, resulting in the same possible final states but with an empty intermediate virtual state [33].

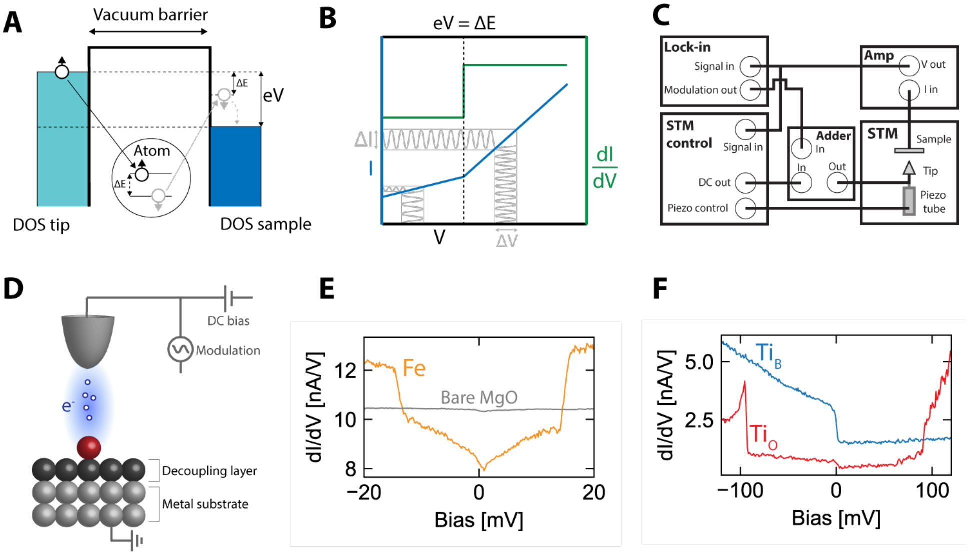

Figure 3.4: Inelastic electron tunneling spectroscopy. **A.** Schematic picture of inelastic spin-flip tunneling. When the applied bias overcomes the spin excitation energy a new conduction channel opens. **B.** Schematic picture of an IETS measurement. At the voltage threshold the slope in the IV curve (blue) changes corresponding to a step in the conductance (green). Lock-in voltage modulation and resulting current modulation show in grey. **C.** Wiring schematic for a conductance measurement involving a lock-in amplifier. **C.** Schematic picture of the tunnel-junction during an IETS measurement. The atomic spin under investigation is placed on a thin insulating layer to decouple it from the electron bath in the meta substrate. **E.** $\frac{dI}{dV}$ measurements on bare MgO (grey) and Fe on MgO (orange). The Fe atom shows characteristic IETS steps at ±14 mV (setpoint: 20 mV, 200 pA). **F.** $\frac{\mathrm{d}I}{\mathrm{d}V}$ measurements on Ti atoms adsorbed on top of an O-site (red, setpoint: 120 mV, 60 pA) and on a bridge site in between to O atoms (blue, setpoint: 120 mV, 500 pA).

We measure these processes by sweeping the bias and measuring the differential conductance $\frac{\mathrm{d}I}{\mathrm{d}V}$ through a single atom. When the bias reaches the threshold for a spin-flip process, a new inelastic tunneling channel opens. This appears as a stepwise increase in the conductance spectrum as illustrated in fig. 3.4B. We measure the conductance directly via a lock-in measurement: on top of the DC bias we add a modulation voltage which is converted to a modulated current of the same frequency at the tip-sample junction. The amplitude of this modulation current is a direct measurement of the slope of the I-V curve: the conductance. In fig. 3.4C we show a typical wiring diagram for IETS measurements using a lock-in amplifier (in our case a Stanford Research SR830).

In order to detect spin-flip transitions in single atoms, the electronic spin state should be sufficiently decoupled from the electrons in the substrate bath. Therefore, single magnetic atoms are placed on top of ultra thin insulating films consisting of only one to several atomic layers in order to separate the spin from the metallic substrate (see fig. 3.4D). This has two main effects on the atomic spin: it allows the spin states of the atom to be sufficiently long-lived to be detected and it induces a crystal field that gives rise to magnetic anisotropy splitting. In previous experiments, spin-flip IETS measurements have revealed these local anisotropy energies induced by the underlying lattice [34] as well as spin interaction between atoms in nanoscale magnetic structures [35, 36] and emergent spin waves in atomic chains [37] among other phenomena. In this thesis we leverage this technique for atom identification, as well as for in-situ characterization of the functionalized tip.

The fist step when starting an experiment on a new area of the MgO/Ag(100) surface is to identify the atomic species using IETS measurements. As can be seen in fig. 3.4E, bare MgO has a flat conductance spectrum at low biases. However, when the tip is placed over an Fe atom bound atop an O-site, we find characteristic steps in the spectrum at ±14 mV due to the surface induced anisotropy energy [24]. For Ti atoms we find a spin-flip transition at energies very close to 0. This is because Ti on MgO is a spin-$\frac{1}{2}$ system and therefore does not experience any anisotropy spin splitting. The spin states are therefore split solely by the Zeeman energy which is only ~ 50 µeV at a field of 500 mT, barely resolvable for IETS. The two possible binding sites for Ti are clearly distinguishable in their conductance spectra by the presence of an extra pair of steps at ~ 90 mV for Ti bound on the O-site (see fig. 3.4F). These steps have been identified as orbital excitations of the combined Ti-H system [23].

3.5. SPIN POLARIZED STM

As mentioned in the previous section, next to atom identification, we employ IETS measurements to check the functionalization of our STM tip as well. During these measurements we look for large spin polarized contrast which we achieve by transferring Fe atoms from the surface to the tip apex by picking them up [38]. This cluster of Fe atoms at the tip apex induces magneto-resistance in the tunneling current: the measured tip-sample conductance depends on the magnetic orientation of the surface relative to the magnetization direction of the tip [11, 39].

Spin polarized contrast appears in both elastic and inelastic tunneling channels. We visualize both contributions in fig. 3.5 by considering the spin flip tunneling processes and the spin split density of states of a magnetic STM tip. When a sufficiently large external magnetic field is applied to the sample ($E_{\text{Zeeman}} > k_B T$), the spin of the adatom will follow the field direction. In this case, as the total spin (consisting of atomic spin number m and tunneling electron spin number σ) must be conserved during a scattering event ($\Delta m + \Delta\sigma = 0$), only electrons with spin opposite to the external field can cause a spin flip in the atom (see section 3.5A). The tunneling electron and the atom exchange their spin state. The amount of electrons polarized in this direction that tunnel through the atom is highly dependent on the direction of the applied bias. This is due to the spin splitting of the DOS of the tip and is illustrated in section 3.5B. In this example, the tip has a majority spin polarisation down (aligned with the external) field while the sample

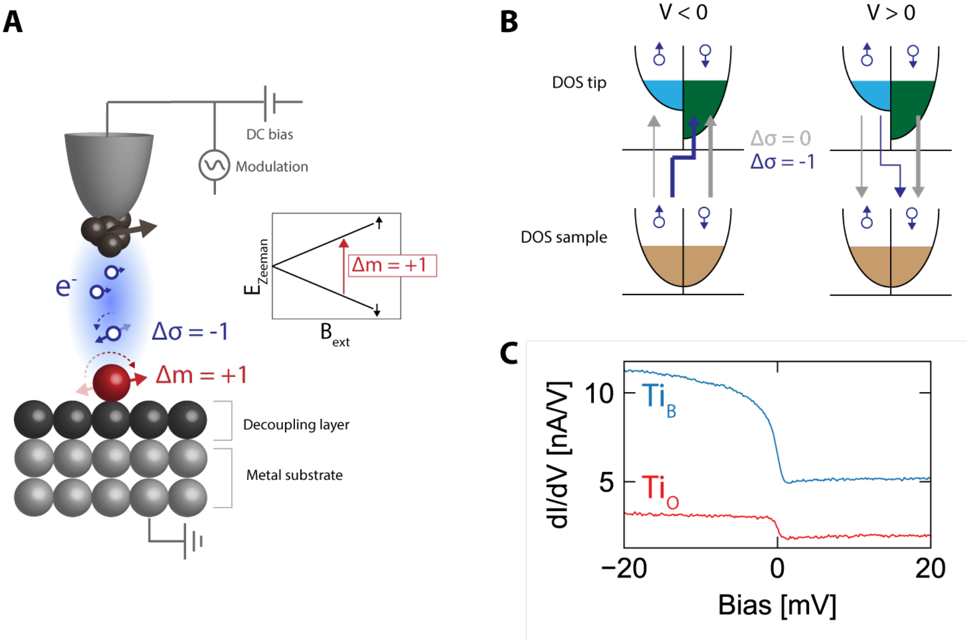

Figure 3.5: Spin polarized STM. A. Schematic picture of atomic spin flips induced by tunneling electrons. Tunneling electrons with spin opposite to the groundstate direction of the atom can cause spin flip excitations by exchanging their spin with the atom in a scattering process. **B.** Schematic representation of the tunneling paths between the spin polarized DOS of the tip and spin averaged DOS of the sample. By convention, the bias is given with respect to the sample in contrast to the experimental bias which is applied to the tip as shown in **A**. **C.** IETS measurements of the spin excitation on Ti atoms on different binding sites taken with a spin polarized tip (setpoint $\mathrm{Ti_B}$: 20mV, 200 pA; setpoint $\mathrm{Ti_O}$: 20 mV, 60 pA).

(excluding the adatom) is spin averaged. The elastic tunneling channels ($\Delta\sigma = 0$, grey) are symmetric with respect to the sign of the applied bias. The single inelastic channel that is able to cause a spin flip in the atom ($\Delta\sigma = -1$, blue) is asymmetric however, as it involves only one of the spin directions of the tip bath.

The amount of inelastic spin polarization of the tip can be determined from IETS measurements [33]. In section 3.5C we show close up measurements of the spin excitation of Ti atoms on both binding sites. Due to the large spin polarization of the tip, the step at negative bias is very large while the step at positive bias is almost indiscernible. When the rate of spin flips occurring due to tunneling electrons starts to compete with the relaxation rate, the average spin state of the atom can be changed [40]. This effect is known as spin pumping and will be of importance for the experiments discussed in this thesis. It will be the main tool with which we manipulate the spin states of individual Ti atoms.

3.6. ELECTRON SPIN RESONANCE

Resonant magnetic phenomena in solids and solutions have been studied since the late 1930s, giving unprecedented insight into the magnetic properties of bulk materials. In general, this could be done by either detecting spin transitions between nuclear spins (nuclear magnetic resonance, NMR) [41] or electron spins (electron spin resonance, ESR) [42]. These transitions can also be driven in a different ways, for example by applying oscillating electric fields or magnetic fields [43]. The implementation of ESR inside an STM in 2015 combined the superior energy resolution of a magnetic resonance technique with the spatial resolution and atomic control capabilities of STM [25]. Instead of measuring ensemble averages of bulk materials, spin transitions could now be measured on individual atoms and molecules on a surface. Here, we will give a brief description of the technique as it is used extensively throughout this thesis.

To perform an ESR-STM measurement, we need to transmit sufficient amplitude radio frequency (RF) voltage to the STM junction. This can be done in two ways: (i) by combining the RF signal with the DC voltage outside of the STM and sending both to the tip via the same cabling [44–46]. Or (ii) by installing an antenna in the STM head and sending the RF voltage via a separate line [47, 48]. In the Unisoku machine used in this thesis, we make use of the first method. The downside to this method is that the cabling can be harder to install and transmission losses will occur at the point where the cable is connected to the tip. The benefit is that this setup is also capable of sending sharp DC pulses (needed for pump-probe spectroscopy, see section 3.7) to the tip via the same cabling. This is harder to do with an RF antenna as it couples capacitively to the tip, transmitting only high frequency signals and omitting the low frequency components of DC pulses. Our cabling scheme is shown in fig. 3.6A. The RF signal is chopped at a few hundred Hertz in order to detect changes in the tunneling current induced by the RF voltage via a lock-in measurement. It is combined with the DC bias in the bias tee (Tektronix PSPL5542) outside the cryostat and sent to the tip via the same high frequency cable.

The microscopic working principle of ESR-STM is still under debate as of the writing of this thesis and there currently is an active effort going on to find theoretical models to understand the driving mechanism in detail [49–51]. For an overview of all proposed theoretical models see [52]. Here, we will briefly discuss the most commonly accepted explanation first introduced by [53], corroborated by experimental investigation [15]. The core idea is that the atom on an MgO surface has a piezoelectric response to the oscillating electric field (see fig. 3.6B). Since we are using a spin polarized STM tip, a highly localised magnetic field is emanating from the Fe cluster on the tip apex [54]. The electric field moves the atom up and down with the applied RF frequency in this inhomogeneous magnetic field of the STM tip. If the direction of the tip field and the atomic spin don't perfectly align, the atom will experience an oscillating B-field component perpendicular to its magnetization axis. This oscillating magnetic field is able to drive $\Delta m = \pm 1$ transitions of the atomic spin [43]. For the spin-2 case of Fe on MgO, calculations show that the component of this oscillating field parallel to the magnetization axis can drive $\Delta m = \pm 4$ transitions between the spin states [15].

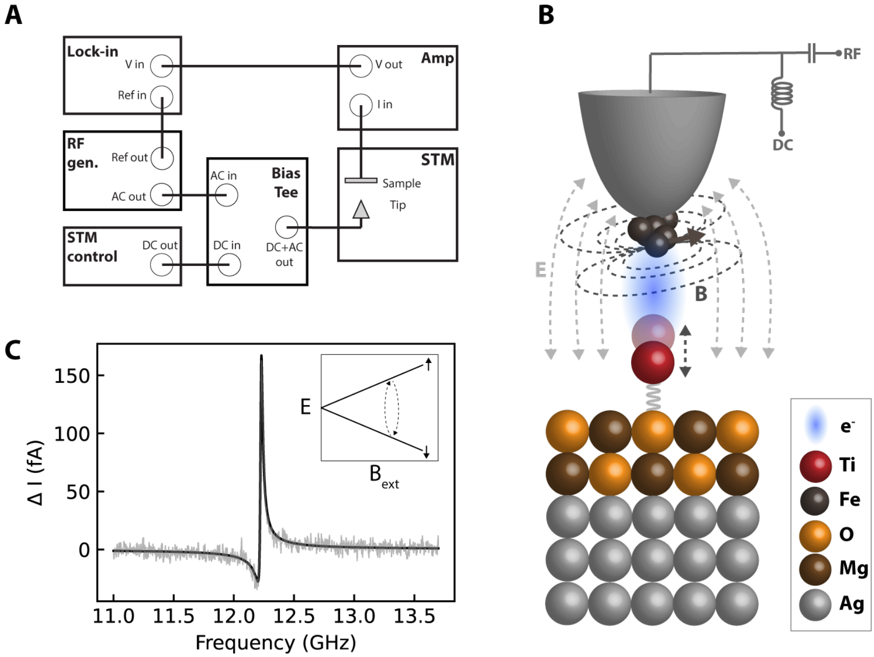

Figure 3.6: Working principle of ESR-STM. A. Wiring schematic of an ESR-STM experiment. The RF voltage is chopped at the lock-in frequency and combined with the DC voltage at the bias tee outside the STM. **B.** Schematic picture of the working principle of ESR-STM. The adatom undergoes a piezoelectric response to the applied RF electric field. This results in the atom shaking up and down in the anisotropic magnetic field emanating from the magnetic STM tip, driving spin transitions. Spin polarized tunneling electrons measure the change in average population of the adatom spin states. **C.** Typical ESR-STM measurement of a single Ti$_B$ atom (Setpoint: 10 pA, 60 mV, $V_{RF} = 25$ mV, $B_{ext} = 480$ mT). Inset: Energy diagram of the spin states split by Zeeman interaction with the external magnetic field.

The resulting signal is measured through the spin polarized current: the time-averaged spin state of the atom is changed when the driving frequency matches the spin state energy splitting. When no RF is applied, the atomic spin should theoretically be distributed between up and down via the Boltzmann distribution which is determined by temperature. In contrast, when RF is applied at the resonance frequency the spin is continually driven back and forth between up and down, averaging over time to a 50-50 distribution. The spin contrast between these two populations gives rise to the contrast in the spin polarized current. A typical measurement on a single Ti$_B$ atom is shown in fig. 3.6C: the frequency is swept while the applied field and tip-sample distance are held constant. Around 12.2 GHz we see a sharp resonance indicating the spin transition. We fit the resonance with a Fano lineshape [55]:

$$\Delta I = I_{\text{peak}} \frac{1+\delta\cdot 2q}{1+\delta^2} \tag{3.3}$$

with $\delta = \frac{f-f_0}{\Gamma/2}$ with Γ the resonance line width, I_{peak} the maximium amplitude of the resonance and q being the Fano parameter that determines the asymmetry of the resonance peak. We need to emphasize here that there is no underlying physics involving interference between different scattering amplitudes that usually gives rise to a Fano line-shape. The actual ESR line shape is much more complex: the asymmetry originates from a homodyne contribution to the measured signal [13, 15, 56, 57]. However, for the purposes of this thesis – to only extract a resonance frequency – we consider fitting ESR spectra with a Fano line-shape to suffice.

The population argument we just presented above, giving rise to the spin contrast, suggests that the ESR signal amplitude is highly dependent on the Boltzmann factor: $I_{\mathrm{peak}} \propto e^{\frac{\Delta E}{k_{\mathrm{B}}T}}$. However, this is not always the case as we can see from the measurements on a single $\mathrm{Ti_B}$ presented in fig. 3.7A. Here, we sweep the RF voltage from 500 MHz to 11 Ghz for different external fields ranging from 360 mT all the way down to 0 T. The experimental temperature of ~ 400 mK should result in a gradual decrease in signal amplitude around 8 GHz according to the Boltzmann factor, however, we observe large signal amplitudes down to $B_{\mathrm{ext}} = 0$. We attribute this to spin pumping caused by the spin polarized tunneling current. This effect, that pushes the population to one of the spin states, competes with the ESR driving, which pushes the population to equality, creating measurable contrast. This mechanism allows for ESR-STM measurements on energy scales that should otherwise not be possible due to temperature constraints.

To achieve constant amplitude frequency sweeps at the tip-sample junction, the transfer function has to be compensated for. This is done by measuring the transfer function and sending the inverse at the output of the RF generator [45, 58]. In fig. 3.7B we show the amplitude transfer function of our STM over this frequency range. This is the amount of RF power lost as a function of frequency due to imperfections in the cabling down to the tip. For $f > 5$ GHz we experience significant losses in the order of -35 dBm. The lost RF power is converted locally into heat as can be seen from the temperature measurements at the sample stage while performing a compensated frequency sweep in fig. 3.7C. For frequencies $f > 5$ GHz the sample warms up significantly, correlating with the amount of RF power lost.

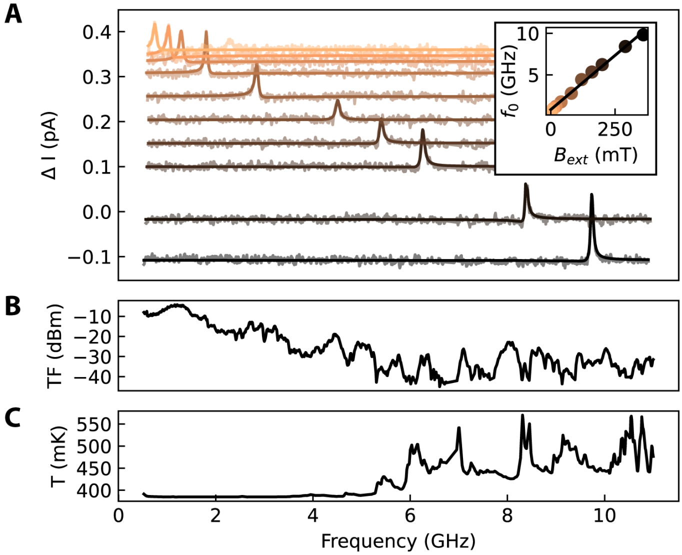

Figure 3.7: ESR-STM measurements at low frequencies. A. ESR measurements on a single $\mathrm{Ti_B}$ atom (Setpoint: 50 pA, 60 mV, $V_{\mathrm{RF}} = 10$ mV, $B_{\mathrm{ext}} = 0-360$ mT). Inset: Resonance frequencies determined by Fano fits through the frequency sweeps. A fit through the shifting resonance frequencies shows the linear relationship of the Zeeman energy splitting with external field. **B.** Transfer function of the Unisoku STM in Delft from 500 Mhz to 11 GHz. **C.** sample temperature measured during a compensated frequency sweep over the same range.

3.7. PUMP-PROBE SPECTROSCOPY

The final technique that we will discuss in this chapter is also the most central to this thesis: pump-probe spectroscopy. Before the introduction of this technique in 2010 [59], STM measurements were limited in time resolution by the bandwidth of the pre-amplifier needed to record very small currents. As many STM experiments consist of measuring currents < 1 nA, low noise amplifiers are used with gains in the range of 10^9, resulting in frequency cutoffs around 100 kHz. This puts many dynamical processes at the atomic scale out of the measurable range as these tend to happen at MHz [59, 60], GHz [13, 61] or even THz [62, 63] timescales.

Pump-probe spectroscopy bypasses the bandwidth limitations of the pre-amplifier by sending a pulse train instead of a DC voltage. This pulse train consists of a pump pulse that excites the atomic spin via spin flip excitations caused by the tunneling electrons, followed by a probe pulse after some time t that reads the spin state via magnetoresistance. The process is illustrated in fig. 3.8A. The pulse train is repeated many times in the first half of a lock-in cycle; in the second half the same pulse train is sent but either the probe is removed or its polarity is inverted [64]. The resulting lock-in signal consists of the difference between the two cycles: the electrons tunneling during the probe pulse. By varying the time t between the pump and probe pulses the evolution of the spin after the pump pulse can be traced out.

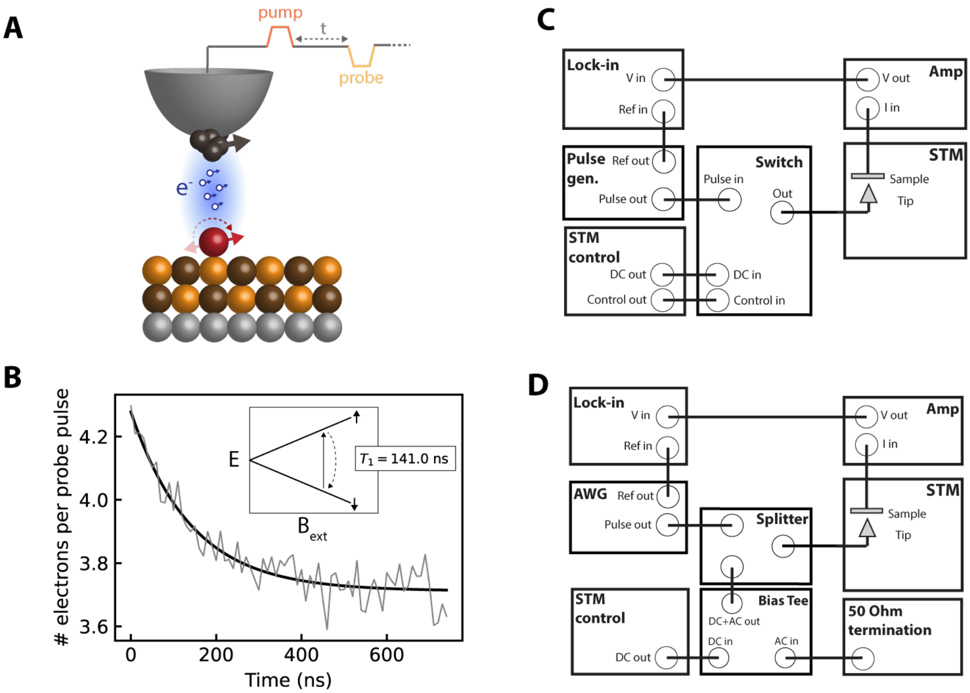

Figure 3.8: Pump-probe spectroscopy. **A.** schematic picture of pump-probe spectroscopy. During the pump pulse, tunneling electrons can cause flip-flip excitations in scattering events. In the subsequent waiting time t, the atomic spin is freely evolving, after which it is measured via magnetoresistance during the probe pulse. **B.** Example measurement of the relaxation time T_1 of a single Ti$_B$ atom (setpoint: 60 mV, 5 pA, T = 400 mK, pulse width: 50 ns, $V_{\text{pump}} = +100$ mV, $V_{\text{probe}} = -100$ mV). **C.** wiring diagram used for pump-probe measurements in chapters 4 to 6. **D.** wiring diagram used for pump-probe measurements in chapter 7.

Previously, the technique was exclusively used for spin relaxation time (T_1) measurements [59]. An example measurement of the T_1 time of a single Ti$_B$ atom is shown in fig. 3.8B. Here, $t = 0$ is the moment where the pump and probe pulses immediately follow each other. The vertical axis is converted to the number of electrons that tunnel during a single probe pulse. Due to the change in spin state during the relaxation process, the current measured during the probe pulse drops exponentially. We extract a relaxation time by fitting the following function:

$$I_{\text{probe}} = A + e^{-t/T_1}. \tag{3.4}$$

For the Ti$_B$ case we find a relaxation time of $T_1 = 141 \pm 13$ ns.

We use two different setups to generate and transmit square DC pulses to the STM junction. The scheme used for chapters 4 to 6 is shown in fig. 3.8C and consists of a Agilent 81110A pulse generator connected to a Mini Circuits ZYSWA-2-50DR switch. For each measurement, the tip is positioned at the desired current setpoint above the center of the adatom after which the regulation feedback was turned off. The switch was then engaged so the DC bias was disconnected and only the pulse train was sent to the tip-sample junction. For the experiments in chapter 7 we used the setup shown in fig. 3.8D. Here, we worked with a Keysight M8195a arbitrary waveform generator (AWG) to generate DC pulses. The pulses are added to the DC bias via a splitter (Mini-Circuits ZFRSC-183-S+) and sent to the tip. To minimize reflections of the DC pulses into the wiring, we run the DC bias through the DC input of a bias tee, with a 50 Ohm termination the AC side.

In the following chapters we will use pump probe spectroscopy combined with separate ESR-STM measurements to study the coherent evolution of a single spin excitation in different configurations of Ti atoms on an MgO/Ag(100) surface. These experiments show that it is possible to not only measure exponential spin decays using this technique, but also coherent spin dynamics.

REFERENCES

[1] J. van Zuylen. “The microscopes of Antoni van Leeuwenhoek”. In: *Journal of microscopy* 121.3 (1981), pp. 309–328.

[2] M. Knoll and E. Ruska. “Das elektronenmikroskop”. In: *Zeitschrift für physik* 78 (1932), pp. 318–339.

[3] G. Binnig and H. Rohrer. “Scanning tunneling microscopy”. In: *Surface science* 126.1-3 (1983), pp. 236–244.

[4] C. J. Chen. *Introduction to Scanning Tunneling Microscopy Third Edition*. Vol. 69. Oxford University Press, USA, 2021.

[5] G. Binnig, H. Rohrer, C. Gerber, and E. Weibel. “Tunneling through a controllable vacuum gap”. In: *Applied Physics Letters* 40.2 (1982), pp. 178–180.

[6] G. Binnig, H. Rohrer, C. Gerber, and E. Weibel. “7×7 reconstruction on Si (111) resolved in real space”. In: *Physical review letters* 50.2 (1983), p. 120.

[7] J. Bardeen. “Tunnelling from a many-particle point of view”. In: *Physical review letters* 6.2 (1961), p. 57.

[8] J. Hoffman, K. McElroy, D.-H. Lee, K. Lang, H. Eisaki, S. Uchida, and J. Davis. “Imaging quasiparticle interference in Bi2Sr2CaCu2O8+ δ”. In: *Science* 297.5584 (2002), pp. 1148–1151.

[9] Z. Zhang and J. T. Yates Jr. “Band bending in semiconductors: chemical and physical consequences at surfaces and interfaces”. In: *Chemical reviews* 112.10 (2012), pp. 5520–5551.

[10] G. Binnig, K. Frank, H. Fuchs, N. Garcia, B. Reihl, H. Rohrer, F. Salvan, and A. Williams. “Tunneling spectroscopy and inverse photoemission: image and field states”. In: *Scanning Tunneling Microscopy* (1993), pp. 93–96.

[11] R. Wiesendanger. “Spin mapping at the nanoscale and atomic scale”. In: *Reviews of Modern Physics* 81.4 (2009), p. 1495.

[12] K. Yang, Y. Bae, W. Paul, F. D. Natterer, P. Willke, J. L. Lado, A. Ferrón, T. Choi, J. Fernández-Rossier, A. J. Heinrich, *et al.* “Engineering the eigenstates of coupled spin-1/2 atoms on a surface”. In: *Physical Review Letters* 119.22 (2017), p. 227206.

[13] K. Yang, W. Paul, S.-H. Phark, P. Willke, Y. Bae, T. Choi, T. Esat, A. Ardavan, A. J. Heinrich, and C. P. Lutz. “Coherent spin manipulation of individual atoms on a surface”. In: *Science* 366.6464 (2019), pp. 509–512.

[14] K. Yang, S.-H. Phark, Y. Bae, T. Esat, P. Willke, A. Ardavan, A. J. Heinrich, and C. P. Lutz. “Probing resonating valence bond states in artificial quantum magnets”. In: *Nature communications* 12.1 (2021), p. 993.

[15] T. S. Seifert, S. Kovarik, D. M. Juraschek, N. A. Spaldin, P. Gambardella, and S. Stepanow. “Longitudinal and transverse electron paramagnetic resonance in a scanning tunneling microscope”. In: *Science Advances* 6.40 (2020), eabc5511.

[16] **L. M. Veldman**, L. Farinacci, R. Rejali, R. Broekhoven, J. Gobeil, D. Coffey, M. Ternes, and A. F. Otte. “Free coherent evolution of a coupled atomic spin system initialized by electron scattering”. In: *Science* 372.6545 (2021), pp. 964–968.

[17] Y. Wang, M. Haze, H. T. Bui, W.-h. Soe, H. Aubin, A. Ardavan, A. J. Heinrich, and S.-h. Phark. “Universal quantum control of an atomic spin qubit on a surface”. In: *npj Quantum Information* 9.1 (2023), p. 48.

[18] S.-h. Phark, Y. Chen, H. T. Bui, Y. Wang, M. Haze, J. Kim, Y. Bae, A. J. Heinrich, and C. Wolf. “Double-Resonance Spectroscopy of Coupled Electron Spins on a Surface”. In: *ACS nano* (2023).

[19] P. Willke, Y. Bae, K. Yang, J. L. Lado, A. Ferrón, T. Choi, A. Ardavan, J. Fernández-Rossier, A. J. Heinrich, and C. P. Lutz. “Hyperfine interaction of individual atoms on a surface”. In: *Science* 362.6412 (2018), pp. 336–339.

[20] P. Willke, K. Yang, Y. Bae, A. J. Heinrich, and C. P. Lutz. “Magnetic resonance imaging of single atoms on a surface”. In: *Nature Physics* 15.10 (2019), pp. 1005–1010.

[21] S. Baumann, I. G. Rau, S. Loth, C. P. Lutz, and A. J. Heinrich. “Measuring the three-dimensional structure of ultrathin insulating films at the atomic scale”. In: *ACS nano* 8.2 (2014), pp. 1739–1744.

[22] I. G. Rau, S. Baumann, S. Rusponi, F. Donati, S. Stepanow, L. Gragnaniello, J. Dreiser, C. Piamonteze, F. Nolting, S. Gangopadhyay, *et al.* “Reaching the magnetic anisotropy limit of a 3 d metal atom”. In: *Science* 344.6187 (2014), pp. 988–992.

[23] M. Steinbrecher, W. M. Van Weerdenburg, E. F. Walraven, N. P. Van Mullekom, J. W. Gerritsen, F. D. Natterer, D. I. Badrtdinov, A. N. Rudenko, V. V. Mazurenko, M. I. Katsnelson, *et al.* “Quantifying the interplay between fine structure and geometry of an individual molecule on a surface”. In: *Physical Review B* 103.15 (2021), p. 155405.

[24] S. Baumann, F. Donati, S. Stepanow, S. Rusponi, W. Paul, S. Gangopadhyay, I. Rau, G. Pacchioni, L. Gragnaniello, M. Pivetta, *et al.* “Origin of perpendicular magnetic anisotropy and large orbital moment in Fe atoms on MgO”. In: *Physical review letters* 115.23 (2015), p. 237202.

[25] S. Baumann, W. Paul, T. Choi, C. P. Lutz, A. Ardavan, and A. J. Heinrich. “Electron paramagnetic resonance of individual atoms on a surface”. In: *Science* 350.6259 (2015), pp. 417–420.

[26] D. M. Eigler and E. K. Schweizer. “Positioning single atoms with a scanning tunnelling microscope”. In: *Nature* 344.6266 (1990), pp. 524–526.

[27] M. Ternes, C. P. Lutz, C. F. Hirjibehedin, F. J. Giessibl, and A. J. Heinrich. “The force needed to move an atom on a surface”. In: *Science* 319.5866 (2008), pp. 1066–1069.

[28] J. A. Stroscio and R. J. Celotta. “Controlling the dynamics of a single atom in lateral atom manipulation”. In: *Science* 306.5694 (2004), pp. 242–247.

[29] L. Bartels, G. Meyer, and K.-H. Rieder. “Basic steps of lateral manipulation of single atoms and diatomic clusters with a scanning tunneling microscope tip”. In: *Physical Review Letters* 79.4 (1997), p. 697.

[30] A. J. Heinrich, J. A. Gupta, C. P. Lutz, and D. M. Eigler. “Single-atom spin-flip spectroscopy”. In: *Science* 306.5695 (2004), pp. 466–469.

[31] L. Lauhon and W. Ho. “Single-molecule vibrational spectroscopy and microscopy: CO on Cu (001) and Cu (110)”. In: *Physical Review B* 60.12 (1999), R8525.

[32] R. Rejali, D. Coffey, J. Gobeil, J. W. González, F. Delgado, and A. F. Otte. “Complete reversal of the atomic unquenched orbital moment by a single electron”. In: *npj Quantum Materials* 5.1 (2020), p. 60.

[33] M. Ternes. “Spin excitations and correlations in scanning tunneling spectroscopy”. In: *New Journal of Physics* 17.6 (2015), p. 063016.

[34] C. F. Hirjibehedin, C. P. Lutz, and A. J. Heinrich. “Spin coupling in engineered atomic structures”. In: *Science* 312.5776 (2006), pp. 1021–1024.

[35] C. F. Hirjibehedin, C.-Y. Lin, A. F. Otte, M. Ternes, C. P. Lutz, B. A. Jones, and A. J. Heinrich. “Large magnetic anisotropy of a single atomic spin embedded in a surface molecular network”. In: *Science* 317.5842 (2007), pp. 1199–1203.

[36] R. Toskovic, R. Van Den Berg, A. Spinelli, I. Eliens, B. Van Den Toorn, B. Bryant, J.-S. Caux, and A. Otte. “Atomic spin-chain realization of a model for quantum criticality”. In: *Nature Physics* 12.7 (2016), pp. 656–660.

[37] A. Spinelli, B. Bryant, F. Delgado, J. Fernández-Rossier, and A. F. Otte. “Imaging of spin waves in atomically designed nanomagnets”. In: *Nature materials* 13.8 (2014), pp. 782–785.

[38] S. Loth, C. P. Lutz, and A. J. Heinrich. “Spin-polarized spin excitation spectroscopy”. In: *New Journal of Physics* 12.12 (2010), p. 125021.

[39] S. Loth, S. Baumann, C. P. Lutz, D. Eigler, and A. J. Heinrich. “Bistability in atomic-scale antiferromagnets”. In: *Science* 335.6065 (2012), pp. 196–199.

[40] S. Loth, K. Von Bergmann, M. Ternes, A. F. Otte, C. P. Lutz, and A. J. Heinrich. “Controlling the state of quantum spins with electric currents”. In: *Nature Physics* 6.5 (2010), pp. 340–344.

[41] I. I. Rabi, J. R. Zacharias, S. Millman, and P. Kusch. “A new method of measuring nuclear magnetic moment”. In: *Physical review* 53.4 (1938), p. 318.

[42] E. Zavoisky. “Spin-magnetic resonance in paramagnetics”. In: *J Phys Ussr* 9 (1945), pp. 211–245.

[43] A. Abragam and B. Bleaney. *Electron paramagnetic resonance of transition ions*. Clarendon P., 1970.

[44] F. D. Natterer, F. Patthey, T. Bilgeri, P. R. Forrester, N. Weiss, and H. Brune. “Upgrade of a low-temperature scanning tunneling microscope for electron-spin resonance”. In: *Review of Scientific Instruments* 90.1 (2019).

[45] W. Paul, S. Baumann, C. P. Lutz, and A. J. Heinrich. “Generation of constant-amplitude radio-frequency sweeps at a tunnel junction for spin resonance STM”. In: *Review of Scientific Instruments* 87.7 (2016).

[46] W. M. van Weerdenburg, M. Steinbrecher, N. P. van Mullekom, J. W. Gerritsen, H. von Allwörden, F. D. Natterer, and A. A. Khajetoorians. “A scanning tunneling microscope capable of electron spin resonance and pump–probe spectroscopy at mK temperature and in vector magnetic field”. In: *Review of Scientific Instruments* 92.3 (2021).

[47] T. S. Seifert, S. Kovarik, C. Nistor, L. Persichetti, S. Stepanow, and P. Gambardella. “Single-atom electron paramagnetic resonance in a scanning tunneling microscope driven by a radio-frequency antenna at 4 K”. In: *Physical Review Research* 2.1 (2020), p. 013032.

[48] O. Peters, N. Bogdanoff, S. Acero Gonzalez, L. Melischek, J. R. Simon, G. Reecht, C. B. Winkelmann, F. von Oppen, and K. J. Franke. “Resonant Andreev reflections probed by photon-assisted tunnelling at the atomic scale”. In: *Nature Physics* 16.12 (2020), pp. 1222–1226.

[49] J. R. Gálvez, C. Wolf, F. Delgado, and N. Lorente. “Cotunneling mechanism for all-electrical electron spin resonance of single adsorbed atoms”. In: *Physical Review B* 100.3 (2019), p. 035411.

[50] A. M. Shakirov, A. N. Rubtsov, and P. Ribeiro. “Spin transfer torque induced paramagnetic resonance”. In: *Physical Review B* 99.5 (2019), p. 054434.

[51] J. Reina-Gálvez, N. Lorente, F. Delgado, and L. Arrachea. “All-electric electron spin resonance studied by means of Floquet quantum master equations”. In: *Physical Review B* 104.24 (2021), p. 245435.

[52] F. Delgado and N. Lorente. “A theoretical review on the single-impurity electron spin resonance on surfaces”. In: *Progress in Surface Science* 96.2 (2021), p. 100625.

[53] J. L. Lado, A. Ferrón, and J. Fernández-Rossier. “Exchange mechanism for electron paramagnetic resonance of individual adatoms”. In: *Physical Review B* 96.20 (2017), p. 205420.

[54] K. Yang, W. Paul, F. D. Natterer, J. L. Lado, Y. Bae, P. Willke, T. Choi, A. Ferrón, J. Fernández-Rossier, A. J. Heinrich, *et al.* “Tuning the exchange bias on a single atom from 1 mT to 10 T”. In: *Physical Review Letters* 122.22 (2019), p. 227203.

[55] P. Willke, W. Paul, F. D. Natterer, K. Yang, Y. Bae, T. Choi, J. Fernández-Rossier, A. J. Heinrich, and C. P. Lutz. “Probing quantum coherence in single-atom electron spin resonance”. In: *Science Advances* 4.2 (2018), eaaq1543.

[56] J. Kim, W.-j. Jang, T. H. Bui, D.-J. Choi, C. Wolf, F. Delgado, Y. Chen, D. Krylov, S. Lee, S. Yoon, *et al.* “Spin resonance amplitude and frequency of a single atom on a surface in a vector magnetic field”. In: *Physical Review B* 104.17 (2021), p. 174408.

[57] Y. Bae, K. Yang, P. Willke, T. Choi, A. J. Heinrich, and C. P. Lutz. “Enhanced quantum coherence in exchange coupled spins via singlet-triplet transitions”. In: *Science Advances* 4.11 (2018), eaau4159.

[58] C. Grosse, M. Etzkorn, K. Kuhnke, S. Loth, and K. Kern. “Quantitative mapping of fast voltage pulses in tunnel junctions by plasmonic luminescence”. In: *Applied Physics Letters* 103.18 (2013).

[59] S. Loth, M. Etzkorn, C. P. Lutz, D. M. Eigler, and A. J. Heinrich. “Measurement of fast electron spin relaxation times with atomic resolution”. In: *Science* 329.5999 (2010), pp. 1628–1630.

[60] W. Paul, K. Yang, S. Baumann, N. Romming, T. Choi, C. P. Lutz, and A. J. Heinrich. “Control of the millisecond spin lifetime of an electrically probed atom”. In: *Nature Physics* 13.4 (2017), pp. 403–407.

[61] M. Hänze, G. McMurtrie, S. Baumann, L. Malavolti, S. N. Coppersmith, and S. Loth. “Quantum stochastic resonance of individual Fe atoms”. In: *Science Advances* 7.33 (2021), eabg2616.

[62] T. L. Cocker, D. Peller, P. Yu, J. Repp, and R. Huber. “Tracking the ultrafast motion of a single molecule by femtosecond orbital imaging”. In: *Nature* 539.7628 (2016), pp. 263–267.

[63] M. Garg and K. Kern. “Attosecond coherent manipulation of electrons in tunneling microscopy”. In: *Science* 367.6476 (2020), pp. 411–415.

[64] F. D. Natterer. “Waveform-sequencing for scanning tunneling microscopy based pump-probe spectroscopy and pulsed-ESR”. In: *MethodsX* 6 (2019), pp. 1279–1285.

4

FREE COHERENT EVOLUTION OF A TWO ATOM SYSTEM

Our nature consists in motion;
Complete rest is death

Blaise Pascal

Full insight into the dynamics of a coupled quantum system depends on the ability to follow the effect of a local excitation in real-time. Here, we trace the free coherent evolution of a pair of coupled atomic spins by means of scanning tunneling microscopy. Rather than using microwave pulses, we use a direct-current pump-probe scheme to detect the local magnetization after a current-induced excitation performed on one of the spins. By making use of magnetic interaction with the probe tip, we are able to tune the relative precession of the spins. We show that only if their Larmor frequencies match, the two spins can entangle, causing angular momentum to be swapped back and forth. These results provide insight into the locality of electron spin scattering and set the stage for controlled migration of a quantum state through an extended spin lattice.

The results in this chapter were conceived in close collaboration with L. Farinacci, R. Rejali, R. Broekhoven, J. Gobeil, D. Coffey, M. Ternes and S. Otte. Parts of this chapter have been published in *Science* **372** (2021) [1]. Bloch-Redfield calculations shown in this chapter were performed by Prof. Dr. Markus Ternes.

4.1. INTRODUCTION

One of the long-standing goals in experimental physics is the ability to create a "quantum simulator": an engineered system of coupled quantum degrees of freedom that can be initialized in an arbitrary state, allowing one to observe its intrinsic free evolution [2]. In principle, scanning tunneling microscopy (STM) offers each of these ingredients. Individual magnetic atoms can be spatially arranged and studied by means of spin-polarized tunneling [3, 4] and electron tunneling spectroscopy [5, 6], allowing physicists to probe their local magnetization state and energy configuration, respectively. However, because of their slow time scales, these techniques have been able to observe the dynamic spin processes only indirectly [7–9].

In recent years, the STM toolbox was expanded to include pump-probe spectroscopy, which allows spin relaxation to be probed on the nanosecond timescale [10, 11], as well as electron spin resonance performed locally at the probe tip (ESR-STM) [12]. ESR-STM, combined with microwave ac pulsing schemes, enabled the observation of the coherent time evolution of a single atomic spinc[13], which is on par with achievements in semiconductor spin qubits [14, 15] and nitrogen-vacancy (NV) centers [16]. However, to demonstrate the free evolution of a pair of entangled spins, the initial excitation has to be sufficiently fast to compete with the intrinsic dynamics set by the coupling strength. ESR-STM uses a Rabi flop process for initialization, the rate of which is limited by the radio frequency (rf) power available at the probe tip.

In this work, by sequentially combining the ESR-STM and dc pump-probe techniques, we demonstrate the detection of a free, coherent flip-flop evolution of two coupled spin-1/2 atoms resulting from an electron-induced spin excitation that is nearly instantaneous when compared with the typical duration of a Rabi rotation. Using the energy resolution of ESR-STM, we tuned the eigenstates of two coupled spin-1/2 particles from Zeeman states $|\uparrow\uparrow\rangle$, $|\uparrow\downarrow\rangle$, $|\downarrow\uparrow\rangle$,and $|\downarrow\downarrow\rangle$ to singlet-triplet states $|\uparrow\uparrow\rangle$, $|-\rangle$, $|+\rangle$,and $|\downarrow\downarrow\rangle$ by varying the tip height [12, 17, 18]. Subsequently, by using a dc pump-probe scheme, we excited and read out the spin projection of one of the two spins with nanosecond resolution. This is in contrast to previous efforts, in which microwave ac pulses were used to control and read out spins [13]. Rather than by means of a Rabi rotation, in this work the coherent evolution is initiated directly through an electron spin scattering event.

As we increased the delay between pump and probe pulses, we observed an oscillating magnetization for the spin underneath the tip, which we attributed to a flip-flop interaction between the two spins [19, 20]. This implies that the excitation process that is due to tunneling electron scattering is local; it only consists of a spin flip on the atom underneath the tip, irrespective of the energy eigenstates of the system. This is a noteworthy result in the light of previous works, in which it was deemed sufficient to consider electron-induced spin excitations as transitions between energy eigenstates [21–23].

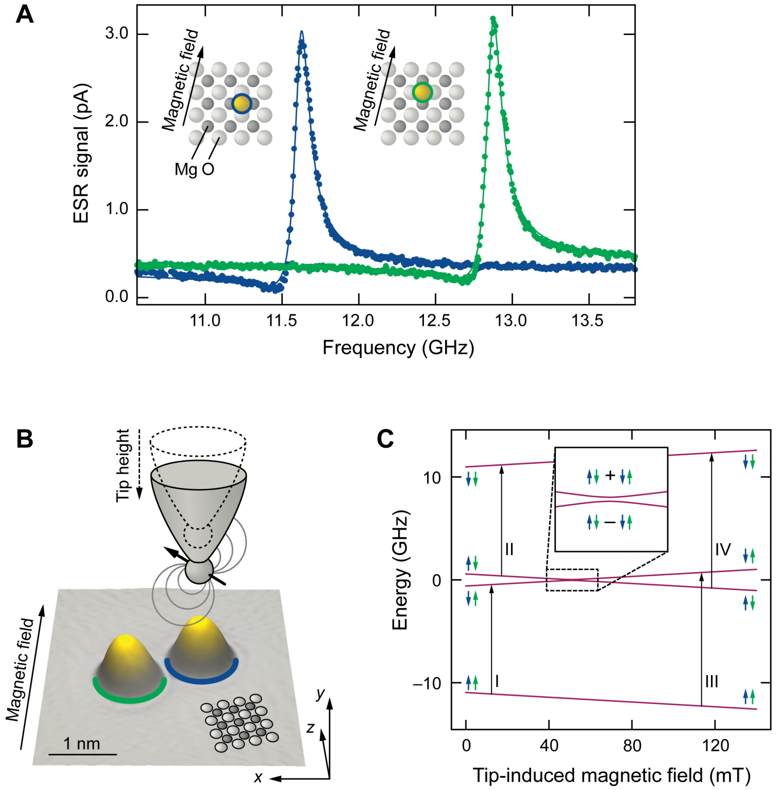

Figure 4.1: Tuning the eigenstates of a Ti dimer by using a tip-induced magnetic field. A. ESR measurements of single Ti adsorbed onto a vertical (blue) and a horizontal (green) bridge site [temperature T = 1.5 K, radiofrequency voltage V_{rf} = 30 mV, current I = 50 pA, V_{dc} = 60 mV, B_{ext} = 450 mT]. **B.** STM topography of a Ti dimer with MgO lattice indication and schematic demonstrating tuning of the tip field. **C.** Calculated energies and eigenstate compositions as function of tip field. An avoided crossing occurs at the point at which the tip field compensates the g-factor difference. Roman numerals indicate the four possible ESR transitions.

4.2. SYSTEM OF STUDY

We used a low-temperature STM to manipulate individual hydrogenated Ti atoms, henceforth referred to as Ti, on top of bilayer MgO islands on an Ag(100) crystal. To obtain spin polarization, we deposited Fe atoms and transferred them to the tip apex [24]. The ESR and pump-probe experiments were per-formed by applying the rf voltage and pulse trains to the tip, at temperatures of 1.5 K and 400 mK, respectively. We used an external magnetic field B_{ext} = 450 mT in-plane at a 14° angle with respect to the MgO lattice to separate the energy levels by means of Zeeman splitting.

We studied Ti species without any observable nuclear spin that are adsorbed on bridge sites with different orientations with respect to the external magnetic field, as sketched in fig. 4.1A. Hydrogenated Ti on MgO has been shown to be an effective spin-1/2 particle with an anisotropic g-factor [25, 26]. In agreement with these studies, we observed different ESR resonance frequencies for the two species; for the spin S_v of the vertically oriented Ti species (blue), we find a g-factor $g_\mathrm{v} = 1.75$, whereas for the spin S_h of the horizontal Ti (green), we find $g_\mathrm{h} = 1.95$ (see section 4.7.1). In fig. 5.1B and C, we demonstrate how we use the effective magnetic field that emanates from the tip on one of the two atoms to tune the level of entanglement between the spins [11, 18]. If the two spins experience the same effective Zeeman splitting, they precess at identical Larmor frequencies resulting in entangled states. Because we want to reach entanglement at a finite tip field, the two spins need to be inherently detuned in absence of the tip. For this reason, we built heterodimers out of vertically and horizontally oriented Ti species (fig. 4.1B and section 4.7.2).

4.3. TUNING THE EIGENSTATES

The dimers were engineered to have a spacing of 1.3 nm, which corresponds to a coupling strength on the order of tens of megahertz. This coupling strength was chosen to ensure that the dynamics of the local magnetization are slow enough to be probed by our experimental setup, which is limited to 5 ns pulses but still faster than the 100 ns decoherence time of Ti dimers [18]. At this distance, the atoms interact through both exchange and dipolar interactions. The Hamiltonian of the system can be written as:

$$H = (J+2D)S_\mathrm{v}^z S_\mathrm{h} S^z + (J-D)(S_\mathrm{v}^x S_\mathrm{h} S^x - S_\mathrm{v}^y S_\mathrm{h} S^y) - \mu_B B_{ext}(g_\mathrm{v} S_\mathrm{v}^z + g_\mathrm{h} S_\mathrm{h}^z) - \mu_B B_{tip} g_\mathrm{v} S_\mathrm{v}^z \quad (4.1)$$

where μ_B is the Bohr magneton and J and D are the exchange and dipolar coupling parameters, respectively. The axes are defined in fig. 4.1B. The two last terms account for the Zeeman splitting due to the external (B_{ext}) and effective tip (B_{tip}) fields, which, on the basis of their relative strengths, we assume to be aligned. In section 4.7.4, we discuss the justification and limits of this assumption.

We separated the exchange and dipolar contributions by performing the experiment on two heterodimers as sketched in fig. 4.2, A (dimer A) and B (dimer B). The two dimers are equidistant, yielding identical exchange couplings. However, because they are oriented at different angles with respect to the external field, their dipolar coupling strengths differ. This was confirmed by ESR measurements performed on top of the vertically oriented Ti of each dimer with the tip well away from the tuning point (fig. 4.2, A and B). In this situation, the $S_\mathrm{v}^x S_\mathrm{h}^x$ and $S_\mathrm{v}^y S_\mathrm{h}^y$ components of the coupling (eq. (4.1)) average out over time as the spins precess with different Larmor frequencies. The resulting coupling, being mediated through the $S_\mathrm{v}^z S_\mathrm{h}^z$ terms only, is effectively Ising-like. Because of the composition of the eigenstates and because ESR can only flip the spin underneath the tip [27], only transitions I and II were observed (fig. 4.1C). The measured splitting between these two ESR resonances corresponds to $J + 2D$ and thus is different for the two heterodimers (fig. 4.2, A and B).

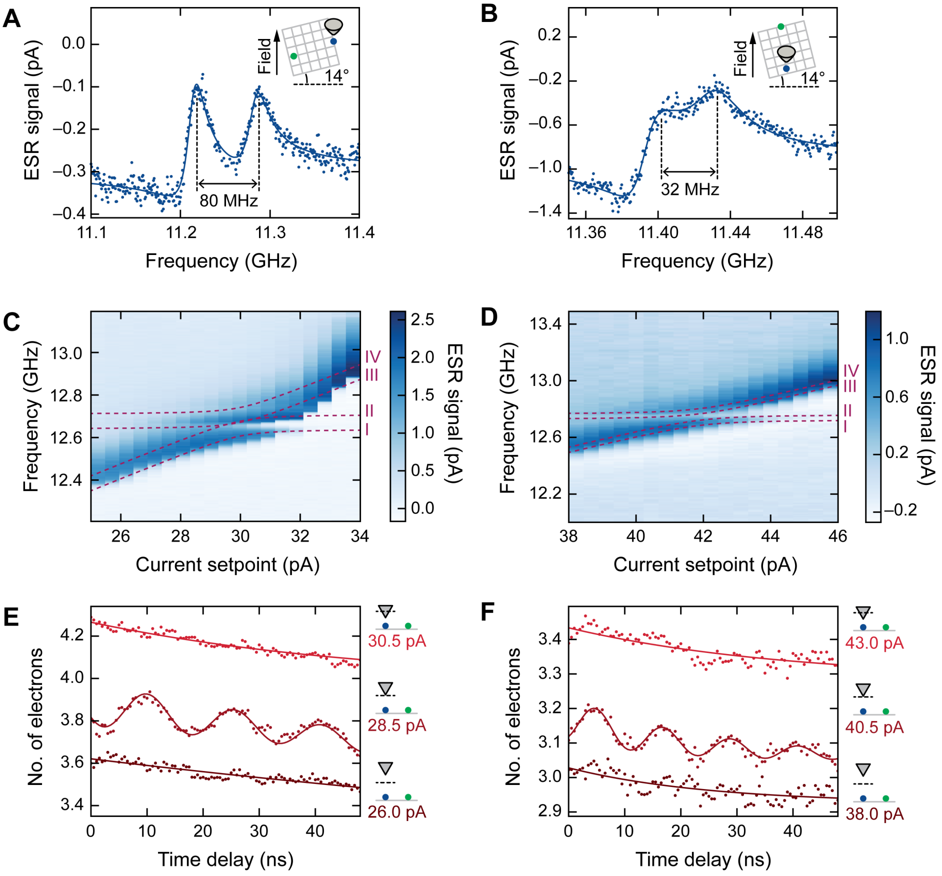

Figure 4.2: Measurement of free coherent evolution at the tuning point. A,B. ESR measurements on dimer A and dimer B ($T = 1.5$ K, $V_{\mathrm{rf}} = 50$ mV, $I = 10$ pA, $V_{\mathrm{dc}} = 60$ mV). (Insets) Schematic drawings of the dimer placement on the MgO lattice. **C,D.** ESR measurements at various tip heights, showing an avoided crossing at the tuning point ($T = 1.5$ K, $V_{\mathrm{rf}} = 50$ mV, $V_{\mathrm{dc}} = 60$ mV). Dashed lines are guides to the eye that mark ESR transitions. **E.** Pump-probe measurements on dimer A, above, below, and at the tuning point ($T = 400$ mK, setpoint voltage: 60 mV, pulse width: 7 ns). **F.** Same as **E** for dimer B (pulse width 5 ns). All pump-probe experiments use +100 mV pump and −100 mV probe pulses.

To probe the full energy-level diagram of fig. 4.1C and identify the exact tuning point for maximal entanglement, we performed ESR measurements at various tip heights for each dimer (fig. 4.2, C and D). We observed two sets of peaks that, upon tip approach, shift together and broaden because of decoherence effects [28]. These two sets of resonances can be assigned to transitions I and II and to III and IV in fig. 4.1C. Away from the tuning point, only one of these pairs was observed: transition I and II before the tuning point and transition III and IV after it. As the energy eigenstates become more entangled near the tuning point, all four transitions become accessible. Because of the opposite signs of the dipolar coupling contributions, the two dimers show slightly different behaviors: transitions II and III intersect twice for dimer A, whereas they stay apart for dimer B. We find that $J = 67 \pm 2$ MHz and $D = 2 \pm 1$ MHz for dimer A and that $D = -15 \pm 1$ MHz for dimer B (see section 4.7.3).

4.4. DYNAMICS AT THE TUNING POINT

We then arrived at the second stage of the experiment, in which we measured the free time evolution of the spins. We used a pump-probe scheme to excite and measure the spin state of the atom underneath the tip for various degrees of entanglement. When the tip height is far away from the tuning point, the pump-probe experiments show the onset of an exponential decay that is similar to the decay signal of a single excited spin (fig. 4.2, E and F, top and bottom curves) [10](9). By contrast, when tuned, we observed a clear oscillation with a frequency of 64 ± 1 MHz for dimer A and 84 ± 1 MHz for dimer B. We attribute these oscillations to the flip-flop interaction of strength $J - D$ between the two atoms in the dimer.

The dynamics of the flip-flop interaction can be well understood by describing the time evolution of the combined density matrix of the two spins within a dissipative Bloch-Redfield framework [29, 30], which accounts for the uncorrelated electron baths in sample and tip (fig. 4.3A and chapter 2). In fig. 4.3, B to E, we show the density matrices in the energy basis obtained by numerical simulation for a perfectly tuned dimer at different moments in time after the pump pulse. During the pump pulse, the system is pushed into a coherent superposition of its excited states (fig. 4.3B). These add up to a net $|{\downarrow\uparrow}\rangle$ magnetization (with the left arrow corresponding to the spin underneath the tip) as a result of spin pumping [24]. This net magnetization is reflected in the off-diagonal terms, which correspond to the coherence between the $|-\rangle$ and $|+\rangle$ states. Because of the finite thermal occupation of the excited states in the initial Boltzmann distribution, the pump pulse also populates the higher energy $|{\downarrow\downarrow}\rangle$ state. Immediately after the pulse, the off-diagonals begin to oscillate between positive and negative values (fig. 4.3, C and D), which gives rise to the observed periodicity in the magnetization (inset of fig. 4.3A). Because of the interaction with the electron baths, the oscillations decay over an effective decoherence time, and eventually, the populations evolve back toward thermal equilibrium (fig. 4.3E). We estimate the decoherence time to be 60 and 130 ns for the relaxation time (see section 4.7.5).

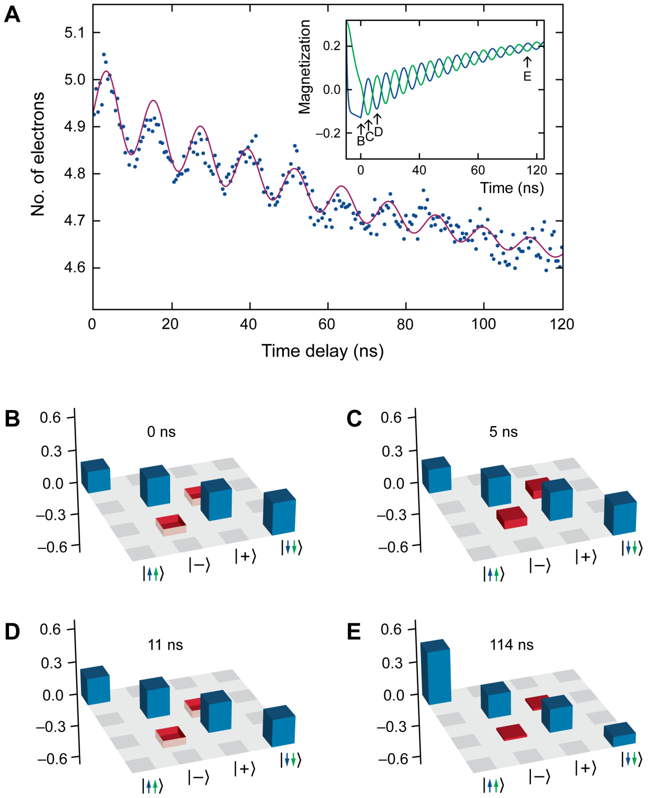

Figure 4.3: Decoherence of the flip-flop oscillation. **A.** Pump-probe measurement on dimer B showing the decay in amplitude of the oscillations ($T = 400$ mK, setpoint: 40.5 pA, 60 mV, pulse width: 7 ns). The solid line represents the calculated pump-probe signal. (Inset) Calculated magnetizations S_{v}^{z} (blue) and S_{h}^{z} (green); the origin of the time axis is set to coincide with the end of the pump pulse. **B to E.** Density matrices at different times after the pump pulse [inset of **A**]. Off-diagonal elements are marked red for clarity.

4.5. DETUNING

We then proceeded to the effect of detuning on the flip-flop oscillations. For this purpose, we performed pump-probe experiments at different current setpoints around the tuning point: 28 pA for dimer A and 40 pA for dimer B (fig. 4.4, A and B). As expected, the oscillations diminished rapidly as we tuned away from these values. Depending on the microscopic tip apex, we observed a small difference in tuning height between ESR (fig. 4.2) and pump-probe measurements (fig. 4.4). We attribute this difference to the influence of the 60 mV DC bias that is present during the ESR-STM measurements but absent for the pump-probe experiments. Recently, DC voltage component was shown to pull on Ti atoms via electrostatic force, changing the effective magnetic tip field felt by the atomic spin [31].

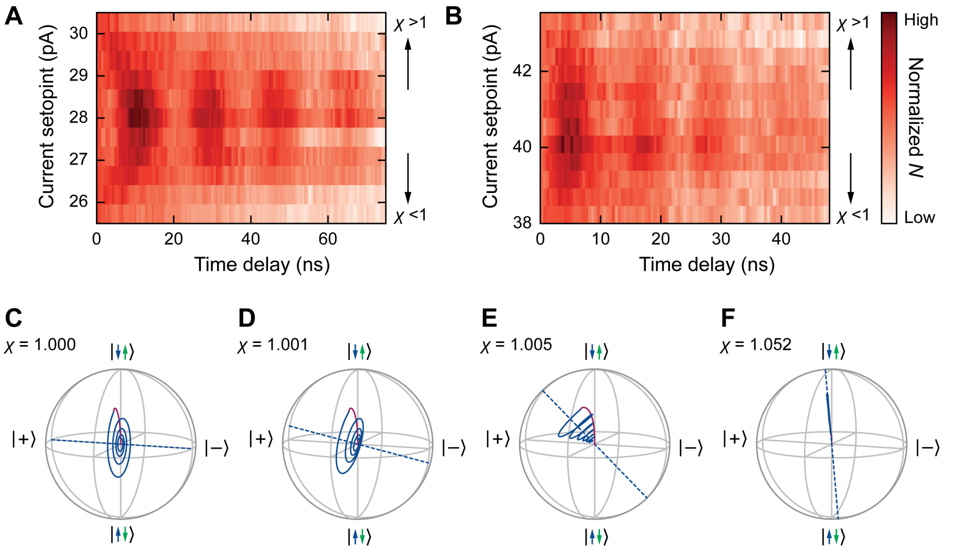

Figure 4.4: Flip-flop oscillations as function of detuning. **A,B.** Pump-probe measurements on dimers A and B at various tip heights (parameters same as those in fig. 4.2). **C to F.** Bloch sphere representations of the state evolution at increasing levels of detuning, as indicated with the detuning ratio $\chi = g_\mathrm{v}(B_\mathrm{ext} + B_\mathrm{tip})/g_\mathrm{h}B_\mathrm{ext}$. The Bloch spheres show the reduced state space between the $|\uparrow\downarrow\rangle$ and $|\downarrow\uparrow\rangle$ states. The excitation process due to the pump pulse is plotted in red, and the subsequent free evolution of the spin state is plotted in blue. For $\chi < 1$, the rotation axis (dashed blue line) tilts in the opposite direction.

To gain insight into the effect of detuning on the spin dynamics, we mapped the effective two-level system of the inner 2 by 2 matrix of the density matrix onto a Bloch sphere. For clarity, the axes of the sphere were fixed to be the energy eigenstates of the fully tuned case, and the projected spin state evolution is plotted for different levels of detuning (fig. 4.4, C to F). As can be seen from the density matrices in fig. 4.3, the spin state always has components outside the inner 2 by 2 matrix, meaning that the projection in fig. 4.4 never reaches the surface of the sphere.

When the dimer is in tune (fig. 4.4C), the state moves fully within the vertical plane of the Bloch sphere, making maximal flip-flops between $|\uparrow\downarrow\rangle$ and $|\downarrow\uparrow\rangle$. With increasing detuning, the axis that the state rotates around moves as the eigenstates of the system gradually tilts toward the vertical. The difference between the projected maxima and minima of the oscillation onto the vertical axis gets smaller, and thus, the oscillation amplitude decreases, which is consistent with our experimental observations.

The observed flip-flop frequency remains constant as a function of detuning. This seems surprising, as the energy splitting is supposed to increase away from the tuning point, causing an increase in the frequency. We attribute this discrepancy to the fact that the avoided crossing between the $|-\rangle$ and $|+\rangle$ states forms a clock transition [18]. Magnetic noise originating from mechanical vibrations of the STM tip effectively flattens out the parabolic shape of the avoided crossing leading to a single dominant frequency in the pump-probe measurements.

4.6. CONCLUSIONS

By combining the energy resolution of ESR-STM and the time resolution of dc pump-probe spectroscopy, we have demonstrated an experimental procedure that enables the observation of the free coherent evolution of coupled atomic spins. Because the dynamic processes are initialized by means of a coherence-preserving pulse in the tunneling current, our method provides insight into the physics of electron spin scattering that could not be obtained by pulsed ESR-STM methods [13]. Specifically, only the spin directly underneath the tip is affected by the spin excitation, irrespective of the global quantum state. In con-junction with the recent demonstration of pulsed ESR-STM, our technique offers path-ways toward coherent manipulation of extended atomic spin arrays. The ability to perform a very local, nearly instantaneous, coherent spin flip inside an extended spin lattice constitutes an essential building block for advances in spintronic engineering as well as studies into the propagation of spin waves.

4.7. APPENDIX

4.7.1. DETERMINATION OF G-FACTORS

We can determine the different g-factors of the horizontal and vertical bridge adsorption sites of Ti atoms by recording ESR spectra as a function of set-point current [18]. For both the horizontal bridge site $\mathrm{Ti_h}$ (fig. 4.5A) and the vertical bridge site $\mathrm{Ti_v}$ (fig. 4.5B), the resonance shifts to higher frequencies upon tip approach indicating that the effective tip magnetic field is (at least partially) aligned with the external magnetic field. We extract the resonance positions by fitting each spectrum with a Fano function (red curves in fig. 4.5A and B) and plot their evolution as a function of setpoint current in fig. 4.5C. We observe a linear shift of the resonance positions indicating that we are in a regime where the exchange interaction between tip and Ti atom dominates over the dipolar one [32]. We can thus express the position of the resonance frequency in ESR as a function of setpoint current I as was done in [18]:

$$f = \frac{g\mu_B}{2\pi\hbar}(B_{\mathrm{tip}} + B_{\mathrm{ext}}) = E + aI \qquad (4.2)$$

where E and a are parameters that we obtain by fitting a line to the data points in fig. 4.5C.

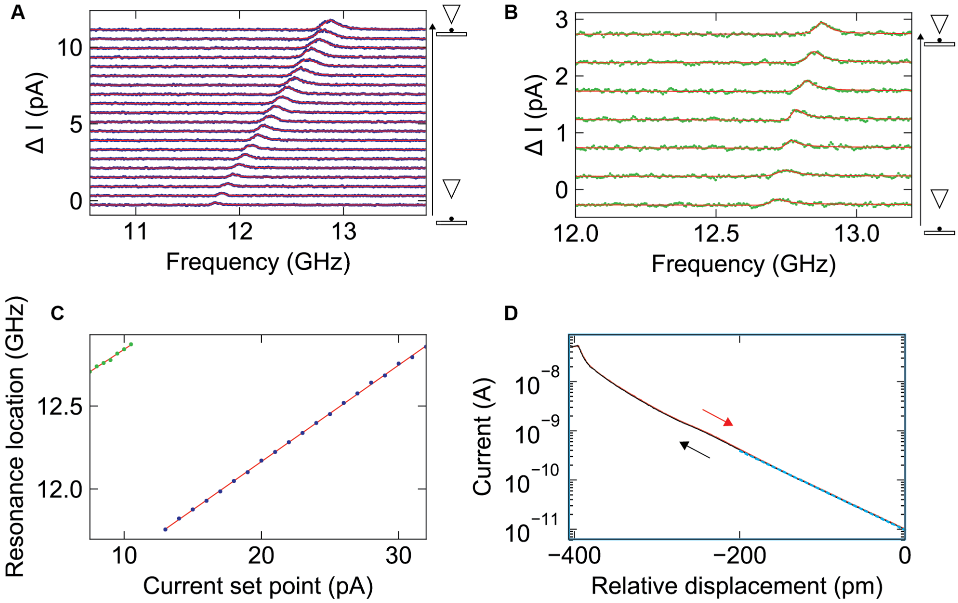

Figure 4.5: Extraction of the g-factor. A. ESR spectra taken on a single $\mathrm{Ti_v}$ at a range of setpoints: 60 mV, 13–32 pA. Red lines are Fano fits to determine the resonance location. **B.** ESR spectra on a single $\mathrm{Ti_h}$ (60 mV, 7.5-10.5 pA). **C.** ESR resonances as function of setpoint for $\mathrm{Ti_v}$ (blue) and $\mathrm{Ti_h}$ (green). Red lines are linear fits. **D.** Current measurement as function of tip height on top of a single bridge-site Ti (setpoint: 60 mV, 10 pA). Blue dotted line is a linear fit.

The parameters of the fits are shown in table 4.1 where the error bars correspond to the standard deviations of the fits (red lines). The g-factors are deduced from E and we obtain for the vertical Ti: $g_\mathrm{v} = 1.740 \pm 0.006$ (corresponding to an effective magnetic moment $\mu_\mathrm{v} = 0.87 \pm 0.003\mu_\mathrm{B}$) and for the horizontal species: $g_\mathrm{h} = 1.953 \pm 0.003$ ($\mu_\mathrm{h} = 0.98 \pm 0.002\mu_\mathrm{B}$).

Knowing the g-factors we can relate the changes in current setpoint to effective tip field variations: a variation of the current by 1 pA leads to a change in magnetic field of ~ 2.2 mT for $\mathrm{Ti_h}$ and ~ 2.1 mT for $\mathrm{Ti_v}$, indicating a small tilt of the tip field with respect to the MgO lattice. Finally, in fig. 4.5D, we can relate the current variations to changes in tip height after opening the feedback with $V_\mathrm{bias} = 60$ mV and $I = 10$ pA (a negative offset corresponds to a tip approach toward the atom). The forward and backward traces fall on top of each other ensuring the stability and repeatability of the experiment, with contact reached at ~ −390 pm. A fit of the exponential dependence of the current with distance for the low conductance regime (blue dashed curve in fig. 4.5D) gives $I \propto e^{-d/d_0}$, where $d_0 = 54.05 \pm 0.05$ pm.

Atom	E [GHz]	a [MHz/pA]
$\mathrm{Ti_v}$	11.002 ± 0.005	58.15 ± 0.22
$\mathrm{Ti_h}$	12.302 ± 0.019	54.03 ± 2.21

Table 4.1: Fit parameters for g-factor extraction. Fit parameters from the linear fit function (eq. (4.2)) to extract the g-factor of $\mathrm{Ti_h}$ and $\mathrm{Ti_v}$.

4.7.2. DIMER CONFIGURATION

We construct heterodimers of Ti atoms adsorbed on bridge sites at different angles with the external magnetic field. The exact position of the atoms with respect to the underlying MgO lattice is determined by obtaining atomic resolution of a MgO island (see fig. 4.6A). In this image only one of the two sub-lattice (Mg or O) of the MgO layer is visible: the lattice parameter is ~ 2.87 Å(i.e. $A_{\mathrm{Ag}}/\sqrt{2}$, where A_{Ag} is the lattice constant of Ag(100)) [17]. The adsorption sites of the atoms refer to their position with respect to the O-lines of the MgO lattice, which we draw in red in fig. 4.6. Once the relative orientation of the MgO lattice is determined, we identify the atomic positions by anchoring the lattice at Fe atoms (marked in orange in fig. 4.6B and C), which adsorb on O-sites [12, 33]. As one can see in fig. 4.6B and C, the two dimers presented in the main text have the exact same spacing but with a 102° angle between them. The horizontal and vertical nature of the bridge adsorption sites for the Ti atoms can be furthermore confirmed by ESR measurements (see main text).

4.7.3. DETERMINATION OF COUPLING PARAMETERS

We detail in this section how we estimate the values of the exchange coupling parameter J, and dipolar coupling parameter D for the two dimers presented in the main text. As mentioned in section 4.7.2, the two dimers have the exact same spacing, leading to identical exchange coupling strength but different orientations with respect to the external field so that their dipolar couplings differ. In particular, as one can see from fig. 4.7A, we expect $D_{\mathrm{A}} > 0$ since the dipolar coupling favors antiferromagnetism for dimer A and $D_{\mathrm{B}} < 0$ corresponding to a favored ferromagnetic dipolar coupling for dimer B (fig. 4.7B). The dependence of the energy levels on the J and D parameters is given by the Hamiltonian (eq. (4.1)). In ESR we measure transitions between these energy levels and we define:

$$\begin{aligned} f_I &= \frac{1}{2\pi\hbar}(E_1 - E_0) \\ f_{II} &= \frac{1}{2\pi\hbar}(E_3 - E_2) \\ f_{III} &= \frac{1}{2\pi\hbar}(E_2 - E_0) \\ f_{IV} &= \frac{1}{2\pi\hbar}(E_3 - E_1) \end{aligned} \tag{4.3}$$

In particular we obtain that the frequency difference between the first and second resonances and the third and fourth resonances does not depend on the tip field:

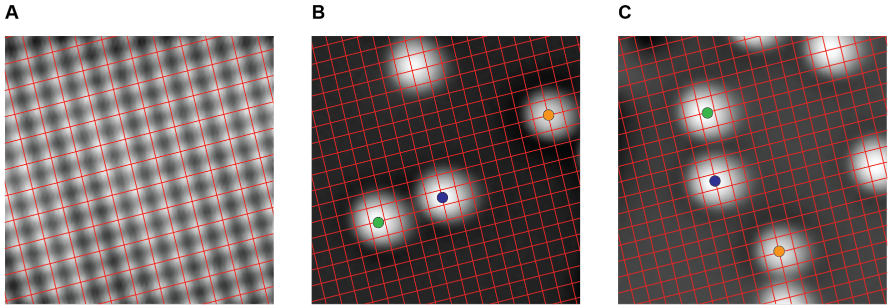

Figure 4.6: Dimer placement. A. Atomic resolution topography of the MgO lattice (3 nm × 3 nm, setpoint: 5 mV, 8 nA). **B.** Dimer A with MgO lattice overlaid (5 nm × 5 nm, setpoint: 150 mV, 10 pA). Orange dot shows an Fe atom adsorbed on an O-site. **C.** Dimer B with MgO lattice overlaid (5 nm × 5 nm, setpoint: 150 mV, 10 pA). Orange dot shows an Fe atom adsorbed on an O-site.

$$\begin{aligned}\Delta f = f_{IV} - f_{III} = f_{II} - f_I \\ &= \frac{1}{2\pi\hbar}(E_3 - E_2 - E_1 + E_0) \\ &= J + 2D\end{aligned} \tag{4.4}$$

We determine this frequency splitting by recording a high resolution ESR spectrum with the tip far away to reduce decoherence effects and subsequent broadening of the peaks. By fitting the spectra by the sum of two Fano functions (see fig. 4.2A of the main text) we obtain:

$$\begin{aligned}J + 2D_\mathrm{A} &= 68.71 \pm 0.25\mathrm{MHz} \\ J + 2D_\mathrm{B} &= 37.48 \pm 0.64\mathrm{MHz}\end{aligned} \tag{4.5}$$

where the error bars correspond the standard deviations of the fits. The flip-flop transition observed in the pump-probe measurements directly correlates to the energy splitting between the first and second eigenstates:

$$f_\text{flip-flop} = \frac{1}{2\pi\hbar}\sqrt{[(g_\mathrm{v} - g_\mathrm{v})\mu_B B_\mathrm{ext} + g_\mathrm{v})\mu_B B_\mathrm{tip}]^2 + [J - D]^2} \tag{4.6}$$

The oscillations are observed when the two spins are tuned so that the first term in the square root equals zero. Fitting the curves of fig. 4.2E and F of the main text by a damped sinusoid (see section 4.7.5) gives:

$$\begin{aligned}|J + 2D_\mathrm{A}| &= 64.26 \pm 0.35\mathrm{MHz} \\ |J + 2D_\mathrm{B}| &= 83.1 \pm 0.81\mathrm{MHz}\end{aligned} \tag{4.7}$$

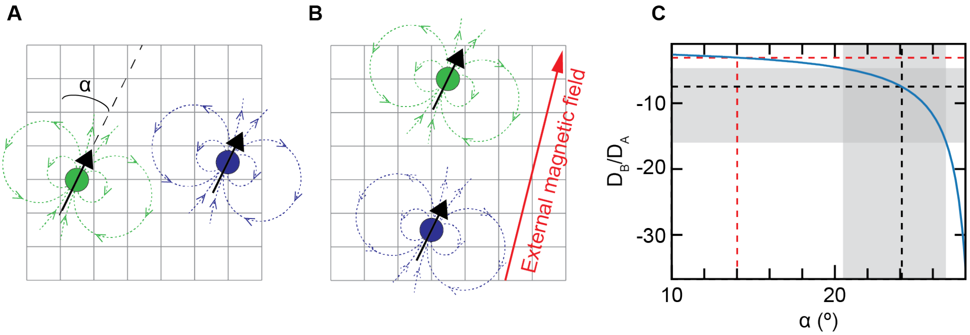

Figure 4.7: Dipolar interaction. A and **B.** Sketches of Dimers A (B) drawn on a MgO lattice grid with the dipolar field emanating from each spin. The angle α indicates the angle between the lattice and the ground-state orientation of the spins, which here, in contrast to the main text, is not fixed in the direction the external field (red arrow). **C.** Ratio of the dipolar coupling strengths of both dimers as function of α. Black dashed lines show the ratio we find from our experiments, red dashed lines show the ratio at a 14° angle as we expect from our setup. Grey colored area shows estimated error margin.

where the error bars are the standard deviations of the fits. From equations (eq. (4.5)) and (eq. (4.7)), we obtain the following estimates:

$$\begin{aligned} J &= 67 \pm 2\text{MHz} \\ D_{\text{A}} &= 2 \pm 1\text{MHz} \\ D_{\text{B}} &= -15 \pm 1\text{MHz} \end{aligned} \tag{4.8}$$

In the model used in the main text, we assume the ground-state orientations of the spins to be aligned with B_{ext}. The obtained values for the dipolar coupling parameters allow us to estimate to what extent this assumption is correct. The dipolar coupling parameter can be expressed as a function of the angle θ between the ground-state orientations of the spins and the vector $\vec{r}$ between the two atoms: $D = D_0(1-3\cos^2(\theta))/2\pi r^3$ where D_0 is a constant that does not depend on the geometry of the dimer. Since we know the relative orientation of the dimers with respect to each other we can calculate the ratio D_B/D_A as a function of the angle α that the spins in the ground state make with the lattice vector of MgO (see fig. 4.7A). The results are plotted in fig. 4.7C where the black dashed lines corresponds to the value obtained from the experiment (the grey area representing the error bars) and the red dashed lines show the result obtained when the spins in the ground state are fully aligned with the external magnetic field ($\alpha = 14°$). The small deviation indicates a non-perfect ground-state alignment of the spins with respect to external field. This is expected for an anisotropic g-factor (in this case, the deviation differs for the two species) and can also be influenced by the presence of the spin-polarized tip.

We can ensure that the values obtained for J, D_A and D_B correctly reproduce the behavior of the ESR measurements around the tuning point as shown in fig. 4.2C and D of the main text. We calculate the dependence of the ESR resonances as a function of tip field using equations (eq. (4.2)) and then use the analysis performed in section 4.7.1 to convert the tip field to an effective tunneling current. We find a good agreement with the measurements if we include a current and frequency offset to the calculations: the guide to the eye of fig. 4.2C (fig. 4.2D) is obtained using the J, D_A and D_B values of eq. (4.8), a current offset of 7.6 pA (19.5 pA) and a frequency offset of 0.38 GHz (0.45 GHz). The qualitative behavior of the ESR peaks at the tuning point can also be understood by considering the frequency difference between the second and third ESR resonances. Using equations (eq. (4.3)) we have:

$$\begin{aligned} f_{III} - f_{II} &= \frac{1}{2\pi\hbar}(2E_2 - E_0 - E_3) \\ &= -J - 2D\sqrt{[(\gamma_1 - \gamma_2)\hbar B_{\text{ext}} + \gamma_1 \hbar B_{\text{tip}}]^2 + [J - D]^2} \end{aligned} \tag{4.9}$$

since $J > D$, we have at the tuning point:

$$f_{III} - f_{II} = -3D \tag{4.10}$$

As a result, when $D > 0$, we have $f_{III} > f_{II}$ at the tuning point and the resonances cross twice upon tip approach, as is the case for dimer A. By contrast, when $D < 0$, the two resonances stay apart from each other as observed for dimer B.

The guides to the eye shown in fig. 4.2C and D of the main text were produced by calculating the resonances shown in equations (eq. (4.3)) as function of tip field. In order to match the calculation with the experiment, we found that we needed constant offsets in both energy and setpoint axes depending on the microscopic apex of the tip used for measurements.

A better quantitative agreement may be achieved by making the model of eq. (4.1) more realistic. First, we note that we neglected the x and y components of the tip field while these must be present for driving the ESR resonant transitions [33]. Second, the tip field is assumed to not affect the Ti_h atom of the dimer (see section 4.7.4). Third, we did not separately treat the spin and orbital degrees of freedom and considered the effective anisotropy of the g-factor along the external field rather than along the crystal lattice. Fourth, we assumed that the ground state orientations of the spins are oriented along the direction of the external field. Finally, we use the secular approximation in which the orientations of the dipolar fields are fixed in space.

4.7.4. TIP DEPENDENCE

In our model Hamiltonian (eq. (4.1)) we assume the tip field, as well as the surface spins in the groundstate, to be aligned with the external field in order to simplify the dipolar interaction term. However, current understanding of the ESR-STM principle demands a small angle between the tip field and the external field [30]. Therefore, we performed additional Bloch-Redfield simulations with varied angles between the external and tip-induced fields to study the impact of this on the spins in the surface. As shown in fig. 4.8A, changing the angle shifts the tuning point to higher magnetic field values but does not affect the energy splitting at the tuning point. Therefore, the resulting flip-flop evolution is affected only in its amplitude, as calculated in fig. 4.8B.

The ESR and pump probe data presented in the main text on dimers A and B were taken with two different microtips. Figure 4.8C-E show a dataset taken on dimer A with the same microtip as used on dimer B in the main text. Although we find the same qualitative behaviour in the experiments independent of the microtip, we see a number of small quantitative differences.

First, the current setpoint at which the crossing is observed shifts from approximately 30 pA to 34 pA. This can be accounted for by the differences in angle and magnitude of the tip field for various tips, as discussed above. Second, the frequency at which the crossing occurs changes from approximately. 12.6 GHz to 12.3 GHz, which is not captured fully by our current model Hamiltonian. A possible explanation, however, could be that the field emanating from the tip also affects the second spin with a magnitude in the order of 10 mT. Third, the flip-flop oscillation frequency at the tuning point is slightly lower: approximately 60 MHz instead of 64 MHz. From our model, we expect this frequency to be determined by $J-D$, and thus independent of the microtip. We suspect that a more intricate interaction with the tip can cause the spin under the tip to tilt, therefore slightly changing the values of D. This behaviour might be captured by removing the secular approximation from our model, or by modelling the tip spin as a quantum spin instead of a classical nanomagnet.

We extract the values and errors associated with J and D (eq. (4.8)) by using our model Hamiltonian (eq. (4.1)) to analyse the experimental results. As previously stated, we expect that small variations in J and D may be observed for different microtips. These statistical variations may exceed the quoted error determined for specific microtips. However, they do not alter the essence of the observed flip-flop physics.

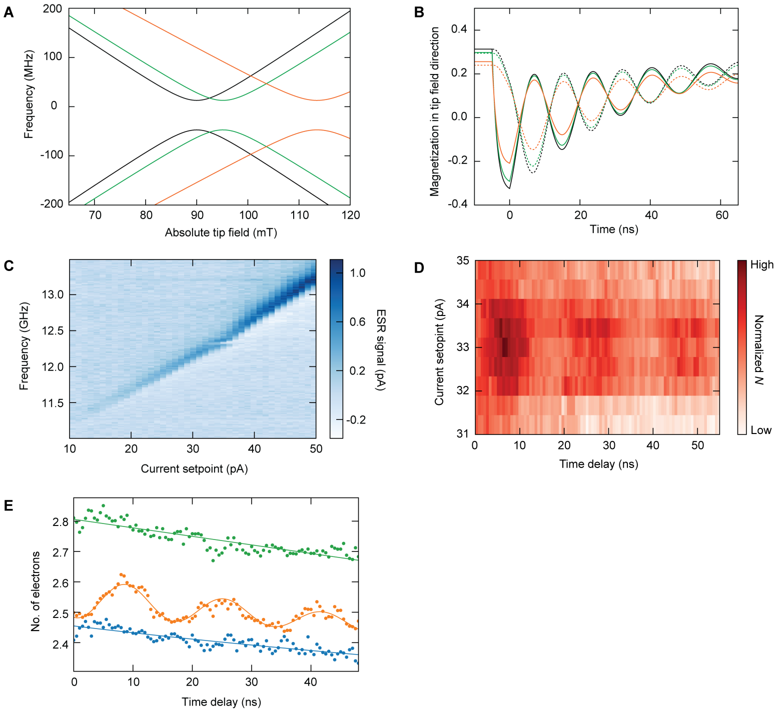

Figure 4.8: Tip dependence. A. Calculated energy levels for tip field misalignment with respect to the external field by 0° (black), 20° (green) and 40° (orange). **B.** Calculated magnetization of spin 1 (underneath tip, solid line) and spin 2 (dotted line) as function of time. Color scheme same as in **B**. **C.** ESR measurements taken on dimer A with same microtip as used on dimer B in the main text. **D,E.** Pump probe measurements taken on dimer A with the same microtip as used on dimer B in the main text. Pulse width: 5 ns. Setpoints in **E**: 31 pA (blue), 33 pA (orange) and 35 pA (green). All other experimental settings identical to fig. 4.2 of the main text.

4.7.5. Lifetime measurements

In order to obtain an estimate for the effective spin relaxation time T_1 for the dimers near the tuning point, we perform pump-probe measurements with 50 ns wide pulses (fig. 4.9B). We find an exponential decay when the tip is above the $\mathrm{Ti_h}$ (blue) while there is a deviation form exponential behavior for the $\mathrm{Ti_v}$ atom (orange) when the tip is at the tuning height. With the tip above the $\mathrm{Ti_h}$, the dimer is detuned and the excitation caused by the pump pulse remains on the atom under the tip. When the tip is above the $\mathrm{Ti_v}$ however, the dimer is in tune and the excitation is shared between the two atoms. This causes a drop in magnetization measured by the pump pulse up until the point where the spin state is decohered and the tuned and detuned cases become indistinguishable. As a measure for the relaxation time of the spin excitation on the dimer, we fit the exponential decay at the tuning point (feedback opened at 28 pA, 60 mV) on the $\mathrm{Ti_h}$. We find: $T_1 = 130 \pm 5$ ns.

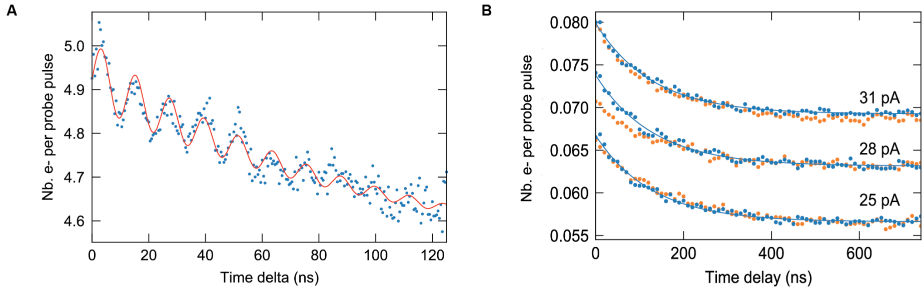

Figure 4.9: Lifetime measurements on dimer A. A. Same data as plotted in fig. 4.3A of the main text, herewith a damped sinusoidal fit to determine the decoherence time. **B.** Pump-probe data on Ti$_h$ (blue) and Ti$_V$ (orange) of Dimer A (setpoint voltage: 60 mV, pulse width: 50 ns, pump pulse height: +100 mV, probe pulse height: -100 mV).

The decoherence time T_2 is determined by fitting a damped sinusoid to the data shown in Fig 3A in the main text.

$$Ae^{-t/T_2}\sin 2\pi f t + Be^{-t/T_1} + C, \tag{4.11}$$

where f is the frequency of the oscillations, T_1 and T_2 characteristic decay times, C an offset, and A and B scaling coefficients for the oscillations and exponential decay, respectively. We find $T_2 = 59 \pm 9$ ns and $T_1 = 101 \pm 13$ ns, where the error bars are the standard deviations of the fits (fig. 4.9A). The smaller T_1 could be assigned to the fact that when the dimer is in tune, the excitation is shared between the two atoms and therefore two scattering centers that connect the excitation to the electron bath. We note that the data was recorded only over the onset of the exponential decay (the first 125 ns) and that the definition of T_1 as in equation eq. (4.11) is simplistic since when the dimer is in tune the system is more complex than an effective two level system. We therefore give the upper limit as determined in fig. 4.9B for our estimate in the main text.

REFERENCES

[1] **L. M. Veldman**, L. Farinacci, R. Rejali, R. Broekhoven, J. Gobeil, D. Coffey, M. Ternes, and A. F. Otte. “Free coherent evolution of a coupled atomic spin system initialized by electron scattering”. In: *Science* 372.6545 (2021), pp. 964–968.

[2] J. I. Cirac and P. Zoller. “Goals and opportunities in quantum simulation”. In: *Nature physics* 8.4 (2012), pp. 264–266.

[3] S. Heinze, M. Bode, A. Kubetzka, O. Pietzsch, X. Nie, S. Blugel, and R. Wiesendanger. “Real-space imaging of two-dimensional antiferromagnetism on the atomic scale”. In: *Science* 288.5472 (2000), pp. 1805–1808.

[4] F. Meier, L. Zhou, J. Wiebe, and R. Wiesendanger. “Revealing magnetic interactions from single-atom magnetization curves”. In: *Science* 320.5872 (2008), pp. 82–86.

[5] A. J. Heinrich, J. A. Gupta, C. P. Lutz, and D. M. Eigler. “Single-atom spin-flip spectroscopy”. In: *Science* 306.5695 (2004), pp. 466–469.

[6] C. F. Hirjibehedin, C. P. Lutz, and A. J. Heinrich. “Spin coupling in engineered atomic structures”. In: *Science* 312.5776 (2006), pp. 1021–1024.

[7] M. Ternes. “Spin excitations and correlations in scanning tunneling spectroscopy”. In: *New Journal of Physics* 17.6 (2015), p. 063016.

[8] R. Elbertse, D. Coffey, J. Gobeil, and A. Otte. “Remote detection and recording of atomic-scale spin dynamics”. In: *Communications Physics* 3.1 (2020), p. 94.

[9] L. Malavolti, G. McMurtrie, S. Rolf-Pissarczyk, S. Yan, J. A. Burgess, and S. Loth. “Minimally invasive spin sensing with scanning tunneling microscopy”. In: *Nanoscale* 12.21 (2020), pp. 11619–11626.

[10] S. Loth, M. Etzkorn, C. P. Lutz, D. M. Eigler, and A. J. Heinrich. “Measurement of fast electron spin relaxation times with atomic resolution”. In: *Science* 329.5999 (2010), pp. 1628–1630.

[11] S. Yan, D.-J. Choi, J. A. Burgess, S. Rolf-Pissarczyk, and S. Loth. “Control of quantum magnets by atomic exchange bias”. In: *Nature nanotechnology* 10.1 (2015), pp. 40–45.

[12] S. Baumann, W. Paul, T. Choi, C. P. Lutz, A. Ardavan, and A. J. Heinrich. “Electron paramagnetic resonance of individual atoms on a surface”. In: *Science* 350.6259 (2015), pp. 417–420.

[13] K. Yang, W. Paul, S.-H. Phark, P. Willke, Y. Bae, T. Choi, T. Esat, A. Ardavan, A. J. Heinrich, and C. P. Lutz. “Coherent spin manipulation of individual atoms on a surface”. In: *Science* 366.6464 (2019), pp. 509–512.

[14] J. J. Pla, K. Y. Tan, J. P. Dehollain, W. H. Lim, J. J. Morton, D. N. Jamieson, A. S. Dzurak, and A. Morello. “A single-atom electron spin qubit in silicon”. In: *Nature* 489.7417 (2012), pp. 541–545.

[15] E. Kawakami, P. Scarlino, D. R. Ward, F. Braakman, D. Savage, M. Lagally, M. Friesen, S. N. Coppersmith, M. A. Eriksson, and L. Vandersypen. “Electrical control of a long-lived spin qubit in a Si/SiGe quantum dot”. In: *Nature nanotechnology* 9.9 (2014), pp. 666–670.

[16] R. Hanson, V. Dobrovitski, A. Feiguin, O. Gywat, and D. Awschalom. “Coherent dynamics of a single spin interacting with an adjustable spin bath”. In: *Science* 320.5874 (2008), pp. 352–355.

[17] K. Yang, Y. Bae, W. Paul, F. D. Natterer, P. Willke, J. L. Lado, A. Ferrón, T. Choi, J. Fernández-Rossier, A. J. Heinrich, *et al.* “Engineering the eigenstates of coupled spin-1/2 atoms on a surface”. In: *Physical Review Letters* 119.22 (2017), p. 227206.

[18] Y. Bae, K. Yang, P. Willke, T. Choi, A. J. Heinrich, and C. P. Lutz. “Enhanced quantum coherence in exchange coupled spins via singlet-triplet transitions”. In: *Science Advances* 4.11 (2018), eaau4159.

[19] J. R. Petta, A. C. Johnson, J. M. Taylor, E. A. Laird, A. Yacoby, M. D. Lukin, C. M. Marcus, M. P. Hanson, and A. C. Gossard. “Coherent manipulation of coupled electron spins in semiconductor quantum dots”. In: *Science* 309.5744 (2005), pp. 2180–2184.

[20] Y. He, S. Gorman, D. Keith, L. Kranz, J. Keizer, and M. Simmons. “A two-qubit gate between phosphorus donor electrons in silicon”. In: *Nature* 571.7765 (2019), pp. 371–375.

[21] C. F. Hirjibehedin, C.-Y. Lin, A. F. Otte, M. Ternes, C. P. Lutz, B. A. Jones, and A. J. Heinrich. “Large magnetic anisotropy of a single atomic spin embedded in a surface molecular network”. In: *Science* 317.5842 (2007), pp. 1199–1203.

[22] A. Otte, M. Ternes, S. Loth, C. Lutz, C. Hirjibehedin, and A. Heinrich. “Spin excitations of a Kondo-screened atom coupled to a second magnetic atom”. In: *Physical review letters* 103.10 (2009), p. 107203.

[23] A. Spinelli, B. Bryant, F. Delgado, J. Fernández-Rossier, and A. F. Otte. “Imaging of spin waves in atomically designed nanomagnets”. In: *Nature materials* 13.8 (2014), pp. 782–785.

[24] S. Loth, K. Von Bergmann, M. Ternes, A. F. Otte, C. P. Lutz, and A. J. Heinrich. “Controlling the state of quantum spins with electric currents”. In: *Nature Physics* 6.5 (2010), pp. 340–344.

[25] M. Steinbrecher, W. M. Van Weerdenburg, E. F. Walraven, N. P. Van Mullekom, J. W. Gerritsen, F. D. Natterer, D. I. Badrtdinov, A. N. Rudenko, V. V. Mazurenko, M. I. Katsnelson, *et al.* “Quantifying the interplay between fine structure and geometry of an individual molecule on a surface”. In: *Physical Review B* 103.15 (2021), p. 155405.

[26] P. Willke, Y. Bae, K. Yang, J. L. Lado, A. Ferrón, T. Choi, A. Ardavan, J. Fernández-Rossier, A. J. Heinrich, and C. P. Lutz. “Hyperfine interaction of individual atoms on a surface”. In: *Science* 362.6412 (2018), pp. 336–339.

[27] T. Choi, W. Paul, S. Rolf-Pissarczyk, A. J. Macdonald, F. D. Natterer, K. Yang, P. Willke, C. P. Lutz, and A. J. Heinrich. “Atomic-scale sensing of the magnetic dipolar field from single atoms”. In: *Nature nanotechnology* 12.5 (2017), pp. 420–424.

[28] P. Willke, W. Paul, F. D. Natterer, K. Yang, Y. Bae, T. Choi, J. Fernández-Rossier, A. J. Heinrich, and C. P. Lutz. “Probing quantum coherence in single-atom electron spin resonance”. In: *Science Advances* 4.2 (2018), eaaq1543.

[29] C. Cohen-Tannoudji, J. Dupont-Roc, and G. Grynberg. *Atom-photon interactions: basic processes and applications.* John Wiley & Sons, 1998.

[30] F. Delgado and J. Fernández-Rossier. “Spin decoherence of magnetic atoms on surfaces”. In: *Progress in Surface Science* 92.1 (2017), pp. 40–82.

[31] P. Kot, M. Ismail, R. Drost, J. Siebrecht, H. Huang, and C. R. Ast. “Electric Control of Spin Transitions at the Atomic Scale”. In: *arXiv preprint arXiv:2209.10969* (2022).

[32] P. Willke, K. Yang, Y. Bae, A. J. Heinrich, and C. P. Lutz. “Magnetic resonance imaging of single atoms on a surface”. In: *Nature Physics* 15.10 (2019), pp. 1005–1010.

[33] T. S. Seifert, S. Kovarik, D. M. Juraschek, N. A. Spaldin, P. Gambardella, and S. Stepanow. “Longitudinal and transverse electron paramagnetic resonance in a scanning tunneling microscope”. In: *Science Advances* 6.40 (2020), eabc5511.

5

COHERENT SINGLE MAGNON DYNAMICS AT THE ATOMIC SCALE

One's company,
two's a crowd
and three's a party

Andy Warhol

In the previous chapter, we showed a proof-of-concept measurement of a single spin excitation, that was induced by scattering electrons during a DC bias pulse, being swapped back and forth between two single atoms. In this chapter we will use the same techniques to study how a single spin excitation, also called a magnon, becomes delocalized and travels through more extended atomic structures. We start by building chains of Ti atoms with different lengths. Subsequently, we insert a single magnon by flipping the spin of a weakly coupled readout atom close to the structure. For a chain of length N*, we find* N *different tuning points when sweeping the STM tip height, each corresponding to a magnetic eigenmode of the chain. By building a branched structure, we are able to give the magnon some degree of direction: it either resonates with one of the two arms or delocalizes over the entire structure depending on the amount of locally applied field by the STM tip. Not only do these results give insight into the migration dynamics of a single magnon, they also open the door to building and studying low dimensional spintronics devices on the atomic scale.*

The results in this chapter were conceived in close collaboration with L. Farinacci and S. Otte. Parts of this chapter are in preparation for peer reviewed publication [1].

5.1. INTRODUCTION

The study of traveling magnetic excitations in the form of spin waves is of great importance to the understanding of novel materials [2], quantum sensing applications [3] and the development of spintronics devices [4]. Most experimental research on spin wave propagation is done either in bulk samples or in nanoscale devices where, in spite of their relatively small size, the magnetic excitation is delocalized over many lattice sites [5]. These methods are powerful tools for studying collective behaviour emerging from interactions between many spins. However, here we aim to give fundamental insight into this spin transport by studying atomic chains and unravel the impact of the quantum nature of the spins on their dynamical properties.

To achieve this goal, we use the atomic scale spatial resolution and control that scanning tunneling microscopy (STM) offers. Additionally, STM provides a powerful bottom-up platform due to it's ability to craft nanomagnets atom-by-atom [6] and perform single spin flips on individual atoms [7]. Here, we present the coherent excitation of a single magnon in several atomically assembled one-dimensional spin chains and readout of the subsequent spin dynamics by means of pump-probe spectroscopy [8, 9]. By controlling the amount of local magnetic field the STM tip applies to a weakly coupled readout spin, we are able to induce different magnetic resonances depending on the number of spins in the chain. Notably, we find that extending the structure by adding an atom to one end of the chain drastically changes the dynamics measured at the other end. This indicates that the single magnon indeed delocalizes over the rest of the chain after excitation. Simulations of the dynamics of the atomic spin chain using a Lindblad formalism [10] closely match the experiments, affirming that we indeed induce a single, local spin flip.

5.2. EXPERIMENTAL CONCEPT

We use a commercial low-temperature STM to build nanostructures out of individual hydrogenated Ti atoms on top of bilayer MgO islands grown on Ag(100) (See fig. 5.1A). Fe atoms were also deposited on the surface in order to construct spin polarized tips. Numerous previous studies have shown that hydrogenated Ti atoms on MgO are effective spin-1/2 particles that exhibit a strongly anisotropic g-factor [11–13]. The STM is fitted with high frequency cabling down to the tip, allowing for both GHz signals and short DC voltage pulses to be sent down to the junction for ESR-STM and pump-probe spectroscopy measurements. ESR-STM experiments were done at an experimental temperature of 1.5 K while pump-probe experiments were done at 400 mK.

We construct chains out of ^{48}Ti isotopes that do not show any hyperfine splitting in their ESR spectrum [14] and place them on horizontal bridge binding sites four unit cells apart. To be able to measure the free evolution of a spin excitation we add a readout atom that is weakly coupled to the chain compared to the intrachain coupling and placed on a vertical bridge site (see fig. 5.1B). This serves two purposes: first, the addition of an atom with a lower effective g-factor allows us to compensate for the tip field and control the amount of detuning between the control bit and the chain [9, 15]. Second, by having a

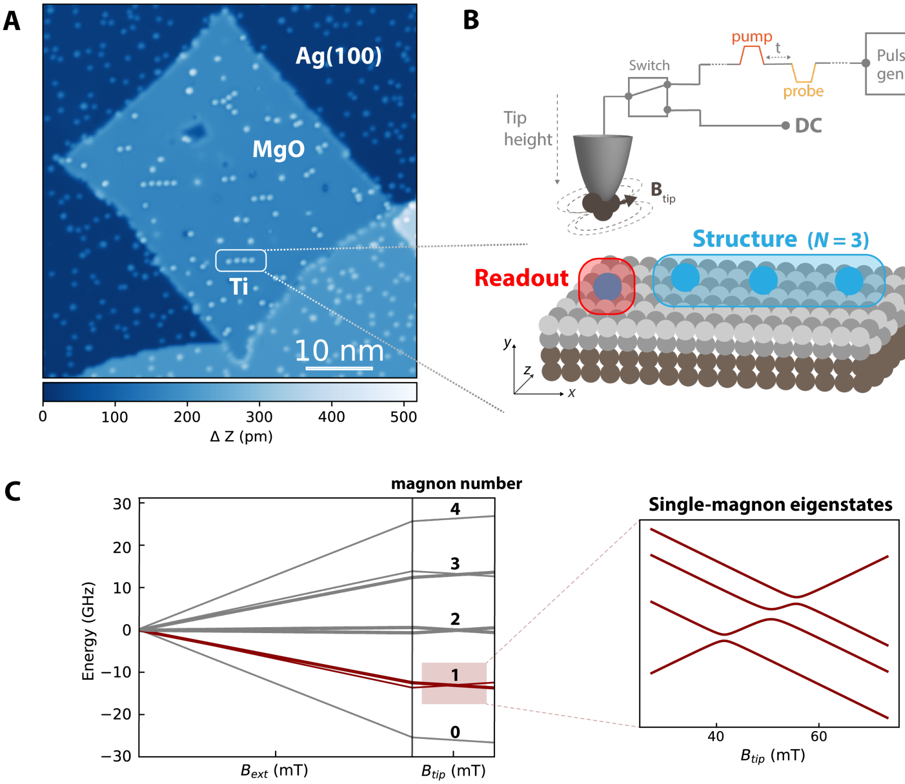

Figure 5.1: Magnon eigenstates in atomically built spin chains. A. STM topography of a bilayer MgO island on top of Ag(100) containing all atomic structures built out of Ti atoms discussed in this chapter (setpoint: 50 pA, 60 mV). **B.** Schematic picture of the experiment. The STM tip is approached on top of the readout atom that is weakly coupled to the structure. The external magnetic field is applied in-plane at a 15.5° with respect to the MgO lattice **C.** Calculated eigenstates of an ($N = 3$) atom spin chain connected to a readout spin as function of applied external and tip field. States containing a single spin flip are plotted in red. Zoom in: single magnon eigenstates as a function of applied tip field.

small coupling to the remainder of the chain we ensure that the DC pulse (8-10 ns) we use to inject the spin excitation into the control bit is faster than the dynamics between the control bit and the chain. This way, the spin excitation mostly stays localized on the readout spin for the duration of the excitation pulse.

We apply an in-plane external magnetic field of 480 mT, causing a large Zeeman energy that dominates over the interatomic coupling. The resulting eigenstates of an $N = 3$ chain connected to a readout spin are plotted in fig. 5.1C. Due to the dominant Zeeman term, the eigenstates are split in groups according to the number of spin flips present in each eigenstate. To understand the free evolution of a single magnon inside the chain, we only need to consider the eigenstates containing one spin flip, i.e. a single magnon (plotted in red). As the readout spin has a smaller g-factor compared to the rest, the most energetically favourable state for the magnon to be in is $|\uparrow\downarrow\downarrow\downarrow\rangle$. Here, a spin in state $|\downarrow\rangle$ is pointing along the direction of the external field. When we don't apply any extra field on the readout spin, the magnon will simply not leave the readout spin as it resides in a stationary eigenstate. However, as the local magnetic field of the tip increases - corresponding to a tip approach over the atom - the energy of this state increases (see zoom-in fig. 5.1C). When its energy comes close to that of another eigenstate, it mixes and forms an avoided level crossing. The number of avoided level crossings present as function of applied tip field depends directly on the number of sites the spin excitation can reside in i.e. the number of atoms in the structure: N. At these avoided crossing points we expect to measure dynamics as the magnon has two degenerate states it can be in. In other words, the initial state $|\uparrow\downarrow\downarrow\downarrow\rangle$ is no longer an eigenstate and the spin excitation will move through the structure.

5.3. MAPPING EXCHANGE AND DIPOLAR COUPLING

To correctly capture the dynamics of the spin chains, we need to model the coupling between the individual atoms in detail. We describe the system using the following Hamiltonians:

$$\hat{H}_{\text{Zeeman}} = \sum_i \mu_B g_i \hat{\mathbf{S}}_i \cdot (\mathbf{B}^{\text{ext}} + \mathbf{B}_i^{\text{tip}}) \tag{5.1}$$

and

$$\hat{H}_{\text{coupling}} = \sum_i J_{i,i+1} \hat{\mathbf{S}}_i \cdot \hat{\mathbf{S}}_{i+1} + D_{i,i+1}(3\hat{S}_i^z \hat{S}_{i+1}^z - \hat{\mathbf{S}}_i \cdot \hat{\mathbf{S}}_{i+1}). \tag{5.2}$$

Here, we sum over all atoms (readout atom and structure combined) using index i. The Zeeman Hamiltonian accounts for the energy splitting due to both external field and tip field scaled by the Bohr magneton μ_B and the g-factor of each atom g_i. The coupling Hamiltonian consists of two parts: first, a Heisenberg exchange term with isotropic coupling constant defined as $J = J_0 e^{-(r-r_0)/d}$, with r the distance between the atoms and d the decay constant. Second, a dipolar term with the dipolar constant defined as $D = D_0(1-3\cos^2(\theta))/2\pi r^3$, with θ the angle between the vector connecting the two atoms and the direction of the external field as previously used in chapter 4 and described in [11].

To model the coupling between any two Ti atoms correctly, we need to determine the values of the constants, J_0, D_0, r_0, d, in the functions given above. We do this by measuring the ESR splitting due to the combined coupling $J + 2D$ (see chapter 4) for 22 dimers with different r and θ (See fig. 5.2A). Both fig. 5.2B and fig. 5.2C show the measured energy spectra for one of these dimers with a corresponding fit to extract the splitting. Depending on the coupling strength, either 2 or 4 peaks are visible (see chapter 4). In every case, the lowest energy peak has a larger amplitude, indicating antiferromagnetic coupling [11].

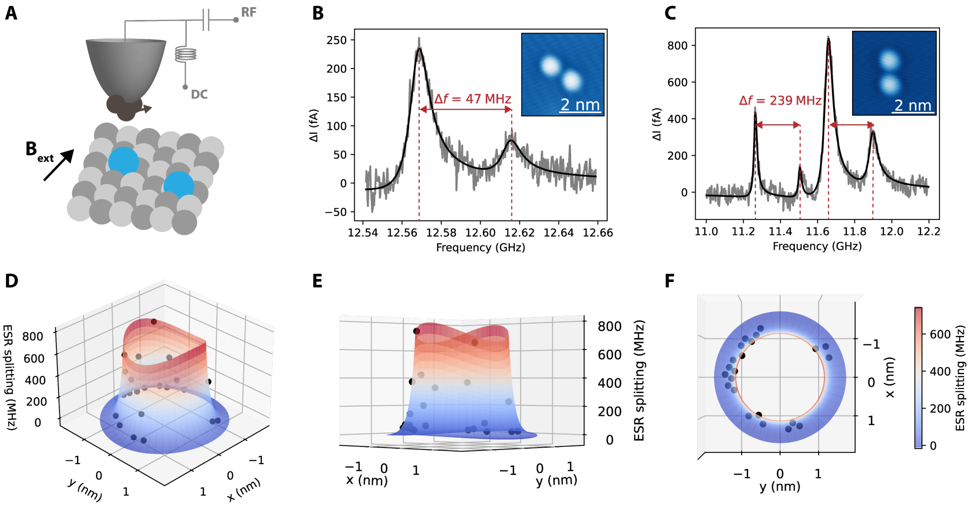

Figure 5.2: Extracting exchange and dipolar coupling constants. A. Schematic picture of an ESR-STM experiment on a dimer. **B,C.** ESR spectra taken on two different dimers (setpoint **B**: 8 pA, 60 mV, setpoint **C**: 50 pA, 60 mV, $T = 1.5$ K). Insets: topographies of the dimers. **D,E,F** 3D plot of the total coupling $J + 2D$. Black dots: data retrieved from the fits of 22 different dimers. Colored isosurface: a fit through the data in order to extract the coupling parameters.

We create a 3D plot of the measured ESR splitting as a function of dimer position, shown in fig. 5.2D, E and F. Each black dot represents the $J + 2D$ value extracted from a particular dimer. The colored isosurface is a 3D fit though the data to extract the coupling parameters. We find a sharp exponential increase as a function of r due to the exchange term and a smaller modulation as a function of θ due to the dipolar term. The resulting constants are: $J_0 = 722 \pm 23$ MHz at $r_0 = 1.0525$ nm, $d = 0.122 \pm 0.005$ nm and $D_0 = 158 \pm 42$ MHz where the error bars correspond to the standard deviation of the fits.

5.4. ATOMIC CHAINS

We build multiple spin chains of length $N = 1$ to $N = 4$ coupled to a single readout spin as described in section 5.2. Topographies of each of these chains are shown in fig. 5.3, together with experimental pump-probe data taken on the readout spin, the calculated single-magnon eigenstates and Lindblad simulations of the dynamics. We will first turn our attention to the experimental data. Prior to the pump probe experiments, we performed a calibration ESR measurement on a dimer with identical spacing as between the readout atom and the chain to find the tuning point, as was done in chapter 4. This way we were able to select suitable magnetic microtips and determine the range of tip heights at which we could expect dynamics in the pump-probe data. For ESR measurements on all structures, see section 5.8.

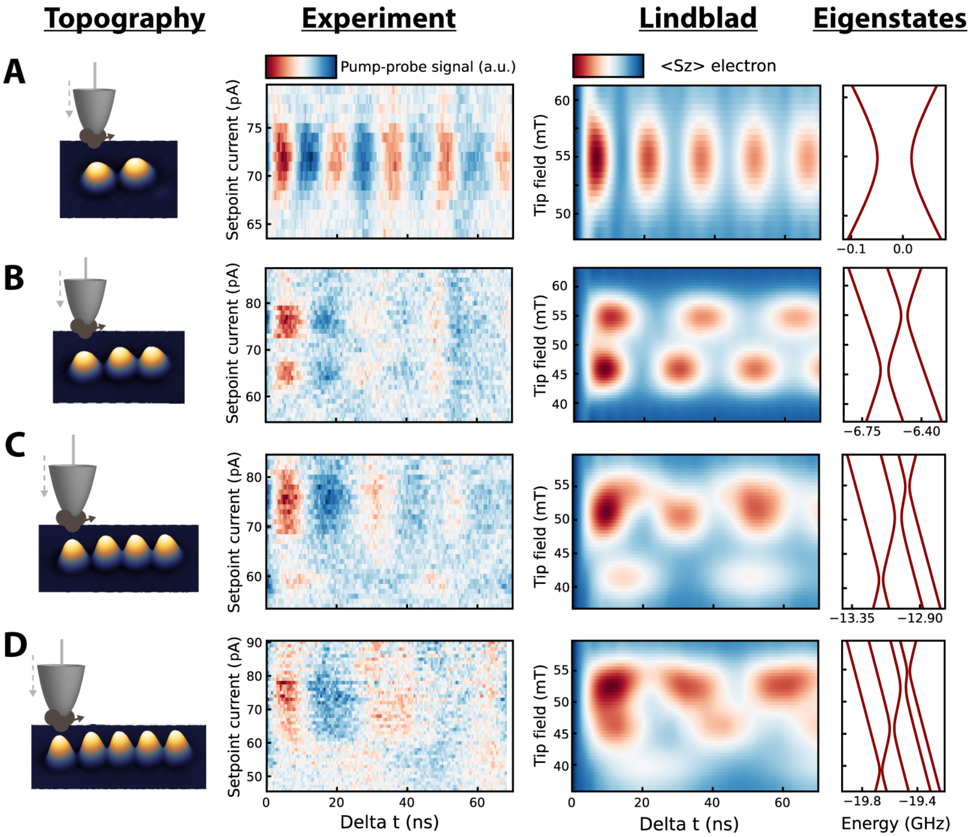

Figure 5.3: Single magnon spin dynamics in atomic chains. A-D pump-probe experiments and simulations on chains of length $N = 1$ to $N = 4$. Left: topographies of the spin chains built atom-by-atom (setpoint: 20 pA, 60 mV). Center: pump-probe spectroscopy experiments performed on the readout spin of each chain. Right: single-magnon eigenstates and Lindblad simulations of the dynamics of the readout spin initialized to the $|\uparrow\downarrow\downarrow\downarrow\rangle$ state. Experimental settings: setpoint voltage 60 mV, $T = 400$ mK, **A.** pump: +100 mV, 8 ns, probe: −100 mV, 8 ns. **B.** pump: +100 mV, 8 ns, probe: −100 mV, 8 ns. **C.** pump: +50 mV, 10 ns, probe: −50 mV, 10 ns. **D.** pump: +100 mV, 8 ns, probe: −50 mV, 13 ns.

The $N = 1$ case (fig. 5.3A) is simply a dimer with the exact same spacing as has been studied in detail in chapter 4. During the pump-probe experiment the pump pulse flips the spin of the readout atom which sets off an oscillation between the two spins when the local tip field, tuned by adjusting the setpoint current, is such that the two spins exhibit entangled eigenstates. When we add an atom to the end of the chain ($N = 2$, fig. 5.3B), we find distinct oscillations at two different tip heights. Adding another atom ($N = 3$, fig. 5.3C) leads to a significantly slower oscillation at a lower setpoint (∼ 58 pA) and a broad, faster oscillation at a higher setpoint (∼ 70-80 pA). Adding a last atom ($N = 4$, fig. 5.3D) shows a complicated oscillation pattern where it is challenging to distinguish the individual tuning points. The fact that the dynamics measured at the readout spin located on one end of the chain drastically change when an atom is added to the other end of the chain indicates that the inserted magnon indeed delocalizes over the entire structure.

To understand the patterns we observe for the different chains we simulate the dynamics using Lindblad equations. We model the system using the Hamiltonians presented above and the coupling constants we measured using ESR-STM in section 5.3 so that the simulations are independent from the pump-probe measurements. The colorplots show the time evolution of the expectation value of S_z for the readout spin at different B^{tip} values after the system is initialized in the $|\uparrow\downarrow\downarrow\downarrow\rangle$ state at time $t = 0$. The results are convoluted with a 2.5 mT Gaussian distribution along the vertical axis to simulate magnetic noise originating from mechanical vibrations of the STM tip present in the experiment. We find a very good agreement between theoretical predictions and the experimental data in the colorplots. We attribute minor differences to deviations in the coupling parameters and the g-factors due to local variations in the underlying surface [12, 16] as well as local disturbances in the lattice caused by the neighbouring Ti atoms within the chain [17, 18].

We can relate the observed dynamics to the energy diagrams of the structures as shown in fig. 5.3. At field values where we find dynamics, avoided level crossings occur between different eigenstates. For each atom that we add to the chain, we find an extra eigenstate in the single-magnon state space, resulting in an additional avoided level crossing. In the following section, we will deduce the spin dynamics occurring inside the chain from these specific avoided level crossings between single-magnon eigenstates.

5.5. AVOIDED LEVEL CROSSINGS

To gain insight into the nature of the magnon excitation, we calculate the change in composition of the eigenstates as function of B^{tip}. We schematically show the single-magnon eigenstates of the $N = 3$ chain in fig. 5.4. Here, state $|0\rangle$ is the ground state in which no magnon is present and all spins (including the readout atom) are pointing along the external magnetic field: $|\downarrow\downarrow\downarrow\downarrow\rangle$. The first 4 excited states form the single-magnon eigenstates, as the magnon is allowed to reside on any of the 4 atoms in the entire structure. When the STM tip does not apply any local field on the readout spin, it is detuned from the chain: the magnon is either localized on the readout spin (state $|1\rangle$) or delocalized over the 3-atom chain (states $|2\rangle$, $|3\rangle$ and $|4\rangle$). The delocalized eigenstates are nearly identical to the solutions for a 3-atom chain without any readout spin: they each consist of one of three standing wave modes confined in the chain. These states are are expressed in terms of Zeeman product states in the table inset in fig. 5.4. All higher states $|>4\rangle$ contain more than one spin flip and therefore should be only minimally populated after the initial pump pulse. Therefore, we do not take them into account in our analysis.

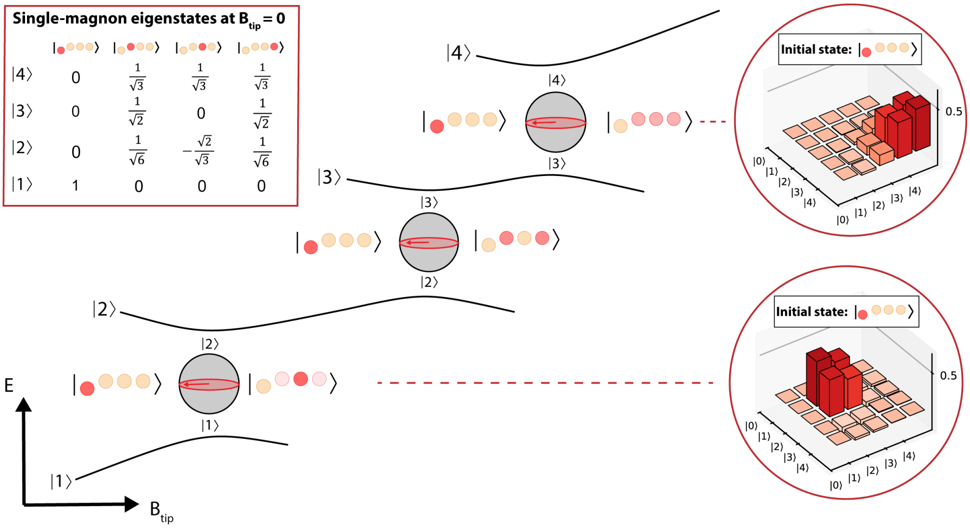

Single-magnon eigenstates at $B_{tip} = 0$

	$\|$●○○○$\rangle$	$\|$○●○○$\rangle$	$\|$○○●○$\rangle$	$\|$○○○●$\rangle$
$\|4\rangle$	0	$\frac{1}{\sqrt{3}}$	$\frac{1}{\sqrt{3}}$	$\frac{1}{\sqrt{3}}$
$\|3\rangle$	0	$\frac{1}{\sqrt{2}}$	0	$\frac{1}{\sqrt{2}}$
$\|2\rangle$	0	$\frac{1}{\sqrt{6}}$	$-\frac{\sqrt{2}}{\sqrt{3}}$	$\frac{1}{\sqrt{6}}$
$\|1\rangle$	1	0	0	0

Figure 5.4: Schematic picture of the single-magnon eigenstates of an $N = 3$ chain. Bloch spheres inside the avoided level crossings visualize the reduced 2-by-2 state space of the relevant energy levels. Dynamics at these points arise from the phase rotation between the states on the equator of the Bloch spheres: the $|\uparrow\downarrow\downarrow\downarrow\rangle$ state and one of the eigenmodes of the chain. Inset top right: eigenmodes of the 3 atom chain. Inset top left: calculated reduced density matrix for the highest energy avoided level crossing. Inset bottom right: calculated reduced density matrix for the lowest energy avoided level crossing.

When we add a local field to the readout spin by approaching the STM tip, the $|\uparrow\downarrow\downarrow\downarrow\rangle$ spin state gains energy. When this state comes close to another single-magnon eigenstate, they form an avoided level crossing due to the $S_i^x S_{i+1}^x$ and $S_i^y S_{i+1}^y$ terms in the exchange and dipolar parts of the coupling Hamiltonian (eq. (5.2)). At these avoided level crossings, the eigenstates form superpositions between the $|\uparrow\downarrow\downarrow\downarrow\rangle$ state and one of the single-magnon modes of the chain. We visualize this by plotting Bloch spheres of the reduced 2-by-2 state spaces inside the avoided level crossings in fig. 5.4. At the center of these avoided crossing, a flip of the readout spin projects the state $|\uparrow\downarrow\downarrow\downarrow\rangle$ exactly at the equator of one of these Bloch spheres, setting off an oscillation between $|\uparrow\downarrow\downarrow\downarrow\rangle$ and one of the single magnon eigenmodes of the chain. In other words, by controlling the tip field we can inject a single magnon into a specific eigenmode of the spin chain via the readout spin. These are the different oscillations we observe in the pump-probe spectroscopy experiments.

The Bloch sphere picture described above only allows to describe an effective two level system. In order to give a more comprehensive picture of the initial state, we also plot the calculated reduced density matrix for two of the avoided level crossings in fig. 5.4. At the lowest energy avoided crossing, between $|1\rangle$ and $|2\rangle$, the initial state is a near equal superposition of the two eigenstates and the resulting oscillation is driven only by the coherence between the two. The Bloch sphere picture described above thus accurately captures the dynamics at play. The higher energy crossings, however, are closer together and overlap slightly. Therefore, the initial state is spread out over multiple populations and coherences leading to more complex dynamics, as seen in fig. 5.3C and D. When adding more atoms to these chains or by increasing the coupling energy, all these avoided level crossings start overlapping and we approach the regime of band formation. In that case, the excitation of a single magnon populates many eigenstates and dynamics are the result of many coherences with different frequencies. The magnon then starts behaving like a traveling spin wave moving through the entire chain [19, 20].

5.6. BRANCHED STRUCTURE

In the previous sections, we have shown that individual magnon modes can be selectively accessed by tuning the STM tip height. We now proceed to harness this behavior to steer a magnon in different directions over the sample surface using the same tip height tuning method. We therefore build a quasi 2D branched structure (as sketched in fig. 5.5A) that consists of a readout spin coupled to two arms. The atoms in the top arm are spaced closer together and therefore are coupled more strongly compared to the bottom arm. When performing pump-probe spectroscopy on the readout spin we find two distinct oscillations: a faster one at lower tip field and a slower one at higher tip field values. The Lindblad simulations match the experiments qualitatively very well but show slightly longer periods which we again attribute to local variations in the actual coupling strengths.

By looking at the single-magnon eigenstate solutions in fig. 5.5A, we find that we actually expect four separate tuning points instead of the observed two. However, two of the four avoided level crossings in the diagram have a very small gap of only several MHz. Because we have a 2.5 mT smearing due to the mechanical vibrations of the STM tip, these very sharp tuning points are invisible in our experiment. By matching the calculated dynamics to the observed oscillations we identify which processes happen inside the different branches. The important avoided crossing and the resulting dynamics are illustrated in fig. 5.5B. The oscillation at low tip field (~ 65 mT) corresponds to a mixture of states $|2\rangle$ and $|3\rangle$, leading to dynamics between the readout spin and the outer two atoms of the top arm. At the observed high field oscillation (~ 75 mT) two avoided crossings play a role. First, a very slow ~ 2 MHz dynamic involving only the bottom arm (states $|4\rangle$ and $|5\rangle$). Second, a faster, dominant dynamic involving both arms (states $|5\rangle$ and $|6\rangle$) which better matches the experimental observation. Both avoided crossings overlap slightly (as can be seen from the density matrices plotted in fig. 5.5B) but should be individually addressable in theory. However, due to the 2.5 mT smearing originating from the mechanical vibrations of the tip, only the second dynamic is visible in the experiment.

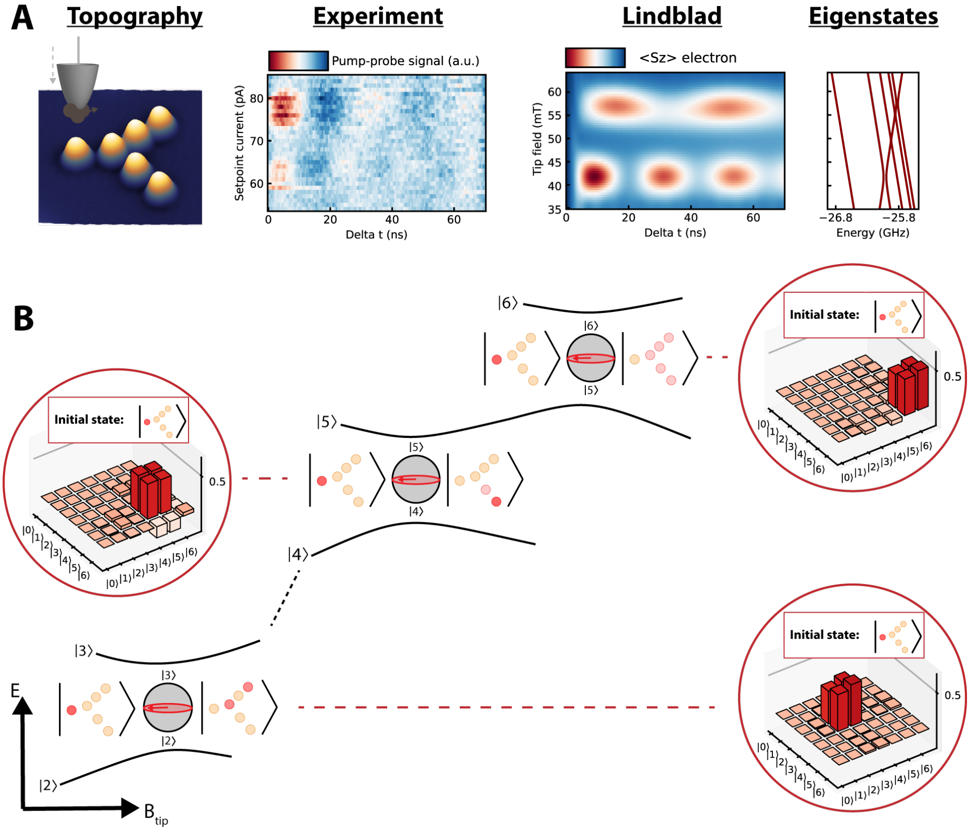

Figure 5.5: single magnon dynamics in a branched structure. **A.** Left: STM topography of the atomically built branched structure consisting of 6 Ti atoms. Center: Pump probe experiment (setpoint voltage = 60 mV, pump: +80 mV, 8 ns, probe: −60 mV, 13 ns). Right: single-magnon eigenstates of the structure and Lindblad simulations of the dynamics after flipping the readout spin. **B.** Schematic picture of the two avoided level crossings that give rise to the dynamics. Bloch spheres are shown where the initial state forms a superposition with one of the modes in the branched structure. In case of the low field crossing a mode located in the top arm, while the high field crossing corresponds to a mode that is delocalized over both arms. Insets show the density matrices of the initial state at each avoided level crossing.

These results show that we still achieve some level of directionality over the spin excitation: by controlling the height of the STM tip we can put the magnon either in the top arm of the structure or delocalized equally over both arms. Optimizing the technique further by fine-tuning the Hamiltonian design or eliminating the vibrational noise would lead to enhanced control over the direction of magnon. This shows the potential of STM to control the coherent transmission of magnetic information through atomically built nanomagnets using the magnetic probe tip.

5.7. CONCLUSIONS

Using nanosecond DC pulses we are able to inject a single magnon into nanomagnets built atom-by-atom via a readout spin. By tuning the local field using the height of the magnetic STM tip, we address individual single-magnon modes within the chain. Lindblad simulations based on independent ESR-STM measurements show remarkable agreement with the experimental data, allowing us to design functional nano structures. By building a branched structure we could, to some extent, control the direction in which the magnon propagates: it either oscillates between readout and one arm of the structure or between readout and both arms equally. These experiments provide insight into single magnon dynamics in the few atom limit as well as show the potential for atomically built structures on a surface to transmit coherent spin information.

5.8. APPENDIX: ESR MEASUREMENTS

Next to pump-probe measurements as function of applied tip field, we performed ESR-STM experiments as function of tip height on the readout spin of each structure, as shown in fig. 5.6. These experiments are similar to ones performed on different chains built from Ti atoms in [21]. However, there are two main differences: first, in our case, a readout spin is placed on a low g-factor binding site allowing us to observe avoided crossings in the ESR spectra. Second, the intra-chain coupling is much weaker in our case compared to [21]. This allows us to observe the free, coherent spin dynamics in pump-probe experiments with finite DC pulse widths.

Our results are shown in fig. 5.6. The single atom case (fig. 5.6A) shows a linear increase of the ESR resonance with tip height indicating exchange coupling between the magnetic tip and Ti atom. The dimer ($N = 1$, fig. 5.6B) shows a single gap due to the avoided crossing, nearly identical to the results presented in chapter 4. The $N = 2$ chain (fig. 5.6C) shows two gaps due to the two avoided crossings present in the eigenstates (see fig. 5.3B). In the larger structures (fig. 5.6D, E and F) no distinguishable gaps are observable anymore. This is due to two causes: first, the energy gap of some of the avoided crossings is smaller for the larger structures, making them harder to see. Second, there are more states present and therefore more ESR transitions with very similar resonance frequencies. For example, in the ESR sweeps on the branched structure we observe only a single peak but this consists probably of multiple resonances that fall within our linewidth. All in all, this makes the avoided crossing gaps harder to observe for larger structures. Therefore, we used a benchmark ESR measurement on a dimer to obtain a rough estimation for the tip height where we expect dynamics in the larger structures. We used this setpoint as a starting position for our pump-probe measurements.

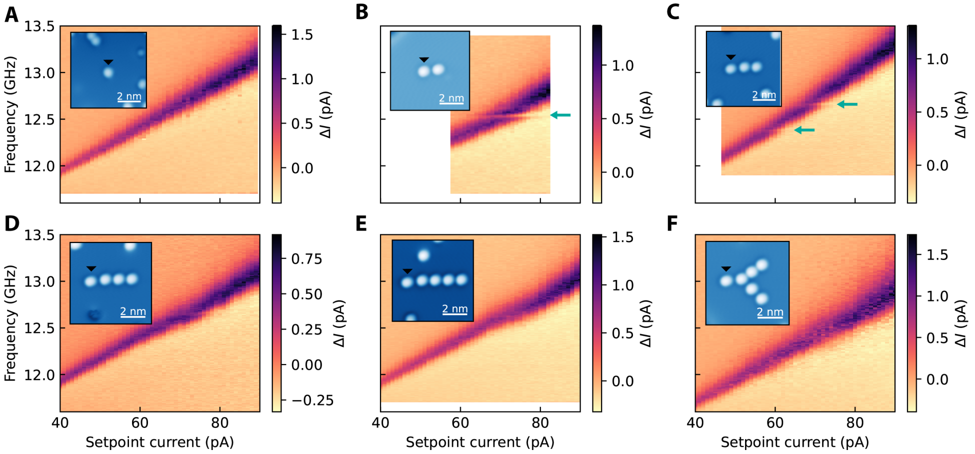

Figure 5.6: ESR measurements as function of tipheight on the readout spin of structures described in this chapter. A. Single atom. **B-E.** chains $N = 1$ to $N = 4$. **F.** Branched structure. Experimental parameters: setpoint voltage = 60 mV, T = 1.5K

REFERENCES

[1] **L. M. Veldman**, L. Farinacci, and S. Otte. “Coherent single magnon dynamics at the atomic scale”. *In preparation.*

[2] J. Hortensius, D. Afanasiev, M. Matthiesen, R. Leenders, R. Citro, A. Kimel, R. Mikhaylovskiy, B. Ivanov, and A. Caviglia. “Coherent spin-wave transport in an antiferromagnet”. In: *Nature physics* 17.9 (2021), pp. 1001–1006.

[3] D. Lachance-Quirion, Y. Tabuchi, A. Gloppe, K. Usami, and Y. Nakamura. “Hybrid quantum systems based on magnonics”. In: *Applied Physics Express* 12.7 (2019), p. 070101.

[4] A. V. Chumak, V. I. Vasyuchka, A. A. Serga, and B. Hillebrands. “Magnon spintronics”. In: *Nature physics* 11.6 (2015), pp. 453–461.

[5] I. Bertelli, J. J. Carmiggelt, T. Yu, B. G. Simon, C. C. Pothoven, G. E. Bauer, Y. M. Blanter, J. Aarts, and T. Van Der Sar. “Magnetic resonance imaging of spin-wave transport and interference in a magnetic insulator”. In: *Science advances* 6.46 (2020), eabd3556.

[6] S. Loth, S. Baumann, C. P. Lutz, D. Eigler, and A. J. Heinrich. “Bistability in atomic-scale antiferromagnets”. In: *Science* 335.6065 (2012), pp. 196–199.

[7] A. J. Heinrich, J. A. Gupta, C. P. Lutz, and D. M. Eigler. “Single-atom spin-flip spectroscopy”. In: *Science* 306.5695 (2004), pp. 466–469.

[8] S. Loth, M. Etzkorn, C. P. Lutz, D. M. Eigler, and A. J. Heinrich. “Measurement of fast electron spin relaxation times with atomic resolution”. In: *Science* 329.5999 (2010), pp. 1628–1630.

[9] **L. M. Veldman**, L. Farinacci, R. Rejali, R. Broekhoven, J. Gobeil, D. Coffey, M. Ternes, and A. F. Otte. “Free coherent evolution of a coupled atomic spin system initialized by electron scattering”. In: *Science* 372.6545 (2021), pp. 964–968.

[10] J. R. Johansson, P. D. Nation, and F. Nori. “QuTiP: An open-source Python framework for the dynamics of open quantum systems”. In: *Computer Physics Communications* 183.8 (2012), pp. 1760–1772.

[11] K. Yang, Y. Bae, W. Paul, F. D. Natterer, P. Willke, J. L. Lado, A. Ferrón, T. Choi, J. Fernández-Rossier, A. J. Heinrich, *et al.* “Engineering the eigenstates of coupled spin-1/2 atoms on a surface”. In: *Physical Review Letters* 119.22 (2017), p. 227206.

[12] M. Steinbrecher, W. M. Van Weerdenburg, E. F. Walraven, N. P. Van Mullekom, J. W. Gerritsen, F. D. Natterer, D. I. Badrtdinov, A. N. Rudenko, V. V. Mazurenko, M. I. Katsnelson, *et al.* “Quantifying the interplay between fine structure and geometry of an individual molecule on a surface”. In: *Physical Review B* 103.15 (2021), p. 155405.

[13] J. Kim, W.-j. Jang, T. H. Bui, D.-J. Choi, C. Wolf, F. Delgado, Y. Chen, D. Krylov, S. Lee, S. Yoon, *et al.* “Spin resonance amplitude and frequency of a single atom on a surface in a vector magnetic field”. In: *Physical Review B* 104.17 (2021), p. 174408.

[14] P. Willke, Y. Bae, K. Yang, J. L. Lado, A. Ferrón, T. Choi, A. Ardavan, J. Fernández-Rossier, A. J. Heinrich, and C. P. Lutz. “Hyperfine interaction of individual atoms on a surface”. In: *Science* 362.6412 (2018), pp. 336–339.

[15] Y. Bae, K. Yang, P. Willke, T. Choi, A. J. Heinrich, and C. P. Lutz. “Enhanced quantum coherence in exchange coupled spins via singlet-triplet transitions”. In: *Science Advances* 4.11 (2018), eaau4159.

[16] S. Baumann, W. Paul, T. Choi, C. P. Lutz, A. Ardavan, and A. J. Heinrich. “Electron paramagnetic resonance of individual atoms on a surface”. In: *Science* 350.6259 (2015), pp. 417–420.

[17] B. Bryant, A. Spinelli, J. Wagenaar, M. Gerrits, and A. Otte. “Local control of single atom magnetocrystalline anisotropy”. In: *Physical Review Letters* 111.12 (2013), p. 127203.

[18] C. F. Hirjibehedin, C.-Y. Lin, A. F. Otte, M. Ternes, C. P. Lutz, B. A. Jones, and A. J. Heinrich. “Large magnetic anisotropy of a single atomic spin embedded in a surface molecular network”. In: *Science* 317.5842 (2007), pp. 1199–1203.

[19] J. Gauyacq and N. Lorente. “Excitation of spin waves by tunneling electrons in ferromagnetic and antiferromagnetic spin-1/2 Heisenberg chains”. In: *Physical Review B* 83.3 (2011), p. 035418.

[20] A. Spinelli, B. Bryant, F. Delgado, J. Fernández-Rossier, and A. F. Otte. “Imaging of spin waves in atomically designed nanomagnets”. In: *Nature materials* 13.8 (2014), pp. 782–785.

[21] K. Yang, S.-H. Phark, Y. Bae, T. Esat, P. Willke, A. Ardavan, A. J. Heinrich, and C. P. Lutz. “Probing resonating valence bond states in artificial quantum magnets”. In: *Nature communications* 12.1 (2021), p. 993.

6

GROUNDSTATE DETERMINATION THROUGH HYPERFINE ANISOTROPY

To a worm in horseradish
the world is horseradish.

Old Yiddish proverb

Historically, electron spin resonance (ESR) has provided excellent insight into the electronic, magnetic, and chemical structure of samples hosting spin centers. In particular, the hyperfine interaction between the electron and the nuclear spins yields valuable structural information about these centers. In recent years, the combination of ESR and scanning tunneling microscopy (ESR-STM) has allowed to acquire such information about individual spin centers of magnetic atoms bound atop a surface, while additionally providing spatial information about the binding site. Here, we conduct a full angle-dependent investigation of the hyperfine splitting for individual hydrogenated titanium atoms on MgO/Ag(001) by measurements in a vector magnetic field. We observe strong anisotropy in both the g factor and the hyperfine tensor. Combining the results of the hyperfine splitting with the symmetry properties of the binding site obtained from STM images and a basic point charge model allows us to predict the shape of the electronic ground state configuration of the titanium atom. Relying on experimental values only, this method paves the way for a new protocol for electronic structure analysis for spin centers on surfaces.

The results in this chapter were conceived in close collaboration with L. Farinacci, P. Willke and S. Otte.

Parts of this chapter have been published in *Nano Letters* **22** (2022) [1].

Calculations to obtain the groundstate orbital using the point charge model were performed by Dr. Laëtitia Farinacci.

6.1. INTRODUCTION

For decades, nuclear spins have constituted an excellent resource to gain information about the atomic scale [2]. In recent years, advances in many different architectures, including nitrogen vacancy centers in diamond [3], molecular break junctions [4], and phosphorus donors in silicon [5], even allowed to address them on an individual level. This effort is mainly driven by their prospect as a future building block in quantum information processing and sensing [6]. However, nuclear spins have been used for even longer to gain structural and electronic information about materials in bulk experiments. The nuclei can be probed directly using nuclear magnetic resonance measurements as well as indirectly via ESR because the magnitude and anisotropy of the hyperfine interaction are reflected in properties of the electron cloud surrounding the nucleus [2].

The combination of electron spin resonance and scanning tunneling microscopy (ESR-STM) has opened a novel platform to access single nuclear spins of atoms on surfaces [7–10]. Most strikingly, both spatial and magnetic information can be obtained by the two techniques simultaneously, providing unique access to hyperfine interaction on the atomic scale. Previous experiments showed that the hyperfine interaction of individual hydrogenated titanium (Ti) atoms on a bilayer of magnesium oxide (MgO) strongly depends on the binding side [8]. Initial experiments hinted toward a strong anisotropic hyperfine interaction on all binding sides. However, these measurements were performed in one magnetic field direction only; this limited the electronic structure analysis and required the additional help of density functional theory (DFT) to interpret the data [8].

Here, we perform ESR-STM measurements of individual hydrogenated Ti atoms on a bridge binding side of MgO in a vector magnetic field. We demonstrate that the hyperfine tensor has distinctly different values along its principal axes than reported previously [8]. Combining the results from the hyperfine analysis with properties of the symmetry group of the atom's binding site derived from STM and a basic point charge model allows us to predict the shape of the ground state orbital of the atom without the use of first-principles calculations such as DFT.

6.2. SYSTEM OF STUDY

Experiments were conducted in a commercial STM system (Unisoku USM1300) equipped with a vector magnetic field (fig. 6.1A) and at a temperature of 1.5 K. The measurements were performed on well-isolated individual Ti atoms adsorbed on two atomic layers of MgO grown on a Ag(100) substrate. These titanium atoms were found to be hydrogenated by residual hydrogen in the vacuum chamber [11], effectively reducing them to Ti with spin $S = 1/2$. fig. 6.1B shows a STM topography of a single hydrogenated Ti atom. For ESR experiments, a radio-frequency (RF) voltage V_{RF} is applied to the STM tip in addition to the DC bias voltage V_{DC}. This RF voltage can drive transitions between the two lowest lying spin states of the Ti atom, which is subsequently detected by changes in the tunnel current ΔI via magnetoresistive tunneling. For the latter, a magnetic STM tip

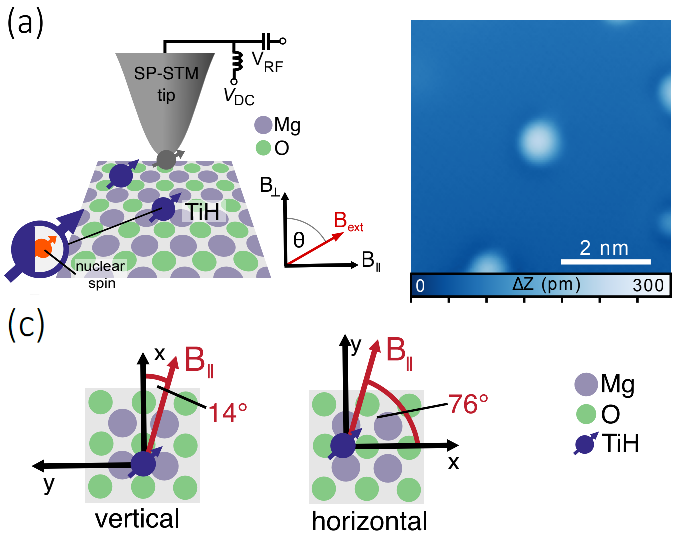

Figure 6.1: Electron spin resonance in a scanning tunneling microscope with a vector magnet. **A.** Schematic of the experiment. **B.** Topography image of a Ti atom on MgO ($I = 20$ pA, $V_{DC} = 60$ mV). **C.** We study Ti atoms adsorbed on two equivalent bridge sites, vertical and horizontal, which effectively correspond to two different directions of the in-plane field $B_\parallel$.

is employed that is created by transferring several Fe atoms from the surface to the STM apex. We study hydrogenated Ti atoms adsorbed on O-O bridge sites, which come in two equivalent orientations as shown in fig. 6.1C: “horizontal” and “vertical”, which have an in-plane magnetic field angle with respect to the crystal lattice of 14° and 76°, respectively. This leads effectively to two different orientations of the in-plane field and thus allows for a 3-dimensional mapping of the hyperfine interaction by rotating the magnet only in a single plane.

In accordance with ref [8], we can identify three different configurations of the Ti nuclear spin. In fig. 6.2, we display different ESR spectra measured above atoms adsorbed on vertical bridge sites; we observe a single ESR resonance for ^{46}Ti, ^{48}Ti, and ^{50}Ti ($I = 0$), six resonances for ^{47}Ti ($I = 5/2$), and eight for ^{49}Ti ($I = 7/2$). In line with previous experiments, we observe a variation of the overall signal intensity for different magnetic field angles [12]. Interestingly, for the isotopes carrying a nonzero nuclear spin, the different peaks are well-resolved when the external field is along the sample plane, with a splitting around ∼ 65 MHz, while they seem to merge when the field is aligned in the out-of-plane direction, with an ∼ 20 MHz splitting. This strong anisotropy of the hyperfine splitting is remarkable and could not be accurately determined with measurements performed along a single field direction [8].

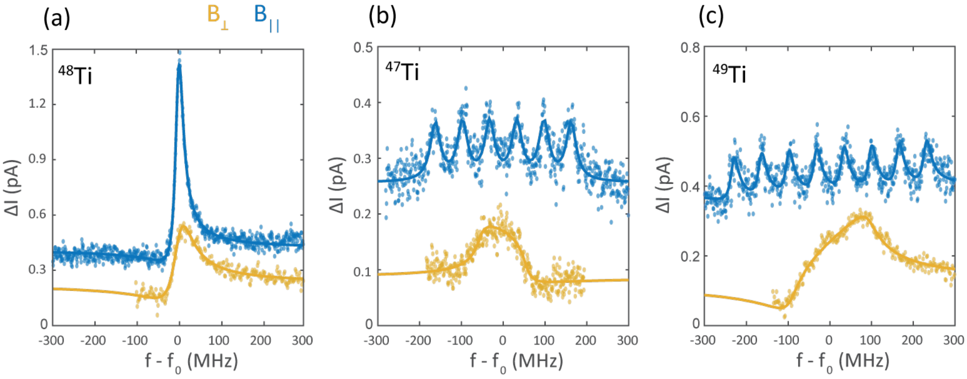

Figure 6.2: Hyperfine anisotropy of different Ti isotopes. A,B,C. ESR spectra of different hydrogenated Ti isotopes adsorbed on vertical bridge sites in an external magnetic field pointing in-plane (blue) and out-of-plane (orange). Traces were offset with respect to each other for clarity. Experimental parameters: $V_{\mathrm{DC}} = 60$ mV, $I = 8 - 10$ pA, $V_{\mathrm{RF}} = 45 - 57$ mV, $|B_{\mathrm{ext}}| = 0.86 - 1.037$ T, and $f_0 = 24.10 - 24.48$ GHz.

6.3. HYPERFINE INTERACTION

In fig. 6.3, we map the full evolution of the ESR spectra as a function of θ, the angle of the magnetic field with respect to the surface normal, for two perpendicular rotation planes. fig. 6.3A shows data taken on a hydrogenated ^{49}Ti atom on a vertical bridge site, meaning that the in-plane field makes a 14° angle with the x-axis. The data exhibit strong anisotropic behavior, with almost complete suppression of the hyperfine splitting for the out-of-plane field direction. All data in this panel were acquired with the same microtip, and by measuring for each data point a reference spectrum on a hydrogenated ^{48}Ti atom, we can ensure that the influence of the tip field is negligible.

We performed the same experiment on another hydrogenated ^{49}Ti atom adsorbed on a horizontal bridge site, with a different microtip but that is again kept the same for the whole data set (see fig. 6.3B). Also here, we observe anisotropic behavior of the hyperfine splitting, though much less dramatic than for the vertical binding site. The evolution of the hyperfine splitting can be quantified by fitting each spectrum with several Fano functions (see chapter 3) and is shown in fig. 6.3C for both adsorption sites. The evolution of the hyperfine splitting is continuous and mirror-symmetric, indicating that the sign of the magnetic field along any direction is irrelevant. We note that the observed symmetry axis is rotated by ~10° with respect to the magnet axes. We discuss possible origins for this rotation in section 6.7.1. From the anisotropic evolution of the hyperfine splitting in fig. 6.3C we can already infer that the extent of the ground state orbital, which scales the hyperfine splitting via the magnetic dipole-dipole interaction, is likely to be similar in two directions (out-of-plane and one in-plane) and differs substantially in the other (in-plane) one.

6.4. ORIGINS OF ANISOTROPY

The anisotropy of the hyperfine splitting is closely related to that of the g factor. The latter had already been observed for hydogenated Ti on MgO/Ag(100) [12–14]. The hyperfine interaction entails three different interactions: a dipole-dipole interaction between the electron and nuclear spins, a Fermi contact interaction that scales with the electron density at the position of the nucleus, and an orbit dipolar interaction that couples the nuclear spin and angular momentum of the unpaired electron. Spin-orbit coupling leads to a partially unquenched angular momentum which couples to the electron spin. Treating this effect up to second order with perturbation theory, one can write a spin Hamiltonian in which, in all generality, **g** and **A** are tensors [2]:

$$\hat{H}_{\text{spin}} = \mu_{\text{B}} \mathbf{B} \cdot \mathbf{g} \cdot \hat{\mathbf{S}} + \hat{\mathbf{S}} \cdot \mathbf{A} \cdot \hat{\mathbf{I}}. \tag{6.1}$$

The symmetry of the adsorption site often lowers the degree of anisotropy of these tensors for a particular set of axes (x, y, z). In fact, in traditional ESR spectroscopy, analysis of the hyperfine anisotropy in a vector magnetic field is used to determine the symmetry of the crystal field around the investigated species [2, 15, 16]. This powerful method compensates for the lack of spatial resolution in these ensemble measurements and permits to even observe effects due to hybridization with ligand orbitals [17]. In our case, the combination of ESR with STM allows us to measure ESR spectra of single atoms, while the symmetry of the adsorption site can be exactly determined by STM. As we show, we can thus perform an all-experimental electronic analysis to determine the shape of the ground state orbital, a quantity that has been long elusive for experimentalists.

The adsorption site of the atom has a C_{2v} symmetry (see fig. 6.4) so that **g** and **A** are vectors along the principal axes (x, y, z) of the crystal lattice [17]. In the presence of an external magnetic field that has (l, m, n) directional cosines with respect to these axes, the effective g and A parameters are given by [2]:

$$g = \sqrt{(l g_x)^2 + (m g_y)^2 + (n g_z)^2} \tag{6.2}$$

and

$$A = \frac{1}{g} \sqrt{(l g_x A_x)^2 + (m g_y A_y)^2 + (n g_z A_z)^2}. \tag{6.3}$$

Using these two equations, we first determine the effective g values for the vertical and horizontal bridge sites corresponding to different in-plane fields. We find that the vector **g** is completely anisotropic with $g_x = 1.702 \pm 0.004$, $g_y = 1.894 \pm 0.004$, and $g_z = 2.011 \pm 0.015$. These values are in good agreement with the literature values [12], and the small deviations can be explained by the presence of a small residual tip field. Because this tip field has been carefully accounted for by Kim et al., we use in the following their reported g values [12].

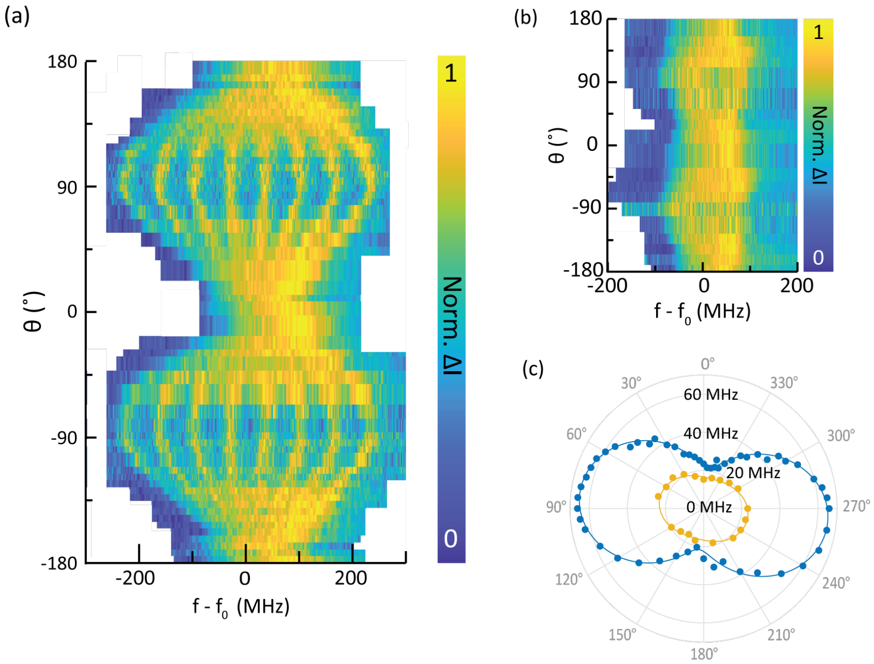

Figure 6.3: Hyperfine splitting in a vector magnetic field A. ESR measurements on hydrogenated ^{49}Ti adsorbed on a vertical bridge site. **B.** ESR measurements on hydrogenated ^{49}Ti adsorbed on a horizontal bridge site. **C.** data obtained by fitting each spectrum in **A.** (blue dots) and **B.** (yellow dots) with a sum of Fano functions, the error bars corresponding to the standard deviation of the fits are smaller than the markers' size. Fits to the experimental data (blue and yellow lines) are based on eqs. (6.2) and (6.3) (see section 6.7.1).

Next, we fit the data of fig. 6.3C to obtain the values of the hyperfine splitting, first along our field directions and, finally, along the lattice directions (see section 6.7.1). We here find $A_x = 68 \pm 4$ MHz, $A_y = 18 \pm 4$ MHz, and $A_z = 19 \pm 4$ MHz. The minima of the two data sets are each a measure of A_z; however, they are not exactly equal. We attribute the difference, which has been taken into account for the estimation of the error in A_z, to small variations in the local electric field surrounding the two atoms. Statistical variations of the g-factor of Ti atoms adsorbed on oxygen sites were indeed also observed and attributed to the same origin [14]. The errors for the in-plane components are dominated by the uncertainty concerning the tilt of the in-plane field with respect to the crystal lattice (see section 6.7.1).

6.5. DETERMINING THE GROUNDSTATE ORBITAL SHAPE

Once both the values of **g** and **A** are determined, we can investigate how these relate to the d1 ground state configuration of the Ti. The corresponding energy diagram for C_{2v} symmetry is displayed in fig. 6.4B [17]. The order of the excited states is arbitrarily chosen and bears no influence on the analysis. The ground state orbital is a superposition of $d_{x^2-y^2}$, d_{z^2}, and 4s orbitals, and our study revolves around determining the values of their respective weights c_1, c_2, and c_s, which satisfy the normalization equation $c_1^2 + c_2^2 + c_s^2 = 1$. The molecular coefficients α, β, γ_1, γ_2, and δ quantify the hybridization of the d levels with ligand orbitals, which we assume to be small - these coefficients are therefore expected to be close to 1.

In C_{2v} symmetry, the electronic configuration of the d levels causes anisotropy of **g** in the following way [17]:

$$\Delta g_x = g_x - g_0 = -2\alpha^2(c_1 + \sqrt{3}c_2)^2 K_2 \tag{6.4}$$

$$\Delta g_y = g_y - g_0 = -2\alpha^2(c_1 - \sqrt{3}c_2)^2 K_3 \tag{6.5}$$

$$\Delta g_z = g_z - g_0 = -8\alpha^2 c_1^2 K_1 \tag{6.6}$$

where $g_0 = 2.0023$, $K_1 = \beta^2\xi/\Delta(a_2)$, $K_2 = \gamma_2^2\xi/\Delta(b_2)$ and $K_3 = \gamma_1^2\xi/\Delta(b_1)$, with ξ being the spin-orbit coupling constant and $\Delta(a_2)[\Delta(b_2), \Delta(b_1)]$ the energy difference between the excited state $a_2[b_2, b_1]$ and ground state a_1 (see fig. 6.4B). As for the **A** vector we have:

$$\Delta A_i = A_i - A_{\text{mean}} = P\alpha^2 f_i(c_1, c_2, K_1, K_2, K_3) \tag{6.7}$$

where $i = x, y, z$, $A_{\text{mean}} = \frac{1}{3}(A_X + A_y + A_z)$, $P = g_0 g_N \mu_N \mu_B \langle r^{-3}\rangle$ (g_N: nuclear g-factor; μ_B: electron Bohr magneton; μ_N: nuclear Bohr magneton) scales with the radial extent of the electronic wave function via $\langle r^{-3}\rangle$, and f_i are functions whose full expressions can be found in section 6.7.2. These equations, along with the normalization condition for c_1, c_2, and c_s above, allow us to calculate the anisotropy of **g** and **A** for a given set of parameters (P, α, c_1, c_2, c_s) and therefore identify all sets of parameters that could, from a symmetry argument, describe our system. We find that more than one set of parameters can lead to the experimentally observed **g** and **A** (see section 6.7.2). Consequently, we employ a basic point charge model (section 6.7.3) that allows us to discriminate the different solutions by their Coulomb interaction. The lateral positions of the atoms are determined experimentally by atomic resolution STM images. The positions in the z-direction of the Ti and H atoms are estimated, but we ensure the robustness of the model against variations of these parameters.

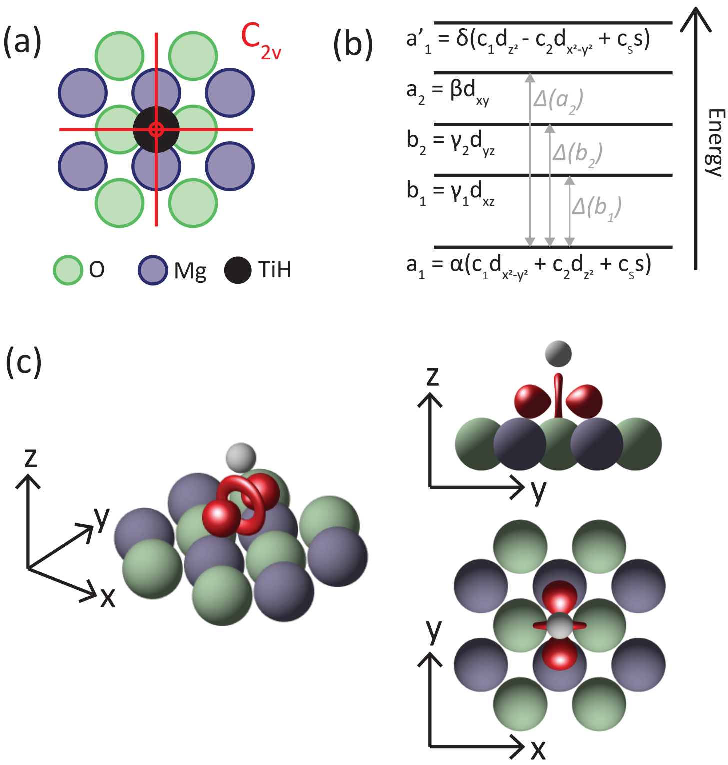

Figure 6.4: Determination of the ground state orbital. **A.** Ti is adsorbed on a bridge site with C_{2v} symmetry. **B.** Energy diagram for C_{2v} symmetry [17]. The order of the excited states is arbitrary and bears no consequence on the analysis. **C.** Isosurface of the ground state orbital (red) obtained for $c_s = 0$. Green spheres represent O atoms, blue spheres Mg atoms, and white sphere the H atom on top of Ti.

The state with the lowest Coulomb energy is shown in fig. 6.4C. It consists of a superposition of the $d_{x^2-y^2}$ (74%) and d_{z^2} (26%) orbitals in very good agreement with results obtained from DFT calculations [8]. This is quite remarkable because our electronic structure analysis is solely based on experimental data assisted by the symmetry group of the surface and a basic point charge model. However, our model cannot discriminate between different values of c_s which scales the admixture of the 4s orbital (see section 6.7.2). Nevertheless, we show that additional admixture of c_s merely influences the shape of the orbital by reducing the size of the central ring that points toward the neighboring O atoms (see section 6.7.4).

6.6. CONCLUSIONS

In summary, this work illustrates how an analysis of the anisotropic hyperfine interaction can be exploited to gain an in-depth knowledge about the shape of the ground state orbital. Crucial for this method is the addition of binding site information derived from STM, which we process in a basic point charge model. Because this protocol can be applied to other spin systems on surfaces in a straightforward manner, it paves the way to determine the spin ground states of atoms and molecules on surfaces and constitutes an independent method that more elaborate theoretical methods such as DFT can be benchmarked against.

While writing this manuscript, we became aware of a similar experiment performed in another group [18]. Overall, their results agree very well with those presented here: A strong anisotropy of the hyperfine splitting along the oxygen direction is also found in their experiment. In contrast to our work, they determine the shape of the ground state orbital via DFT, which allows to shed light onto the origin of anisotropic and isotropic contributions to the hyperfine interaction from a first-principles perspective.

6.7. APPENDIX

6.7.1. DETERMINATION OF THE HYPERFINE VALUES

Based on eq. (6.3) of the main text we fit the data of fig. 6.3C of the main text with the following function:

$$A = \frac{1}{g}\sqrt{\tilde{l} g_{v,h}^2 A_{v,h}^2 + n^2 g_z^2 A_z^2}. \tag{6.8}$$

Here $\tilde{l}$ and n are the cosine directions of the external field along the u and z axis respectively (see Figure S1b). As mentioned in the main text, we observe a rotation of the data in Fig.3c with respect to the magnet axes. We expect that although these errors could accumulate, macroscopic origins alone should be insufficient to explain the magnitude of the observed rotation. We also consider possible origins of a microscopic nature. Local variations in the electric field emerging from inhomogeneities of the substrate have been linked to variations in the g-factor of Ti atoms adsorbed on O-sites of the MgO lattice. The g-factor was found to be especially susceptible to changes in the in-plane direction of the electrostatic field leading to variations up to 15% [14]. This indicates that local charges play a large role in the crystalline environment the atom experiences. We account for this observed angle by an effective tilt between the magnet axes and the crystal field axes of the atom. More precisely, we consider an offset angle θ_0 between ($\mathbf{B}_\parallel$, $\mathbf{B}_\perp$) and ($\mathbf{u}$, $\mathbf{z}$) (see Figure S1c) and we therefore have

$$\tilde{l} = \cos\theta - \theta_0 \tag{6.9}$$

$$n = \sin\theta - \theta_0 \tag{6.10}$$

where $\tan\theta = \frac{B_\perp}{B_\parallel}$.

ϕ_0	12°	14°	16°
A_x	67 ± 2	68 ± 2	69 ± 2
A_y	20.5 ± 1.5	19 ± 2	17 ± 2

Table 6.1: Values for hyperfine splitting along the x and y axis when taking into account the error bars for ϕ_0.

The fits in fig. 6.3C of the main text are based on eqs. (6.8) to (6.10) and show a very good agreement with the experimental data. We obtain for the vertical bridge site $\theta_0 = -6.8° \pm 0.8°$, $A_v = 65.4 \pm 0.7 MHz$, $A_z = 21.7 \pm 1$ MHz and for the horizontal bridge site $\theta_0 = -15° \pm 5°$, $A_h = 23.6 \pm 0.8$ MHz, $A_z = 16.1 \pm 0.8$ MHz. Taking into account the presence of a tip-field, as determined in the previous section, does not improve the quality of the fits and leads to variations of less than 1 MHz of the fit coefficients. In particular, the presence of a tip field cannot account for the different values ofA_z. These are most likely due to local variations of the electric field for each atom as also observed in Ref. [14]. To obtain the values of the hyperfine vector along the lattice direction we again have to take into account the tilt of the in-plane field with respect to the crystal lattice. Using eq. (6.3) of the main text we fin the values shown in section 6.7.1. As one can see, the uncertainty concerning ϕ_0 dominates the error bars for A_x and A_y.

6.7.2. ANISOTROPY OF THE HYPERFINE SPLITTING IN C$_{2V}$ SYMMETRY

The anisotropy of the g and A vectors in C$_{2v}$ symmetry is given by eq. (6.7) of the main text where the functions f_x, f_y and f_z are defined as follows [17] (p.382) :

$$\begin{aligned} f_x = & -\frac{4}{3}(c_1+\sqrt{3}c_2)^2K_2+\frac{2}{3}[(c_1-\sqrt{3}c_2)^2K_3+4c_1^2K_1] \\ & +\frac{2}{7}(c_1^2-c_2^2-2\sqrt{3}c_1c_2)-\frac{4\sqrt{3}}{7}c_1c_2K_1 \\ & +\frac{\sqrt{3}}{7}(\sqrt{3}c_1+c_2)(c_1-\sqrt{3}c_2)K_3 \end{aligned} \tag{6.11}$$

$$\begin{aligned} f_y = & -\frac{4}{3}(c_1-\sqrt{3}c_2)^2K_3+\frac{2}{3}[(c_1+\sqrt{3}c_2)^2K_2+4c_1^2K_1] \\ & +\frac{2}{7}(c_1^2-c_2^2+2\sqrt{3}c_1c_2)+\frac{4\sqrt{3}}{7}c_1c_2K_1 \\ & +\frac{\sqrt{3}}{7}(\sqrt{3}c_1-c_2)(c_1+\sqrt{3}c_2)K_2 \end{aligned} \tag{6.12}$$

$$\begin{aligned} f_y = & -\frac{16}{3}c_1^2K_1+\frac{2}{3}[(c_1+\sqrt{3}c_2)^2K_2+(c_1-\sqrt{3}c_2)^2K_3] \\ & -\frac{4}{7}(c_1^2-c_2^2)-\frac{\sqrt{3}}{7}(\sqrt{3}c_1+c_2)(c_1-\sqrt{3}c_2)K_3 \\ & -\frac{\sqrt{3}}{7}(\sqrt{3}c_1-c_2)(c_1+\sqrt{3}c_2)K_2 \end{aligned} \tag{6.13}$$

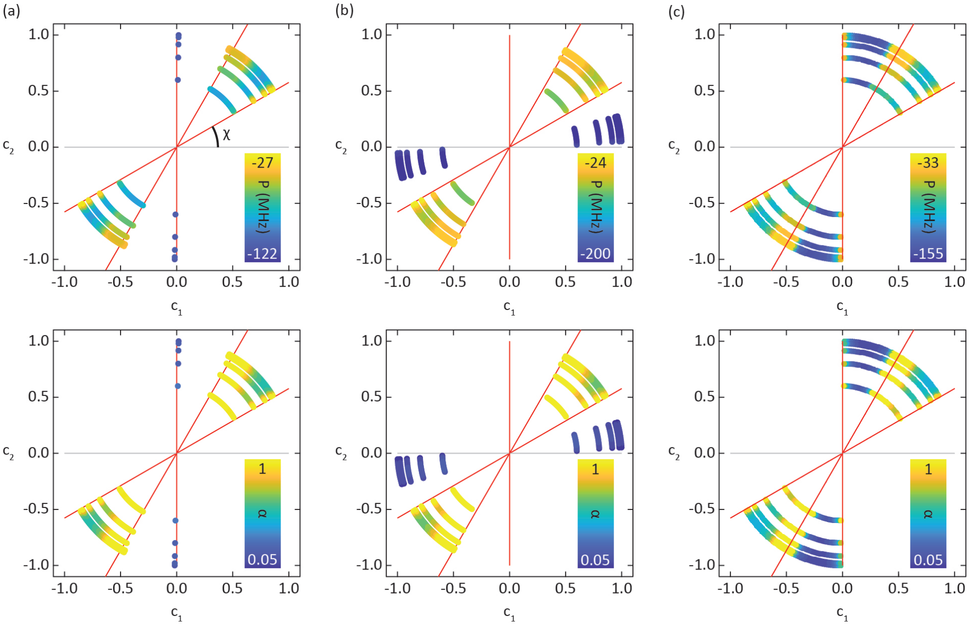

Figure 6.5: Sets of parameters $(P, \alpha, c_s, c_2, c_3)$ **that can give rise the observed anisotropy of the hyperfine splitting. A,B,C.** considers additionally variations of **g**. **A.** Values as reported in Ref. [2]: $(g_x, g_y, g_z) = (1.653, 1.917, 1.989)$. **B.** $(g_x, g_y, g_z) = (1.655, 1.898, 2.013)$. **C.** $(g_x, g_y, g_z) = (1.651, 1.936, 1.965)$.

We calculate the values of ΔA_x, ΔA_y and ΔA_z for parameter sets $(P,\ \alpha,\ c_1,\ c_2,\ c_3)$ where P spans $[0:-200]$ MHz, α spans $[0:1]$, c_s spans $[0:0.8]$ for which we only calculate sets in increments of 0.2. c_1 and c_2 are calculated via the normalization equation $c_1^2 + c_2^2 + c_3^2 = 1$. An angle χ is defined as $\tan\chi = \frac{c_2}{c_1}$, where χ spans $[0° : 360°]$. The calculation is performed in the following way: first the values of K_1, K_2, and K_3 are calculated via eqs. (6.4) to (6.6) of the main text and then ΔA_x,ΔA_y and ΔA_z are obtained from eqs. (6.7) and (6.11) to (6.13).

A parameter set is considered to be a valid solution if the values obtained for ΔA_x, ΔA_y and ΔA_z are within ±4 MHz of the experimental values. We plot in fig. 6.5A the data points that correspond to such valid solutions: each solution is represented with a point whose coordinates are (c_1, c_2) and the value of c_s determines the distance between this point and the origin (because of the normalization equation) - as a result the different concentric cycles correspond to the different values of the c_s parameter. The two remaining parameters, P and α, are represented by the color of the points in upper and lower graphs, respectively. We ensured the stability of our model against the uncertainty of **g** reported in literature and fig. 6.5B-C, shows two examples of the results of the calculations performed when considering a combination of extrema/minima of the components of **g** (we performed the calculation for all 8 possible combinations).

Ion	Δ electrons (no.)	x (Å)	y (Å)	z (Å)
H	1	0	0	1.8
O	2	-1.45	0	-1.6
O	2	1.45	0	-1.6
Mg	-2	0	-1.45	-1.6
Mg	-2	0	1.45	-1.6

Table 6.2: Point charge model used to identify the ground state orbital. Shown are the local charges as well as their position in the (x, y, z) coordinate system centered around the Ti atom (see fig. 6.1 of the main text).

As one can see, the value of c_s does not discriminate between different χ values but rather renormalizes the values of P and α. The two lines corresponding to $\chi = 30°$ and $\chi = 60°$ indicated by red lines are robust against variations of $\mathbf{g}$ and correspond to reasonable values for P and α. Indeed, α quantifies the hybridization of the d-levels with ligands orbitals and, since, we assume this effect to be minor, α should be close to 1. On the other hand, P scales with $\langle r^{-3}\rangle$ and large values of P correspond to orbitals with a very small spatial extent, from literature values [17] (Table 9.13 p.359) we expect $P \sim -78$ MHz for a Ti.

6.7.3. POINT CHARGE MODEL

To discriminate between the different solutions shown in fig. 6.5, we use additionally a point charge model defined from section 6.7.2. The point charge model allows to distinguish solutions that yield the correct hyperfine values (fig. 6.5), but are unlikely ground states, since the orbital charges are pointing in unfavorable directions of the surrounding crystal field. Each charge q_i at a position (x_i, y_i, z_i) yields a potential:

$$V_i = \frac{q_i}{\sqrt{(x-x_i)^2 + (y-y_i)^2 + (z-z_i)^2}}. \tag{6.14}$$

So that the total Coulomb energy for an electron in an orbital $|\psi\rangle$ is $E_c = -e\langle\psi|\sum_i V_i|\psi\rangle$. For each set of parameters that yields correct values for the anisotropy of the hyperfine vector we calculate the corresponding ground state orbital:

$$|\psi\rangle = c_1 \mathrm{d}_{x^2-y^2} + c_2 \mathrm{d}_{z^2} + c_s 4\mathrm{s} \tag{6.15}$$

where $\mathrm{d}_{x^2-y^2}$, $c_2\mathrm{d}_{z^2}$ and 4s are the spherical harmonics for which the radial parts verify:

$$R_{3,2} = \frac{4}{81\sqrt{6}(\frac{Z_{3\mathrm{d}}}{a_0})^3/2}\rho^2 e^{\frac{-\rho}{3}} \tag{6.16}$$

$$R_{4,0} = \frac{1}{96} Z_{4\mathrm{s}}^{3/2}[24 - \frac{26\rho}{2} + 12(\frac{\rho}{2})^2 - \frac{\rho}{2})^3]e^{-\frac{\rho}{4}} \tag{6.17}$$

where $\rho = Zr/a_0$, with a_0 being the Bohr radius and $Z_{3\mathrm{d}}(Z_{4\mathrm{s}})$ the effective nuclear charge for the 3d(4s) shell.

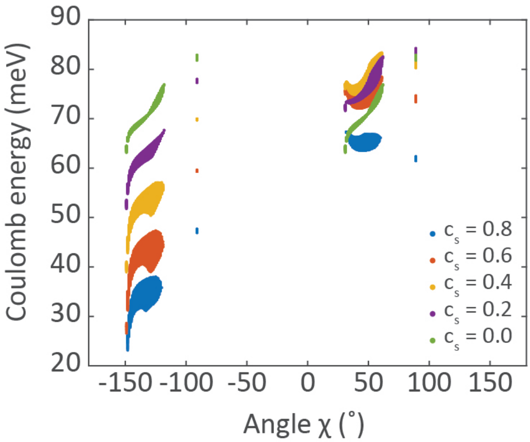

Figure 6.6: Coulomb energy for the different sets of parameters that correctly describe the hyperfine anisotropy.

For the angular parts we have:

$$Y_{x^2-y^2} = \frac{\sqrt{15}x^2 - y^2}{4\sqrt{\pi}r^2} \tag{6.18}$$

$$Y_{z^2} = \frac{\sqrt{5}3z^2 - r^2}{4\sqrt{\pi}r^2} \tag{6.19}$$

$$Y_{4\mathrm{s}} = \frac{1}{4\sqrt{\pi}} \tag{6.20}$$

Furthermore, we have (see main text):

$$P = g_0 g_\mathrm{N} \mu_\mathrm{N} \mu_\mathrm{B} \langle r^{-3} \rangle \tag{6.21}$$

Neglecting for simplicity any contribution of c_s, the radial extent of the orbital can be calculated from the radial wave-function for d-orbitals (see eq. (6.16)):

$$\langle r^{-3} \rangle = \int_0^{\mathrm{inf}} [R_{3,2}(r)]^2 r^{-3} r^2 dr \tag{6.22}$$

And we obtain:

$$\langle r^{-3} \rangle = \frac{z^3}{81 a_0^3} \tag{6.23}$$

Therefore, for each set of solutions determined after the previous step, we calculate the value of $Z_{3\mathrm{d}}$ using the value of the P parameter and eqs. (6.21) and (6.23). The effective nuclear charge for the s orbital is then adjusted so that the ratio $Z_{3\mathrm{d}}/Z_{4\mathrm{s}}$ equals the one given in literature [19].

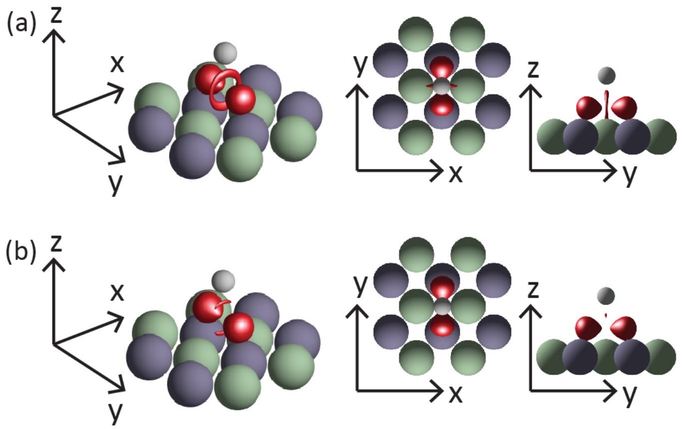

Figure 6.7: Influence of c_s on the ground state orbital. A. Solution obtained for $c_s = 0.2$. **B.** Solution obtained for $c_s = 0.4$.

The calculation is performed using a grid in the (x, y, z) space that spans $[-4a_0 : 4a_0]$ in each direction and with a spacing of $0.1a_0$ between points. We ensure robustness of the results by varying the position of the Ti atom with respect to the crystal lattice along the z-direction in the range of 20%. The position of the Mg and O atoms are determined experimentally by atomic resolution images and the one of the H atom is set according to [20].

In fig. 6.6 we show the Coulomb energy calculated for the sets of parameters shown in fig. 6.6A. Each color represents a different value of c_s and the multiplicity of points for given χ and c_s values corresponds to the multiple sets of candidates that contains these values. As one can see, decreasing c_s leads to a systematic decrease in the Coulomb energy. While this can be easily explained by the smaller radial extent of the 4s orbital with respect to the 3d orbitals, the calculation suggests that the minimal solution corresponds to an electron only localized in the 4s orbital which is unrealistic. The point charge model therefore does not allow to determine with certainty the value of c_s. However, it allows us to clearly identify the ground state orbital for each value of c_s. As we consistently find a minimum at $\chi = -150°$ for every value of c_s we conclude that the relative mixture between the d-orbitals is not affected by the addition of c_s.

6.7.4. INFLUENCE OF c_s ON THE GROUND STATE ORBITAL

In the main text, we show the solution obtained for $c_s = 0$. In fig. 6.7, we show the optimal solutions for $c_s = 0.2$ (A), which is most likely an upper boundary for the admixture of the 4s orbital, as well as for $c_s = 0.4$ (B), which is unrealistic but help us better capture the influence of the parameter. The admixture of the ss orbital influences only marginally the shape of the orbital: it mostly reduces the size of the central ring that points towards the neighboring O atoms. We ensured that these results are robust against variations of the g vector within the error bars given in Ref. [12].

REFERENCES

[1] L. Farinacci†, **L. M. Veldman**†, P. Willke, and S. Otte. “Experimental determination of a single atom ground state orbital through hyperfine anisotropy”. In: *Nano Letters* 22.21 (2022), pp. 8470–8474.

[2] A. Abragam and B. Bleaney. *Electron paramagnetic resonance of transition ions*. Clarendon P., 1970.

[3] P. Neumann, J. Beck, M. Steiner, F. Rempp, H. Fedder, P. R. Hemmer, J. Wrachtrup, and F. Jelezko. “Single-shot readout of a single nuclear spin”. In: *science* 329.5991 (2010), pp. 542–544.

[4] R. Vincent, S. Klyatskaya, M. Ruben, W. Wernsdorfer, and F. Balestro. “Electronic read-out of a single nuclear spin using a molecular spin transistor”. In: *Nature* 488.7411 (2012), pp. 357–360.

[5] J. J. Pla, K. Y. Tan, J. P. Dehollain, W. H. Lim, J. J. Morton, D. N. Jamieson, A. S. Dzurak, and A. Morello. “A single-atom electron spin qubit in silicon”. In: *Nature* 489.7417 (2012), pp. 541–545.

[6] B. E. Kane. “A silicon-based nuclear spin quantum computer”. In: *nature* 393.6681 (1998), pp. 133–137.

[7] S. Baumann, W. Paul, T. Choi, C. P. Lutz, A. Ardavan, and A. J. Heinrich. “Electron paramagnetic resonance of individual atoms on a surface”. In: *Science* 350.6259 (2015), pp. 417–420.

[8] P. Willke, Y. Bae, K. Yang, J. L. Lado, A. Ferrón, T. Choi, A. Ardavan, J. Fernández-Rossier, A. J. Heinrich, and C. P. Lutz. “Hyperfine interaction of individual atoms on a surface”. In: *Science* 362.6412 (2018), pp. 336–339.

[9] K. Yang, P. Willke, Y. Bae, A. Ferrón, J. L. Lado, A. Ardavan, J. Fernández-Rossier, A. J. Heinrich, and C. P. Lutz. “Electrically controlled nuclear polarization of individual atoms”. In: *Nature nanotechnology* 13.12 (2018), pp. 1120–1125.

[10] S. Kovarik, R. Robles, R. Schlitz, T. S. Seifert, N. Lorente, P. Gambardella, and S. Stepanow. “Electron paramagnetic resonance of alkali metal atoms and dimers on ultrathin MgO”. In: *Nano Letters* 22.10 (2022), pp. 4176–4181.

[11] K. Yang, Y. Bae, W. Paul, F. D. Natterer, P. Willke, J. L. Lado, A. Ferrón, T. Choi, J. Fernández-Rossier, A. J. Heinrich, *et al.* “Engineering the eigenstates of coupled spin-1/2 atoms on a surface”. In: *Physical Review Letters* 119.22 (2017), p. 227206.

[12] J. Kim, W.-j. Jang, T. H. Bui, D.-J. Choi, C. Wolf, F. Delgado, Y. Chen, D. Krylov, S. Lee, S. Yoon, *et al.* “Spin resonance amplitude and frequency of a single atom on a surface in a vector magnetic field”. In: *Physical Review B* 104.17 (2021), p. 174408.

[13] **L. M. Veldman**, L. Farinacci, R. Rejali, R. Broekhoven, J. Gobeil, D. Coffey, M. Ternes, and A. F. Otte. “Free coherent evolution of a coupled atomic spin system initialized by electron scattering”. In: *Science* 372.6545 (2021), pp. 964–968.

[14] M. Steinbrecher, W. M. Van Weerdenburg, E. F. Walraven, N. P. Van Mullekom, J. W. Gerritsen, F. D. Natterer, D. I. Badrtdinov, A. N. Rudenko, V. V. Mazurenko, M. I. Katsnelson, *et al.* “Quantifying the interplay between fine structure and geometry of an individual molecule on a surface”. In: *Physical Review B* 103.15 (2021), p. 155405.

[15] H. Rinneberg and J. Weil. “EPR Studies of Ti3+–H+ Centers in X-Irradiated α-Quartz”. In: *The Journal of Chemical Physics* 56.5 (1972), pp. 2019–2028.

[16] M. Yulikov, M. Sterrer, M. Heyde, H.-P. Rust, T. Risse, H.-J. Freund, G. Pacchioni, and A. Scagnelli. “Binding of single gold atoms on thin MgO (001) films”. In: *Physical review letters* 96.14 (2006), p. 146804.

[17] F. Mabbs and D. Collison. “Electron paramagnetic resonance of d transition metal compounds”. In: *Studies in Inorganic Chemistry* 16 (1992), pp. 1–1306.

[18] J. Kim, K. Noh, Y. Chen, F. Donati, A. J. Heinrich, C. Wolf, and Y. Bae. “Anisotropic hyperfine interaction of surface-adsorbed single atoms”. In: *Nano Letters* 22.23 (2022), pp. 9766–9772.

[19] E. Clementi and D.-L. Raimondi. “Atomic screening constants from SCF functions”. In: *The Journal of Chemical Physics* 38.11 (1963), pp. 2686–2689.

[20] O. Launila and B. Lindgren. “Spectroscopy of TiH: Rotational analysis of the 4Γ→ X 4Φ (0, 0) band at 530 nm”. In: *The Journal of chemical physics* 104.17 (1996), pp. 6418–6422.

7

COHERENT ELECTRON-NUCLEUS SPIN DYNAMICS IN A SINGLE ATOM

> *Truth is born in arguments*
>
> Stalker - Andrei Tarkovsky

The nuclear spin, being much more isolated from the environment than its electronic counterpart, enables quantum experiments with prolonged coherence times and serves as a viable pathway to study the sophisticated dynamics within an atom. These qualities have been demonstrated in a variety of qubit architectures based on individual nuclear spins [2–4], albeit with limited control over the direct environment of the nuclei. As a contrasting approach, the combination of electron spin resonance (ESR) and scanning tunnelling microscopy (STM) [5] provides a bottom-up platform to study the fundamental properties of nuclear spins of single atoms on a surface [6, 7]. However, access to nuclear spin dynamics, as was recently demonstrated for electron spins [8, 9], remained a challenge. Here, we present an experiment resolving the nanosecond coherent dynamics of a hyperfine driven flip-flop interaction between the spin of an individual nucleus and that of an orbiting electron. We use the unique local controllability of the magnetic field emanating from the STM probe tip [10] to bring the electron and nuclear spins in tune, as evidenced by an avoided level crossing in ESR-STM. Subsequently, we polarize both spins through scattering of tunnelling electrons and measure the resulting free evolution of the coupled spin system using a DC pump-probe scheme. The latter reveals a complex pattern of multiple interfering coherent oscillations, providing unique insight into the atom's intricate hyperfine physics. The ability to trace the coherent hyperfine dynamics with atomic scale structural control adds a new degree of freedom to the study of on-surface spins, offering a pathway towards dynamic quantum simulation of low-dimensional magnonics.

The results in this chapter were conceived in close collaboration with E. Stolte, M. Canavan, R. Broekhoven, P. Willke, L. Farinacci and S. Otte.

Parts of this chapter are in preparation for peer reviewed publication and are available as a preprint [1].

7.1. INTRODUCTION

Control over nuclear spins has shown great promise as building blocks for quantum information in molecular spin qubits [3, 11], NV centers [2, 12], and donors in silicon [4]. They also are an excellent resource for quantum simulation [13], magnetic sensing [14, 15] and spintronics [16] and are potentially scalable via engineered molecular and atomic networks [17, 18]. Their key advantage arises from the longer coherence times compared to their electron spin counterpart [19], though the intricacies of the decoherence channel depend on the exact interaction with the environment and may be difficult to describe in detail. Scanning tunneling microscopy (STM) constitutes an excellent means of investigation here, since it not only permits to address individual electron spin states in electron spin resonance (ESR) experiments with sub-nanometer resolution [5, 20], but also allows for an atomically precise control of their environment [21, 22]. Up to now, interactions involving the nuclear spin could be measured indirectly by probing the hyperfine coupling in ESR-STM between the nucleus and the surrounding electrons [6]. In addition, the nuclear spin of individual copper atoms could be polarized via spin pumping induced by the spin-polarized tunneling current [7]. However, accessing the coherent dynamics involving the nucleus remained challenging, due to its weak coupling to the tunneling electrons.

In this work, we show the free, coherent evolution between the nuclear spin and the unpaired electron spin in a single hydrogenated titanium atom. By using ESR-STM and by fine-tuning the electronic Zeeman energy, we identify a parameter space where electronic and nuclear spin states hybridize. In a second step, we probe the free coherent evolution of the coupled system by electric DC pump-probe experiments. Here, we reveal an emerging beating pattern, that originates from multiple quantum oscillations with different frequencies at the points of hybridization.

7.2. SYSTEM OF STUDY

We use a commercial low-temperature STM equipped with high frequency cabling to be able to send both RF signals and nanosecond DC pulses down to the tip. The sample system consists of Ti atoms deposited on bilayer MgO islands grown on Ag(100) (fig. 7.1A), that become hydrogenated by residual hydrogen. For all measurements, we use spin-polarized tips that are created by picking up co-deposited Fe atoms onto the tip apex. We study hydrogenated Ti adsorbed onto the oxygen sites of MgO which exhibit an effective electron spin $S = 1/2$ [23] and an anisotropic g-factor $\mathbf{g}$ [24]. Throughout this work, we focus on ^{47}Ti isotopes, which carry a nuclear spin $I = 5/2$. Along the principle axes of the crystal field, the system is described by the following Hamiltonian:

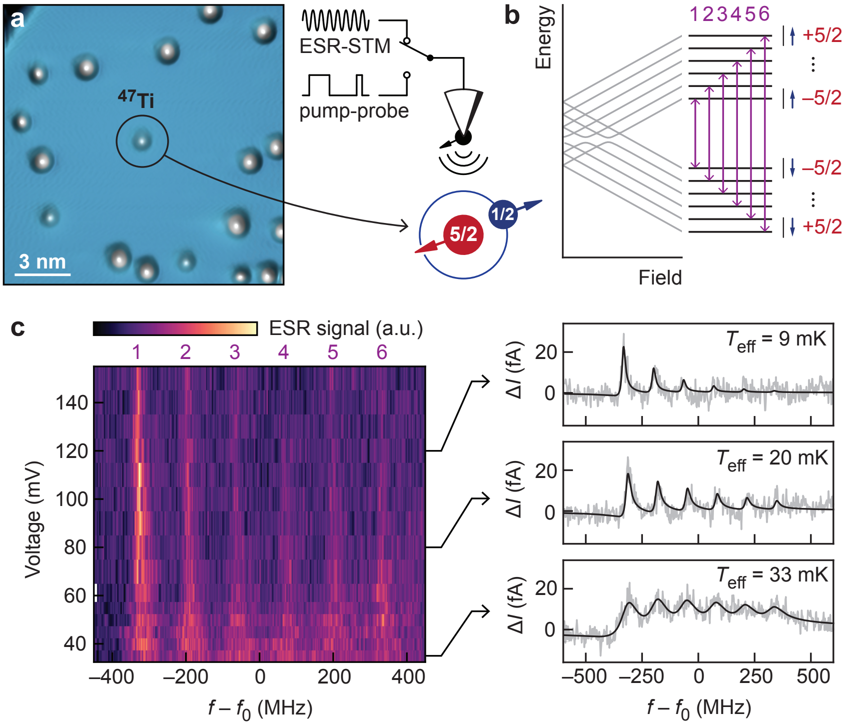

Figure 7.1: Single atom nuclear polarization. A. STM topography of the single ^{47}TiH studied in this work. A schematic drawing shows the magnetic STM tip above the electron spin (blue) and nuclear spin (red) of the single atom. **B.** Energy diagram of the spin states of a single ^{47}TiH. In the high field regime, the eigenstates resemble Zeeman product states. ESR transitions (green arrows) can be driven between states with equal nuclear spin. **C.** ESR-STM measurements at different applied DC bias ($T = 1.5$ K, $B_{\mathrm{ext}} = 1.5$ T, $V_{\mathrm{RF}} = 25$ mV, $I_{\mathrm{set}} = 2.5$ pA, $f_0 = 11.5 - 12.56$ GHz). Line traces at 35 mV, 80 mV and 120 mV are shown with fits using six Fano lineshapes scaled by the Boltzmann factor in order to extract an effective temperature.

$$\hat{H} = \sum_{i=x,y,z} (\mu_{\mathrm{B}} g_i (B_{\mathrm{ext},i} + B_{\mathrm{tip},i})\hat{S}_i + A_i \hat{S}_i \hat{I}_i + Q_i \hat{I}_i^2). \tag{7.1}$$

With the anisotropic hyperfine and quadrupole contributions $\mathbf{A} = [10, 10, 130]$ MHz and $\mathbf{Q} = [1.5, 1.5, -3]$ MHz [6], respectively (see section 7.7.1). Moreover, the first term describes the Zeeman energy of the electron spin with contributions from both the external $\mathbf{B}_{\mathrm{ext}}$ and the tip-induced magnetic field $\mathbf{B}_{\mathrm{tip}}$. We neglect the effect of either of these fields on the nuclear spin, since their contributions are small compared to the other terms.

7.3. STATE INITIALIZATION VIA SPIN PUMPING

We start our investigation by applying a magnetic field of 1.5 T, which is large compared to the hyperfine interaction, in order to drive ESR transitions between the individual spin states of a ^{47}Ti atom that has been isolated from neighboring spins using atom manipulation (fig. 7.1B). Similar to measurements of Ti on a bridge binding site of MgO [25, 26], we find a large anisotropy in the hyperfine coupling ranging from 10 MHz in-plane to 130 MHz out-of-plane (see section 7.7.1). Since we later aim for a regime in which the hyperfine interaction competes with the Zeeman splitting of the electron, the experiments are performed with an out-of-plane magnetic field.

For certain magnetic tips with sufficient spin-polarization, we observe that the hyperfine-split ESR peaks have different intensities, which indicates a strong polarization of the nuclear spin. Such nuclear polarization has been observed for Cu atoms on MgO [7] and was modeled by taking into account inelastic spin scattering events between the tunneling electrons and electron spin. In our case, we find that the polarization is strongly dependent on the applied bias voltage while measuring at constant current (fig. 7.1C). We believe that this may be due to the bias-dependent efficiency of the spin scattering channels involved, but a more complex mechanism involving the Ti orbital excitation [24] or Pauli spin blockade [27] may be at play. We find that the effective temperature of the nuclear spin population drops below 10 mK at voltages larger than 100 mV, more than two orders of magnitude lower than the actual experimental temperature of 1.5 K.

7.4. TUNING ELECTRON-NUCLEAR SPIN ENTANGLEMENT

This highly efficient spin pumping allows us to overcome a main limitation of ESR-STM: so far, the frequency ranges accessible for a given temperature were limited to the spin contrast set by the Boltzmann distribution. Here, owing to the nuclear polarization, we can investigate a much lower frequency regime, in which the level of entanglement between the electron and nuclear spins can be tuned. In fig. 7.2A, we show the different contributions to the energy diagram of a ^{47}Ti in a low-field regime. When the total electronic Zeeman energy – due to the external and tip magnetic field – is comparable to the hyperfine splitting, multiple avoided level crossings occur in the spectrum (see dashed lines in fig. 7.2A). The multiplicity of these avoided crossings arises from the anisotropy of the hyperfine coupling and a small misalignment of the tip field with the external field. At each of these crossings, the eigenstates form different superpositions of the electronic and nuclear spin states.

We identify these tuning points in our experiment by performing ESR measurements in the low field regime using an external field of merely 20 mT (fig. 7.2B). Here, in order to fine-tune the coupled spin system, we vary the tip-induced magnetic field, which we adjust by the tunnel conductance of the junction. At large tip fields ($G > 20$ pS) multiple ESR peaks are visible in addition to several very sharp (~ 33 MHz) NMR type resonances around 60 MHz. The uneven splitting of the NMR type resonances is here caused by the quadrupole interaction [6]. Below $G \approx 20$ pS, the ESR and NMR transitions start to mix

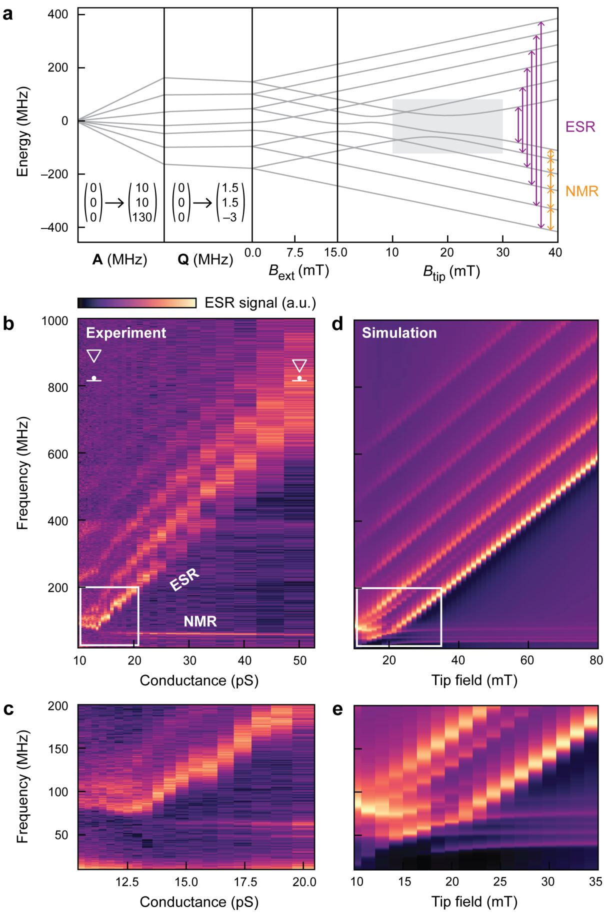

Figure 7.2: ESR and NMR-type measurements in the low-field regime. A. Energy diagram of the atomic eigenstates as a function of hyperfine coupling, quadrupole moment, external and tip-induced magnetic field. **B.** ESR-STM measurements showing ESR and NMR-type transitions (T = 400 mK, B_{ext} = 20 mT, V_{RF} = 40 mV, I_{set} = 2 pA). The bottom close-up is a separate dataset showing the splitting of the NMR transitions and a curve upwards of the bottom ESR transition signaling the avoided level crossing. **C.** Simulations of the ESR-STM measurements (see chapter 2 for details).

and overlap, accompanied by a redistribution of their intensities as shown in the bottom panel of fig. 7.2B. This is consistent with the presence of avoided level crossings in the energy levels, as expected from fig. 7.2A and modelled in fig. 7.2C. For the simulation we model the tip field to be oriented at an 8 degree angle with respect to the out-of-plane external field and scale the intensities of NMR and ESR transitions separately (see chapter 2). The small in-plane component of the tip magnetic field gives rise to an additional avoided level crossing in fig. 7.2A. The two avoided crossings correspond to mixing of different combinations of states: the first one consists of a superposition of both electron and nuclear spin states while the second one, driven by the in-plane field, involves a superposition of the electron spin states only.

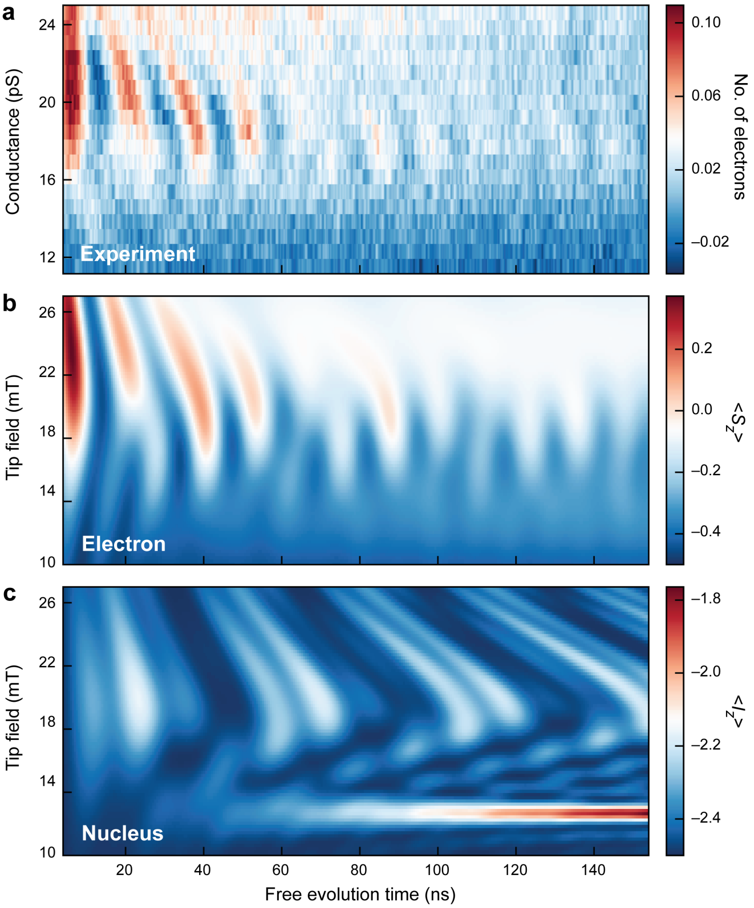

Figure 7.3: Free evolution measurements and Lindblad simulations. **A.** Pump-probe data for different tip-atom distances set by the junction conductance ($V_{\text{set}} = 130$ mV, $T = 400$ mK, $B_{\textbf{ext}} = 15$ mT, for details on the pulse scheme, see section 7.7.2). **B.** Lindblad simulation of the free time evolution of the electron spin when initialized to $\left|\downarrow, -\frac{5}{2}\right\rangle$. **C.** Corresponding Lindblad simulation of the free time evolution of the nuclear spin. The calculations also show the onset of an additional oscillation in the nuclear spin at around 13 mT. However, since the period is an order of magnitude longer than the coherence time of the electron spin, it is not visible in our measurements.

7.5. PROBING COHERENT SPIN DYNAMICS

Having identified the appropriate tip-atom distances in order to induce superposition states, we perform DC pump-probe experiments to explore the coupled spin dynamics. We use a two-pulse sequence to initialize both electron and nucleus spins to the state $\left|\downarrow, -\frac{5}{2}\right\rangle$ via inelastic scattering (See fig. 7.3A and section 7.7.2). Then, after a free, varied time evolution, the final state of the system is probed by a 5 ns probe pulse.

The spin dynamics (fig. 7.3A) following this pulse sequence depend on the tip magnetic field: when the STM tip is close (i.e., at large tip field, fig. 7.3A, top) we observe fast, low-amplitude oscillations that become slower and larger as the tip is retracted. This is the expected behavior when the system moves through an avoided crossing point [9]. However, around 17 pS (fig. 7.3A, middle) a beating appears due to interference with a second oscillation. Upon further retraction of the tip, no spin dynamics are detected anymore (fig. 7.3A, bottom). fig. 7.3B and fig. 7.3C show the evolution of the S_z and I_z expectation values for the electron and the nuclear spin, respectively, calculated using Lindblad time evolution starting from the $\left|\downarrow, -\frac{5}{2}\right\rangle$ state. We find excellent agreement between the data and calculations, with in particular a beating pattern that arises when the electron and nucleus states are entangled. While the electron shows an interference pattern, the nuclear spin is dominated by a ~ 40 ns oscillation.

To understand the origin of these different oscillations, we focus on the region of interest marked in the energy spectrum of fig. 7.2A: In fig. 7.4A, we identify a combination of three eigenstates that form a pair of avoided level crossings, which we assign to the observed dynamics. When we tune the tip field to the second avoided level crossing (fig. 7.4C, 24 mT) we find that the population is evenly split between state $|5\rangle$ and $|6\rangle$ corresponding to the lowest energy ESR resonance observed in fig. 7.2. Here, the nucleus remains unaffected and only the electron spin forms a superposition between up and down: $\left|\uparrow \pm \downarrow, -\frac{5}{2}\right\rangle$. Accordingly, we can fit in fig. 7.4B a trace from the pump-probe data with a single sinusoid obtaining a frequency of roughly 75 MHz, matching the expected energy splitting between $|5\rangle$ and $|6\rangle$ at a tip field of 23.7 mT. The transition between states $|4\rangle$ and $|5\rangle$, on the other hand, corresponds to a flip-flop between the electron and nuclear spin. When these states hybridize they form the superposition state $\left|\uparrow, -\frac{5}{2}\right\rangle \pm \left|\downarrow, -\frac{3}{2}\right\rangle$. Thus, when the tip field is right in middle of the two tuning points (fig. 7.4B, 20.5 mT) the dynamics are expected to be a mixture between the electron oscillation discussed above and an additional flip-flop dynamic between electron and nucleus. In fig. 7.4B, we observe this as a clear interference pattern in the time evolution, which we fit using three sinusoids with frequencies of 65 MHz, 20 MHz and their sum. This matches the calculated energy splitting at this tip field. Correspondingly, we can attribute the 65 MHz oscillation to a Larmor precession of the electron spin due to the in-plane component of the tip field while the 20 MHz oscillation is a flip-flop between the electron and the nucleus driven by the hyperfine interaction.

The reduced coupling of the nuclear spin to the environment is expected to result in an enhanced coherence time when the nuclear spin is involved, compared to the dynamics of only the electron spin [15, 28, 29]. Indeed, the data shown in fig. 7.4B still shows observable dynamics up to 120 ns, whereas the oscillation in fig. 7.4C has decayed already after 80 ns. We point out, however, that the increased coherence time may also in part result from a decreased sensitivity to magnetic tip field due to the energy levels being more parallel at 21 mT compared to 23 mT (fig. 7.4A), akin to a clock-transition [30, 31].

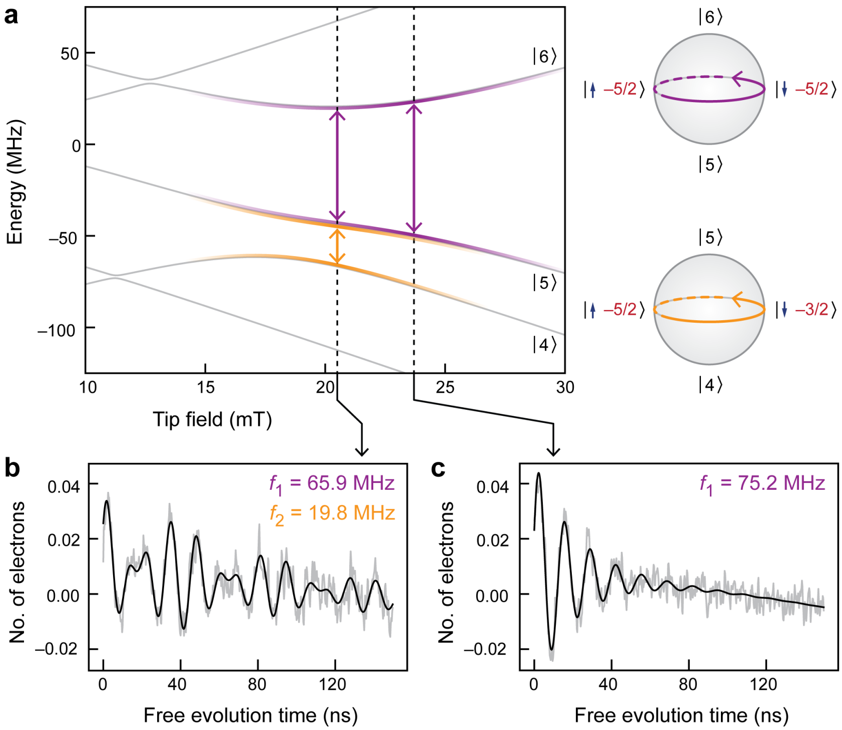

Figure 7.4: Origin of the beating pattern. A. Zoom in on the relevant avoided level crossings of fig. 7.2A. The Bloch spheres illustrate the dominating dynamics arising from the superpositions of the corresponding states. **B.** A fit to a line trace from the pump-probe data from fig. 7.3A showing a beating pattern. The pattern arises from two dominating frequencies and their sum frequency. **C.** A fit to a line trace from the pump-probe data from fig. 7.3A showing a single frequency oscillation.

7.6. CONCLUSIONS

Developing single atom quantum information processing requires thorough understanding of the underlying electron and nuclear spin dynamics. This demands initialization, tuning and readout tailored on the atomic length scale. Using pump-probe spectroscopy, we here revealed the collective coherent dynamics of the internal spin dynamics inside a single atom. The magnetized STM tip functioned in this work as a control knob to locally tune the nature of these dynamics providing excellent functional flexibility. This technique has the potential to be extended to any on-surface atomic or molecular spin system, yielding a great variety of phenomena to explore in the future. Moreover, the prospect of STM for engineering bottom-up atomic designer assemblies can provide an integral atomic-scale understanding into the fundamentals of complex coherent spin dynamics.

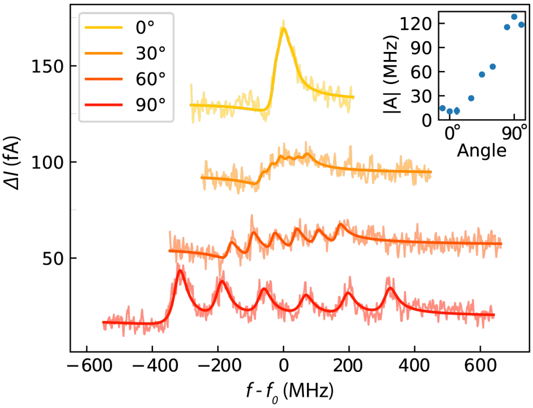

Figure 7.5: Hyperfine anisotropy measurements. ESR-STM measurements on ^{47}Ti at angles varying from in-plane (0°) to out-of-plane (90°) with fits of 6 equidistant Fano functions. Traces are offset for clarity. Inset top right: magnitude of hyperfine splitting A as a result of the fitting for the entire dataset. All fitting parameters, except the hyperfine splitting magnitude and peak amplitude, were fixed by an identical data set taken on a ^{48}Ti without any nuclear spin. Experimental parameters: $I_{\text{setpoint}} = 3$ pA, $V_{\text{setpoint}} = 60$ mV, $V_{\text{RF}} = 25$ mV, $T = 1.5$ K, $|B_{\text{ext}}| = 1.5 - 0.5$ T.

7.7. APPENDIX

7.7.1. HYPERFINE ANISOTROPY

In order to correctly calculate the eigenenergies of the Hamiltonian presented in equation 1.1 in the main text, we need to determine the hyperfine vector **A**. Due to the C_{4v} symmetry of the crystal structure of the oxygen binding site, we assume the two in-plane directions A_x and A_y to be equal. Therefore, we only need two measurements to characterize **A** fully: the hyperfine splitting in-plane and out-of-plane. Consequently, we swept the angle of the external field from in-plane to out-of-plane while measuring the magnitude of the hyperfine splitting in a ^{47}Ti atom. Results are shown in fig. 7.5: we find an in-plane splitting of 10 MHz, in accordance with previous measurements [6] and an out-of-plane splitting of 130 MHz.

7.7.2. PULSE SEQUENCE

The pump-probe measurements were done in constant-height mode after tracking the center of the atom for ~ 1 hour and while linearly compensating for drift due to piezo creep. For the pump-probe data shown in the main text the tip was placed ~ 300 fm away from the center in order to minimize in-plane field component of the tip field.

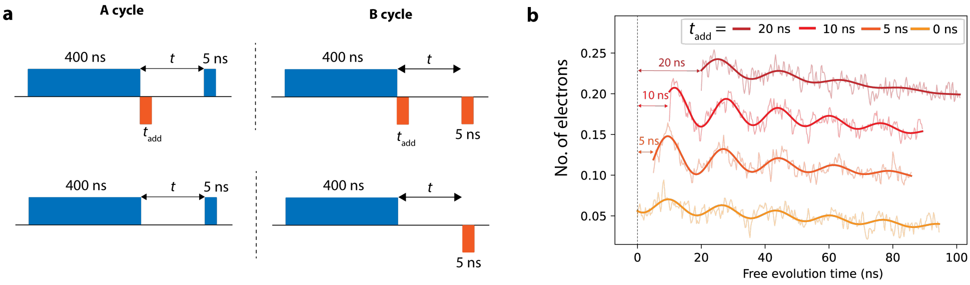

Figure 7.6: Pump-Probe pulse scheme. A. Schematic picture of the pulse schemes in the lock-in A and B cycle. A additional second pump pulse is used (top) to increase signal intensity. Displayed widths of the pulses are the values that were used for the data in the main text. **B.** Signal intensity comparison between the pulse trains with different second pump pulses (setpoint: 4 pA, 130 mV). The signal is phase shifted by the length of the second pump pulse. For $t_{\mathrm{add}} = 5, 10$ ns we find an increase in signal amplitude.

To pump the electron and nuclear spin we start the pulse train with a 400 ns positive bias pulse. We then add an extra 5 ns negative pump pulse that we empirically found helps to increase the signal intensity. We hypothesize that the addition of this pulse brings the atomic electron spin in a superposition state close to which maximizes the amplitude of the resulting spin dynamics. In fig. 7.6 pulse sequences with and without this extra pulse are compared. To increase the signal detected by the lock-in amplifier we switch the polarity of the 5 ns probe pulse in the B-cycle [32]. All pulses went through a 5 GHz low pass filter before being sent to the STM to minimize artefacts. The pulses were calibrated to have an amplitude of 110 mV at the tip sample junction.

7.7.3. NUCLEAR SPIN PUMPING CURRENT DEPENDENCE

In fig. 5.1 we showed that we could pump the spin state of the nuclear spin of a ^{47}Ti bound to an oxygen site of the underlying MgO. We found that the amount of nuclear polarization we could achieve is largely dependent on the applied DC bias during the experiment. In section 7.3 we briefly discussed the possible origins of this effect and noted that it is distinctly different from the spin pumping mechanism described for Cu in [7]. There, the amount of nuclear polarization scales with the spin polarized current interacting with the orbiting electron spin and is captured in a rate equation model [33].

In fig. 7.7 we show the current dependence of the nuclear spin pumping, similar to the bias dependence shown in fig. 7.1C. We find a clear inverse relation: the larger the current, the smaller the resulting nuclear polarization. This again points towards a different mechanism than described by [7].

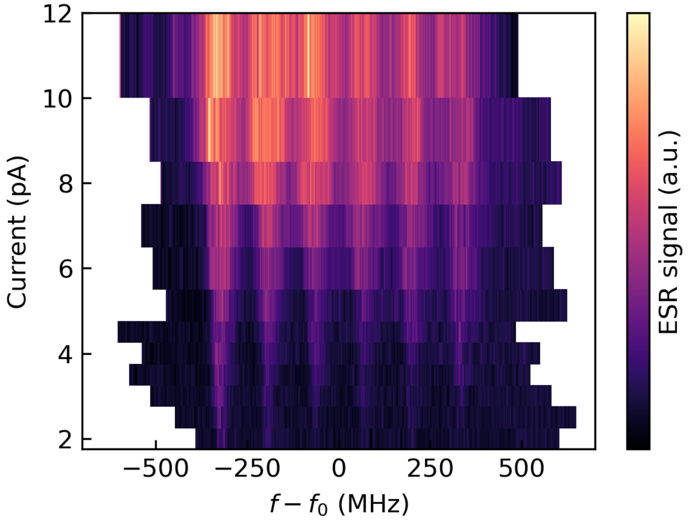

Figure 7.7: Current dependence of nuclear spin pumping. ESR measurements on a ^{47}Ti on the O binding site as function of setpoint current ($T = 1.5$ K, $B_{\text{ext}} = 1.5$ T, $V_{\text{RF}} = 25$ mV, $V_{\text{set}} = 100$ mV).

7

7.7.4. TIP DEPENDENCE

To show the influence of the microtip, we perform ESR-STM measurements with a different microtip on the same ^{47}Ti atom bound on the oxygen site. The results are shown in fig. 7.8 for two different B_{ext} values. Compared to the data taken with the tip of the main text (fig. 7.2) we find a number of differences. First, at both external field values, the lowest two ESR resonances are stuck closer together and are separated more when the tip is further away ($G < 40$ pS). Second, the splitting between NMR resonances are so small that the are observed as a single peak that shifts in energy with applied tip field.

We get a good agreement in the simulations by adjusting just a single parameter compared to the simulations shown in fig. 7.2: the angle of the magnetic tip field compared to the external field. While we found a very small angle of 8° for the tip used in fig. 7.2, we find an angle of ~ 80° for the tip used in fig. 7.8. This means that when we approach the atom with this last tip, we effectively add more in-plane field than we do out-of-plane field. This results in qualitatively different behaviour of the resonances due to the anisotropy of the hyperfine coupling. Since $A = 10$ MHz in-plane, the splitting between ESR resonances becomes smaller (just like in fig. 7.5) with increasing tip field and the NMR resonances (which are a direct measurement of this energy difference) shift to lower frequency.

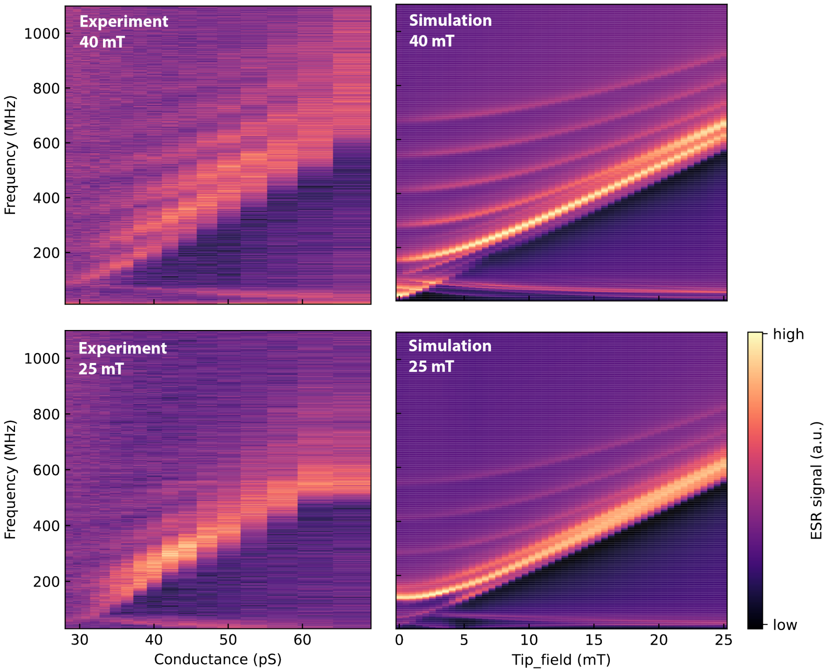

Figure 7.8: ESR-STM data taken with a different microtip on the same ^{47}Ti atom compared to the data presented in the main text. Top (bottom) left: ESR-STM measurements at $B_{\mathrm{ext}} = 40(25)$ mT. ($T = 400$ mK, $V_{\mathrm{RF}} = 40$ mV, $I_{\mathrm{set}} = 2$ pA).) Top and bottom right: simulations matching the data.

7.7.5. NUCLEUS AS A SOURCE OF DECOHERENCE

Lastly, we perform an experiment with two Ti atoms that is almost identical to the one described in chapter 4. The only difference is that the dimer is now made up of one ^{48}Ti and one ^{47}Ti. We apply a relatively large external field of $B_{\mathrm{ext}} = 480$ mT so the electron spins are fully detuned from the nuclear spin in the ^{47}Ti atom. We place the two spins on different bridge binding sites and compensate for the difference in electron spin g-factors using the local magnetic field emanating from the STM tip.

In fig. 7.9A-D we show data for a reference dimer built out of two ^{48}Ti. Just like in chapter 4 we find the location of the avoided crossing in ESR sweeps and observe coherent oscillations in the pump-probe measurements. Measurements of the dimer containing the nuclear spin are presented in fig. 7.9E-H. As expected, the ESR resonances appear broader since they contain multiple energy transitions due to the hyperfine interaction with the nucleus. However, an avoided crossing is still faintly observable. The pump-probe data taken on this dimer, shown in fig. 7.9H, show similar coherent oscillations to the reference dimer (fig. 7.9D). The frequency of the oscillation on both dimers is nearly identical, but the structure with the nuclear spin shows significantly lower amplitude and has a broader tuning point compared to the reference. We can understand this by plotting the eigenstates of both dimers (fig. 7.9A and E). When the nuclear spin is in a

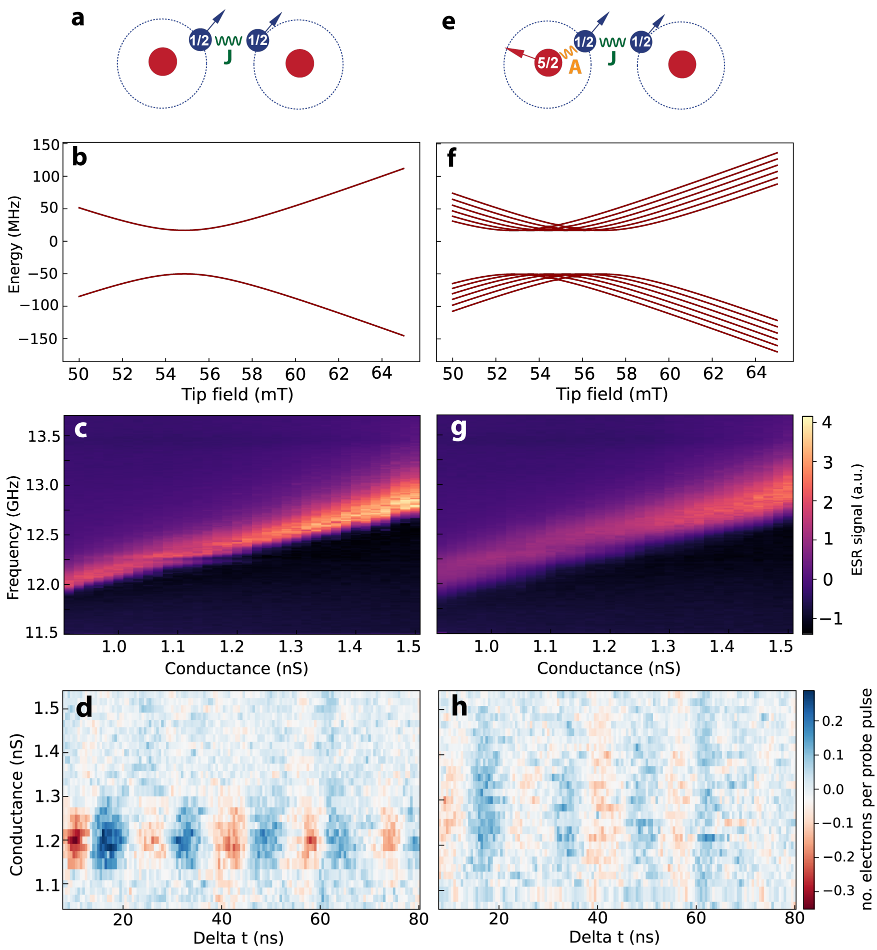

Figure 7.9: Influence of a detuned nuclear spin on coherent dynamics. A. Schematic of the experiment: the electron spins of two ^{49}Ti are coupled and tuned by the field emanating from the STM tip. Identical setup to the experiment discussed in chapter 4. **B.** Energy diagram of the first two excited states forming an avoided crossing. **C.** ESR-STM measurements on the dimer as a function of tip height. (Experimental parameters: $T = 1.5\text{K}, V_{\text{set}} = 60$ mV, $B_{\text{ext}} = 480$ mT) **D.** Pump-probe measurements as a function of tip height. (Experimental parameters: $T = 400$ mK, $B_{\text{ext}} = 480$ mT, pump: 80 mV, 7 ns, probe: -80 mV, 7 ns) **E-H.** Same figures as **A-D** but for a simer consisting of one ^{49}Ti and one ^{48}Ti atom.

fully mixed state, the flip-flop oscillation of the electron spin will occur over a multitude of eigenstates. Since these are all split by the hyperfine interaction, the effective avoided crossing is also broadened by this splitting. Note that the pump-probe data in fig. 7.9 is taken using the same experimental setup used for chapters 4 and 5, in contrast to the rest of the data presented in this chapter which is acquired using the AWG setup (see chapter 3 for details on the different setups).

REFERENCES

[1] **L. M. Veldman**, E. W. Stolte, M. P. Canavan, R. Broekhoven, P. Willke, L. Farinacci, and S. Otte. "Coherent spin dynamics between electron and nucleus within a single atom". In: *arXiv preprint arXiv:2309.03749* (2023).

[2] P. Neumann, J. Beck, M. Steiner, F. Rempp, H. Fedder, P. R. Hemmer, J. Wrachtrup, and F. Jelezko. "Single-shot readout of a single nuclear spin". In: *science* 329.5991 (2010), pp. 542–544.

[3] R. Vincent, S. Klyatskaya, M. Ruben, W. Wernsdorfer, and F. Balestro. "Electronic read-out of a single nuclear spin using a molecular spin transistor". In: *Nature* 488.7411 (2012), pp. 357–360.

[4] J. J. Pla, K. Y. Tan, J. P. Dehollain, W. H. Lim, J. J. Morton, D. N. Jamieson, A. S. Dzurak, and A. Morello. "A single-atom electron spin qubit in silicon". In: *Nature* 489.7417 (2012), pp. 541–545.

[5] S. Baumann, W. Paul, T. Choi, C. P. Lutz, A. Ardavan, and A. J. Heinrich. "Electron paramagnetic resonance of individual atoms on a surface". In: *Science* 350.6259 (2015), pp. 417–420.

[6] P. Willke, Y. Bae, K. Yang, J. L. Lado, A. Ferrón, T. Choi, A. Ardavan, J. Fernández-Rossier, A. J. Heinrich, and C. P. Lutz. "Hyperfine interaction of individual atoms on a surface". In: *Science* 362.6412 (2018), pp. 336–339.

[7] K. Yang, P. Willke, Y. Bae, A. Ferrón, J. L. Lado, A. Ardavan, J. Fernández-Rossier, A. J. Heinrich, and C. P. Lutz. "Electrically controlled nuclear polarization of individual atoms". In: *Nature nanotechnology* 13.12 (2018), pp. 1120–1125.

[8] K. Yang, W. Paul, S.-H. Phark, P. Willke, Y. Bae, T. Choi, T. Esat, A. Ardavan, A. J. Heinrich, and C. P. Lutz. "Coherent spin manipulation of individual atoms on a surface". In: *Science* 366.6464 (2019), pp. 509–512.

[9] **L. M. Veldman**, L. Farinacci, R. Rejali, R. Broekhoven, J. Gobeil, D. Coffey, M. Ternes, and A. F. Otte. "Free coherent evolution of a coupled atomic spin system initialized by electron scattering". In: *Science* 372.6545 (2021), pp. 964–968.

[10] K. Yang, W. Paul, F. D. Natterer, J. L. Lado, Y. Bae, P. Willke, T. Choi, A. Ferrón, J. Fernández-Rossier, A. J. Heinrich, *et al.* "Tuning the exchange bias on a single atom from 1 mT to 10 T". In: *Physical Review Letters* 122.22 (2019), p. 227203.

[11] S. Thiele, F. Balestro, R. Ballou, S. Klyatskaya, M. Ruben, and W. Wernsdorfer. "Electrically driven nuclear spin resonance in single-molecule magnets". In: *Science* 344.6188 (2014), pp. 1135–1138.

[12] G. Fuchs, G. Burkard, P. Klimov, and D. Awschalom. “A quantum memory intrinsic to single nitrogen–vacancy centres in diamond”. In: *Nature Physics* 7.10 (2011), pp. 789–793.

[13] J. Randall, C. Bradley, F. van der Gronden, A. Galicia, M. Abobeih, M. Markham, D. Twitchen, F. Machado, N. Yao, and T. Taminiau. “Many-body–localized discrete time crystal with a programmable spin-based quantum simulator”. In: *Science* 374.6574 (2021), pp. 1474–1478.

[14] J. R. Maze, P. L. Stanwix, J. S. Hodges, S. Hong, J. M. Taylor, P. Cappellaro, L. Jiang, M. G. Dutt, E. Togan, A. Zibrov, *et al.* “Nanoscale magnetic sensing with an individual electronic spin in diamond”. In: *Nature* 455.7213 (2008), pp. 644–647.

[15] S. Zaiser, T. Rendler, I. Jakobi, T. Wolf, S.-Y. Lee, S. Wagner, V. Bergholm, T. Schulte-Herbrüggen, P. Neumann, and J. Wrachtrup. “Enhancing quantum sensing sensitivity by a quantum memory”. In: *Nature communications* 7.1 (2016), p. 12279.

[16] I. Žutić, J. Fabian, and S. D. Sarma. “Spintronics: Fundamentals and applications”. In: *Reviews of modern physics* 76.2 (2004), p. 323.

[17] W. Wernsdorfer and M. Ruben. “Synthetic Hilbert space engineering of molecular qudits: Isotopologue chemistry”. In: *Advanced Materials* 31.26 (2019), p. 1806687.

[18] B. E. Kane. “A silicon-based nuclear spin quantum computer”. In: *nature* 393.6681 (1998), pp. 133–137.

[19] S. Yang, Y. Wang, D. B. Rao, T. Hien Tran, A. S. Momenzadeh, M. Markham, D. Twitchen, P. Wang, W. Yang, R. Stöhr, *et al.* “High-fidelity transfer and storage of photon states in a single nuclear spin”. In: *Nature Photonics* 10.8 (2016), pp. 507–511.

[20] P. Willke, K. Yang, Y. Bae, A. J. Heinrich, and C. P. Lutz. “Magnetic resonance imaging of single atoms on a surface”. In: *Nature Physics* 15.10 (2019), pp. 1005–1010.

[21] A. A. Khajetoorians, J. Wiebe, B. Chilian, and R. Wiesendanger. “Realizing all-spin–based logic operations atom by atom”. In: *Science* 332.6033 (2011), pp. 1062–1064.

[22] L. Wang, Y. Xia, and W. Ho. “Atomic-scale quantum sensing based on the ultrafast coherence of an H2 molecule in an STM cavity”. In: *Science* 376.6591 (2022), pp. 401–405.

[23] K. Yang, Y. Bae, W. Paul, F. D. Natterer, P. Willke, J. L. Lado, A. Ferrón, T. Choi, J. Fernández-Rossier, A. J. Heinrich, *et al.* “Engineering the eigenstates of coupled spin-1/2 atoms on a surface”. In: *Physical Review Letters* 119.22 (2017), p. 227206.

[24] M. Steinbrecher, W. M. Van Weerdenburg, E. F. Walraven, N. P. Van Mullekom, J. W. Gerritsen, F. D. Natterer, D. I. Badrtdinov, A. N. Rudenko, V. V. Mazurenko, M. I. Katsnelson, *et al.* “Quantifying the interplay between fine structure and geometry of an individual molecule on a surface”. In: *Physical Review B* 103.15 (2021), p. 155405.

[25] L. Farinacci†, **L. M. Veldman**†, P. Willke, and S. Otte. “Experimental determination of a single atom ground state orbital through hyperfine anisotropy”. In: *Nano Letters* 22.21 (2022), pp. 8470–8474.

[26] J. Kim, K. Noh, Y. Chen, F. Donati, A. J. Heinrich, C. Wolf, and Y. Bae. “Anisotropic hyperfine interaction of surface-adsorbed single atoms”. In: *Nano Letters* 22.23 (2022), pp. 9766–9772.

[27] S. R. McMillan, N. J. Harmon, and M. E. Flatté. “Image of dynamic local exchange interactions in the dc magnetoresistance of spin-polarized current through a dopant”. In: *Physical review letters* 125.25 (2020), p. 257203.

[28] C. L. Degen, F. Reinhard, and P. Cappellaro. “Quantum sensing”. In: *Reviews of modern physics* 89.3 (2017), p. 035002.

[29] R. Savytskyy, T. Botzem, I. Fernandez de Fuentes, B. Joecker, J. J. Pla, F. E. Hudson, K. M. Itoh, A. M. Jakob, B. C. Johnson, D. N. Jamieson, *et al.* “An electrically driven single-atom “flip-flop” qubit”. In: *Science Advances* 9.6 (2023), eadd9408.

[30] Y. Bae, K. Yang, P. Willke, T. Choi, A. J. Heinrich, and C. P. Lutz. “Enhanced quantum coherence in exchange coupled spins via singlet-triplet transitions”. In: *Science Advances* 4.11 (2018), eaau4159.

[31] M. Shiddiq, D. Komijani, Y. Duan, A. Gaita-Ariño, E. Coronado, and S. Hill. “Enhancing coherence in molecular spin qubits via atomic clock transitions”. In: *Nature* 531.7594 (2016), pp. 348–351.

[32] F. D. Natterer. “Waveform-sequencing for scanning tunneling microscopy based pump-probe spectroscopy and pulsed-ESR”. In: *MethodsX* 6 (2019), pp. 1279–1285.

[33] S. Loth, C. P. Lutz, and A. J. Heinrich. “Spin-polarized spin excitation spectroscopy”. In: *New Journal of Physics* 12.12 (2010), p. 125021.

8

CONCLUSION & OUTLOOK

This thesis describes experiments demonstrating the free, coherent spin dynamics in magnetic nanostructures built atom-by-atom on a surface. We use the powerful combination of continuous-wave ESR and pump-probe spectroscopy to study these kinds of systems inside an STM. Using ESR measurements we are able to resolve the avoided level crossings occurring in these systems due to a competition between spin-spin coupling and different, local Zeeman energies. We aim to measure dynamics at these points, since there the eigenstates form superposition states of the Zeeman basis states. Subsequently, we show that using a short DC bias pulse, we are able to flip the spin of a single atom inside these structures. Thereby, we create a single magnon which then is either allowed to undergo some dynamical oscillation or not depending on the system Hamiltonian. We have a fine tuning parameter of this Hamiltonian in the form of the STM tip's magnetic exchange field which is highly localised and can be controlled by the tip-atom distance. By changing this experimental parameter, we show that we can control the dynamics of the single spin excitation inside the nanostructure.

Using the novel measurement scheme described above, we have shown the flip-flop interaction between the electron spins of two neighbouring Ti atoms in a proof-of-concept measurement (see chapter 4). Next, we applied this technique to atomic chains of different lengths. We found that the single magnon excitation becomes delocalized over the chain in different ways depending on the placement of the STM tip (see chapter 5). We then moved from studying the atom's electron spins to studying its nuclear spin. In chapter 6, we mapped the anisotropy of the hyperfine coupling between nuclear and electron spin in a single ^{49}Ti isotope and used the experimental data to derive the ground state orbital the electron spin resides in. Lastly, we used the measurement scheme of chapters 4 and 5 to measure the free, coherent dynamics between the electron and nuclear spins inside a single ^{47}Ti isotope (see chapter 7). Due to the larger spin number of the nucleus, as well as the interplay between the anisotropic hyperfine interaction and the magnetic tip field, we find a beating pattern of multiple frequencies. Since every chapter has its own conclusions section that focuses on the take-away message of that particular set of experiments, here we would like to discuss the broader conclusions that can be drawn from the thesis as a whole.

First, the ESR experiments performed in this thesis show that we can study single atom systems with such high energy resolution that we can measure spin interactions and anisotropies that are completely invisible without this technique. This allows us to deduce significantly more information from our system, like the isotope of the adatom and the groundstate orbital of the probed electron spin. In this thesis we focused on Ti atoms on an Mgo/Ag(100) surface but this technique has the potential to uncover different phenomena when applied to different systems like molecular magnets, 4f-elements and nanographene flakes. ESR-STM could shed light on the spin distribution in these systems, the role of spin-orbit interaction and molecular groundstate orbitals.

Second, the pump-probe experiments in this thesis show that a spin system in a thermal groundstate can be excited to a coherent quantum state via scattering with an incoherent spin bath. We achieve this by allowing the scattering events to occur only on a highly localised part of the spin system. The STM tip is the ideal tool for this type of state manipulation as it effectively is a spin polarized electron bath that can be positioned above a nanostructure with sub-atomic precision. Measurements on atomic chains of different lengths showed that this method can be used to inject a single spin flip into a spin system and measure it's propagation in time resolved experiments. This opens the door to studying magnon propagation in spin ladders, two dimensional spin lattices and frustrated systems built atom-by-atom.

Third, our experiments on nuclear spins show that they hold great promise for further experiments involving coherent dynamics. Our pump-probe experiments show that it is possible to control and read out the spin state of the nucleus via the electron spin. On top of that, the observation of very sharp NMR-type transitions hint at future possible coherent control of the nuclear spin via pulsed RF experiments. Furthermore, experiments combining both DC and RF pulses could give even greater control over the nuclear spin and allow for utilization of its longer coherence time compared to the electron spin.

In conclusion, the study of coherent spin physics on the atomic scale using STM is currently still in its infancy. In general, compared to the spatial axes, time has been a relatively under-explored dimension in STM research. Together with techniques like THz-STM and time resolved luminescence, the study of coherent spin dynamics is one of the up-and-coming research directions that is changing this. The platform offers a unique combination of atomic scale control and nanosecond time resolution that makes it ideal for studying nano-scale magnetic dynamics. The challenge that remains at the moment is to find different sample systems that allow for longer coherence times as this is currently an important limiting factor for studying long range magnon evolution as well as qubit operations and magnetic sensing applications.

ACKNOWLEDGEMENTS

Questions of science, science and progress
Do not speak as loud as my heart

Coldplay

When I started my PhD on April 1st 2019 (yes, my PhD was destined to be a joke from the very first day) I had already been a student at the TU Delft for over five years. At the end of those five years, I thought I had learned enough physics to get me through the rest of my life and I figured I had seen everything there was to see in the small town of Delft. I was ready to spread my wings and leave the university to start a life far away from lecture halls and homework exercises. My master thesis was supposed to be the last big effort of my studies, but oh, how I miscalculated. When I started working in an actual research group, I immediately became enamoured with the academic life that was so different from the one I had experienced in the five years prior. No sleepy lecture halls surrounded by half-interested fellow students, no numbing rhythm of exam period after exam period and no boring fabricated homework exercises. Instead, all of a sudden I found myself surrounded by an incredibly divers, open and inspiring group of people that were as enthusiastic about discovering physics that you couldn't yet find in textbooks as they were meeting people, moving abroad and starting something new. It is those people that made my time in Delft one that changed my life and to those people I will always be incredibly grateful.

I vividly remember the first time I met **Sander**, when I interviewed for a master thesis in his group. I was as amazed by the fact that he was able to move thousands of atoms one by one, as I was by the fact that all his valuable machines were covered in aluminum foil for some reason. On top of that, I was struck by his ability to break down difficult quantum mechanical concepts in understandable chunks and his clear passion for teaching. Now, five years later, I am very grateful to you for the journey we have been on and the opportunities you have given me. I have learned not just about moving atoms and why the machines are covered in aluminum foil, but also about the intricacies of time and people management and the dos and don'ts of academia. All of this has shaped me as a scientist and I very much look forward to working in the same research field in the near future.

To **Toeno**, the copromotor of this thesis, thank you very much for the progress meetings, career advice and paintball games throughout the years. Your dedication to the scientific as well as the interpersonal aspects of academia is truly inspiring. **Philip Willke**, I remember being incredibly nervous when I sent you an e-mail with questions about ESR-STM as a PhD student that had only just started. Now, I am very proud to have worked with you on the two chapters involving nuclear spins in this thesis. Thank you so much for your expertise, patience and your everlasting good spirits. **Markus Ternes**, it was a pleasure and a privilege to have worked with you on the free evolution chapter of this thesis. Chatting and discussing physics with you was always a wonderful experience and your knowledge on so many topics in physics is astonishing. To **Alex Khajetoorians**, **Harald Brune** and **Simon Gröblacher**, thank you so much for taking the time and effort to carefully read my thesis. It is a great privilege to have you in my thesis committee and I eagerly look forward to your insights.

I was extremely lucky to work with a group of impressively capable physicists during my PhD. Without their input, hard work and patience, this thesis wouldn't even be a shadow of what it is now and I owe them a great deal of gratitude for this. But I realise I have to count myself doubly lucky since these people turned out to not only be incredibly smart, but also some of the most kind, warm and fun people I have met. They made long days in the lab feel short and difficult problems feel like exciting puzzles.

To the wise postdoc not just in the lab but also in life itself, **David**, the things I learned from you as a master student and as a young PhD student rekindled my enjoyment of physics. On top of that, you are one of the most kindhearted, dedicated and caring people I have ever met. Over the years, you were a mentor even when you had left academia and you have become a great friend. As you once said yourself: the things you do come from a place of love, be it completely covering my first feeble attempt at writing a master thesis in red ink, guiding me through tricky workplace situations or tolerating my unhinged late night ideas for new experiments. Now that I am a postdoc myself, I still regularly quote your famous phrases: thanks to you there won't be a single student in Stuttgart who doesn't have their eyes on the prize. It was also an absolute joy to see you and **Ione** become amazing parents to **Sara** in the last year. It is a great excuse to come visit you more often before she has already grown up!

To **Hester**, my soft-spoken fellow arthouse film fanatic and, unbeknownst to most, the best artist in residence QN has had. It has been such a great pleasure to become a friend of yours in the last couple of years. From collecting songs for our lab playlist (that still has to see the light of day) to nightlife adventures in Amsterdam to nerding out over design furniture. You approach people with the same thoughtfulness, finesse and care as you do putting together AFM sensors and I very much admire that. Thank you so much for your advice (on life, burnout, workplace shenanigans and, of course, on film recommendations) and for brightening my days in Delft with your party vibes and sense of humor. Your friendship has made the more difficult parts of the last years a lot easier. Please come visit Stuttgart soon! They have a lot of squirrels running around the city that are almost as cute as cats.

My time in the lab would not have been the same without my two bullies: **Laëti** and **Rasa**. In spite of all the horrible crimes you have committed against me over the years, I am eternally grateful that I got to work and hang out with you guys. Although I have to say I might be suffering from a strange form of Stockholm syndrome at this point. You made work not feel like actual work but more like kindergarten recess. Both in the sense that beverages were regularly coming out of our noses because we were laughing so much and in the sense that airborne footwear was occasionally directed towards my face.

Rasa, I'm so happy I found such a great friend in you. When David left, you took it upon yourself to guide this very green PhD student through the He3 lab and I could not have wished for a better companion to take my first steps into the scary world of running ones own experiments. Still every time I touch a button to change the magnetic field I hear you scream 'QUUEEENCH!' in the back of my head. I also still flinch every time somebody holds a water bottle too close to me. But on a serious note, thank you for bringing so much joy into my life in Delft. Spending this time together made me look up to you a lot because you seem to defy all preconceived notions of what a scientist should be: You're a very talented and smart physicist and somehow you are also always the center of any party. On top of that, you quote John Milton and Jane Austin as effortlessly as you (try to) sing along to Maluma and Celine Dion (or should we count her as high culture?). And you can spend ten minutes laughing about a molecule that only very vaguely resembles a phallic shape and then seconds later you turn into a beacon of wisdom giving advice on my personal life. I don't know how you do it.

Laëti, with you joining the lab in January 2020, many things, both inside the lab and outside, got turned upside down. All of a sudden, I got to work with a postdoc that turbocharged every project she worked on and I had found a new partner in crime to complete our triumvirate with Rasa. Pre-pandemic we both screamed our lungs out together at a Carly Rae Jepsen concert while after COVID struck we ordered more and more elaborate dinners to the lab on long workdays. During that time, I learned so much from you, from long discussions about spin-spin scattering to how to properly cut Roquefort without invoking the anger of the French nation. Writing down how much you contributed to this thesis and how much you have helped me get through difficult periods would probably double the page count, so I won't be able to do justice to all the work you put in and to all your care, dedication and affection of the last years. Just know that I am incredibly grateful and that I consider myself very lucky that I got to share this time in Delft with you.

One of the results from my PhD I take most pride in is that the two master students I supervised not only finished very successful projects but also both decided to continue in academia. Early on in my PhD, I had the privilege to supervise a very excellent student: **Rik**. The only problem was that he was so excellent that I had to work double shifts to keep up with the theoretical insights coming out his project next to the grind of labwork. In all seriousness though, I learned a lot from you and your incredibly friendly, upbeat character and cheerful laugh made it a joy to work with you. I was very happy when you decided to stay in the group for a PhD and I continue to be very impressed by the things that come out of your brain.

At the end of my PhD, I was blessed with another outstanding student: **Mark**. Your calm and thoughtful approach to science, as well as your obvious talent for it, made working with you an absolute breeze. Both inside and outside of the lab, I got to know you as a very kind, warm, hardworking and clever person. I'm certain you will do great things at ETH Zürich and I look forward to hearing about them at future conferences. I will definitely come visit in Switzerland as soon as time allows!

My time in the Ottelab would not have been the same without the rest my wonderful colleagues. My comrade in the great struggle, **Alex**, your optimism brightened many coffee breaks and I very much enjoyed the discussions we had, ranging from politics to Lady Gaga. I am very happy that you got a permanent position in Delft and I am certain that you will be a force for good in the world of professors. My destined successor in the lab, **Evert**, I've had a great time working with you and discussing science. I very much admire your passion for physics and I'm certain the Ti atoms are in good hands with you. May your roaring laugh never seize! **Jérémie**, the work in this thesis benefited a lot from the LabView infrastructure you set up, I'm very grateful for that. On top of that, it was a pleasure sharing an office with you and I learned a lot from our discussions on physics at the start of my PhD. **Robbie**, VI aficionado, board game designer and YouTube influencer. The many facets of your personality always made for intriguing stories during lunch breaks. It was a pleasure sharing time in the group with you and I wish you all the best on your great American adventure! **Vivien**, for the relatively short time that you were part of the group, I very much enjoyed your very friendly, relaxed and caring approach to science. **Koen**, it was inspiring to discuss with you during the weekly group meetings. I wish you all the best with your new career at ASML. **Maura**, it was a lot of fun to have you in the group. Thank you so much for the positive and happy atmosphere you bring with you.

My time in the department of Quantum Nanoscience would not have been half as pleasant if it wasn't for the wonderful people working there. They reminded me that even amongst physicists there is fun to be had outside of the lab. To the most talented breakdancer (with and without roller-skates) that I have every had the pleasure of sharing a dance floor with: **Matty**, the self proclaimed viking. I'm very happy that I got to know you as the kind, musical and clever intellectual that you are (come to think of it, those traits are probably also the reason the nickname 'the viking' never caught on). It makes it all even more enjoyable when I got a glimpse of the tiny bit of crazy underneath when you start climbing an excavator parked in the street or drop to the floor in a crowded club. To my well dressed companion **Lacopo**, ambassador of the *joie de vivre* among physicists. Thank you for all those years of dragging people out of the TN building towards bars and for being one of those important bridges connecting people of different research groups. **Luigi**, you were one of the people that made QN such an open and welcoming environment. Thank you so much for your dedication to getting people to join TPKV, organising parties and of course your famous memes. Best of luck in Manchester! **Sona**, you absolutely were a social bridge between people from groups as well, even between departments. Thank you very much for making QN such a nice place. To the undisputed Mario Kart champion of QN, **Patrick**, thank you for being a friend, the fun times in Chicago and the many nights of beer, pizza and videogames. It was a very welcome and enjoyable time both during and after the pandemic. To the Italian farmer turned physicist, **Ulderico**, thank you for the many enjoyable coffee breaks. Your sense of humor was a highlight in certain days of greyness. From time to time I catch myself making your 'sad last pear hanging from a tree' gesture in conversation. **Thierry**, I always appreciated your truly Dutch humor and honesty. Thank you for the many nice lunch breaks and for always being in for a Friday drink. My fellow lover of dry bread, **JorJor**, it was a pleasure to share many lunch breaks with you. Not only because it made my own Dutch sandwiches look less bad but also because of the great conversations and of course the mandatory updates on the relationship therapy of your rabbits. **Samer**, it was a blast every time I hung out with you after work. Your path in academia is inspirational and it's a shame you didn't decide to continue it in Stuttgart! Oh, and thank you for that one time you made an entire bus full of physicists wait for me in Veldhoven because I overslept, I still owe you for that one. **Joris**, it always was great fun hanging out during Friday drinks. Your upbeat attitude is very contagious. Fellow member of the three tired boys, **Michael**, unfortunately our band never came off the ground but hey, who needs fame, money and sex appeal when you can be a physicist, am I right? Thanks for the good times though. Most of all I will miss you coming into my office to randomly charge your phone there. Those small moments were truly special. **Brecht**, you were always such a very pleasant and cheerful person to chat with, be it during Fridays at TPKV, the occasional trip to the beach in Katwijk or during a fierce paintball battle. **Allard**, every time we discussed physics I was amazed by how much you know. Not only are you a great scientist but you also take the well-being of the PhD students at QN to heart. Thank you for making such a positive impact on the department. **Gary**, thank you so much for the amazing coffee machine in the QN department. It has changed my taste buds forever.

There are still many people that I didn't get to interact with nearly as much as I would have wanted during the five years that I was at the QN department. They still were a very big part in making it a social, welcoming community: **Nina, Nicco, Parsa, Irina, Sabrya, Sonia, Edouard, Marc, Jinkun, Maarten** and many more.

However, the department would've probably fallen apart rather fast if it wasn't for the support staff: **Etty, Heleen, Karin** and **Maria**. Thank you so much for the years of hard work and great care. **Marinka**, you have helped me during very difficult times in my PhD. I am immensely grateful for your support and your great advice.

During my PhD I was approached by **Gesa** who had the amazing initiative to organise an online workshop for young researchers by young researchers to replace the NanoMRI conference that was cancelled due to the pandemic. Together with **Martin, Leora and Laëti** we set up a very exciting week long program in collaboration with the Lorentz center in Leiden. I am very grateful for the opportunity to take part in the organisation of the event and to get to do that with such a wonderful group of people.

Before this thesis was completely finished, I had already moved to Germany to start a postdoc in the group of **Sebastian Loth** at the University of Stuttgart. I'm very grateful to him and the rest of the group: **Susanne, other Lukas, Nicolaj, Kurt, Felix, Henrik, Johannes, Vivek** and **Svenja** for their very warm welcome as well as their patience while I was still balancing the work of starting in a new country with finishing the last things for my PhD in Delft.

I also owe a great deal of gratitude to the people in my life outside of science that supported me through the years. First of all, **Marlou**, without you I might have never had the necessary nerve, confidence and drive to try and pursue a PhD. You have played a huge role in who I am as a person today. You were my best friend, confidante and source of inspiration for many years and I will always be immensely grateful for that.

I have also been very lucky to be surrounded by a group of friends that I have known for many years and without whom I don't know what I would do with myself. **Dan, Melle, Dua, Judith, Maud, Milo, Kees, Mees** and **Rick**, without you guys I would have had several mental breakdowns already. Thank you so much for keeping me sane and making life a joy in general.

I couldn't have made my first steps into the scary world of physics without my dear friends from the bachelors: **Artiom, Arend** and **Jasper**. Honestly, at some points it felt like you guys were just carrying me through it on moments of mathematical despair. Thank you for all the great times.

I also don't think I could have finished the PhD without my weekly noise generation sessions. **Ramon, Ludwin, Richard** and **Derk**, making music with you was a privilege, an amazing learning experience and above all a tremendous amount of fun. I am truly sad I had to leave you and I miss playing with you a lot. But I am very grateful to have been part of Tiger Pilots and HOOFS and I eagerly look forward to your continuing rise to stardom. Whenever I can make it, you'll find me in the audience all the way at the front.

Finally, I want to thank my family: **Emmie, Reinier** and **Jozias**. I have always felt incredibly supported growing up and I felt free to choose to become whatever I wanted to. I don't know where I would be without your guidance, encouragement and love but I know it brought me here and for that I am deeply grateful.

CURRICULUM VITÆ

Lukas Maarten VELDMAN

21-04-1995	Born in Amsterdam, The Netherlands.

EDUCATION

2007–2013	Grammar School Het 4^{e} Gymnasium, Amsterdam
2013–2016	Bachelor's degree in Applied Physics Technische Universiteit Delft
2015	Minor programme in Literary Studies Vrije Universiteit Amsterdam
2016–2019	Master's degree in Applied Physics Technische Universiteit Delft
2019	Research & Development Internship SPECS group, Berlin
2019–2023	PhD. in Physics Technische Universiteit Delft Department of Quantum Nanoscience *Thesis:* Coherent dynamics of atomic spins on a surface *Promotor:* Prof. dr. A.F. Otte

LIST OF PUBLICATIONS

1. **L. M. Veldman**, L. Farinacci, R. Rejali, R. Broekhoven, J. Gobeil, D. Coffey, M. Ternes, and A. F. Otte. "Free coherent evolution of a coupled atomic spin system initialized by electron scattering". In: *Science* 372.6545 (2021), pp. 964–968
2. L. Farinacci[†], **L. M. Veldman[†]**, P. Willke, and S. Otte. "Experimental determination of a single atom ground state orbital through hyperfine anisotropy". In: *Nano Letters* 22.21 (2022), pp. 8470–8474
3. **L. M. Veldman**, E. W. Stolte, M. P. Canavan, R. Broekhoven, P. Willke, L. Farinacci, and S. Otte. "Coherent spin dynamics between electron and nucleus within a single atom". In: *arXiv preprint arXiv:2309.03749* (2023)
4. **L. M. Veldman**, L. Farinacci, and S. Otte. "Coherent single magnon dynamics at the atomic scale". *In preparation.*

[†] These authors contributed equally.